Design and Control of an Active Ankle-Foot Orthosis

by

Benjamin DeBoer

A thesis submitted to the School of Graduate and Postdoctoral Studies in partial fulfillment of the requirements for the degree of

Master of Applied Science in Mechanical Engineering

Faculty of Engineering and Applied Science
University of Ontario Institute of Technology
Oshawa, Ontario, Canada
April 2022

Thesis Examination Information

Submitted by:

Benjamin DeBoer

Master of Applied Science in Mechanical Engineering

Thesis Title:

Design and Control of an Active Ankle-Foot Orthosis

An oral defense of this thesis took place on April 13th, 2022 in front of the following examining committee:

Examining Committee

Chair of Examining Committee	Dr. Amirkianoosh Kiani
Research Supervisor	Dr. Sayyed Ali Hosseini
Research Co-Supervisor	Dr. Carlos Rossa
Examining Committee Member	Dr. Scott Nokleby
Thesis Examiner	Dr. Matthew Harker

The above committee determined that the thesis is acceptable in form and content and that a satisfactory knowledge of the field covered by the thesis was demonstrated by the candidate during an oral examination. A signed copy of the Certificate of Approval is available from the School of Graduate and Postdoctoral Studies.

Abstract

ACTIVE ankle-foot orthoses (AAFOs) assist a user unable to dorsiflex the ankle joint. The optimal AAFO is lightweight and aids the user in achieving a nominal gait.

This thesis presents the design and control of a novel discrete nonlinear series elastic actuator for AAFOs. The actuator uses regenerative braking to reduce the peak mechanical input power to the AAFO by 77.2%.

To control the designed actuator and AAFO, two methods are proposed. First, an adaptive extended state observer is developed to reject disturbance and estimate the error in the dynamics model. Second, a nonlinear model predictive controller is presented to track the ankle trajectory while reducing assistance to the user.

The adaptive extended state observer can identify the AAFO and ankle joint parameters. The nonlinear model predictive controller with the adaptive extended state observer reduced the trajectory tracking error by up to 58.3%.

Keywords: foot drop, active ankle-foot orthoses, series elastic actuator, adaptive disturbance rejection, model predictive control

Author's Declaration

I declare that the thesis presented here is my original work that I have authored. It is a true copy of the thesis.

I grant the University of Ontario Institute of Technology the right to lend this thesis, for the purpose of scholarly research, to other individuals or institutions. Additionally, I grant the University of Ontario Institute of Technology the right to reproduce by means of photocopying or other, this thesis, partially or fully per the request of other institutions or individuals forthe purpose of scholarly research. I acknowledge this thesis will be made publicly available through electronic means.

Benjamin DeBoer

Statement of Contribution

Parts of the work described in this thesis have been published in peer-reviewed journals, and conferences as follows:

Chapter 2

B. DeBoer, A. Hosseini, and C. Rossa, 'A Discrete Non-Linear Series Elastic Actuator for Active Ankle-Foot Orthoses,' IEEE Robotics and Automation Letters, 2022. https://doi.org/10.1109/LRA.2022.3167065

Chapter 3

B. DeBoer, A. Hosseini, and C. Rossa, 'An Extended Parameter Estimation Disturbance Observer for an Active Ankle Foot Orthosis,' in IEEE International Conference on Systems, Man, and Cybernetics (SMC), 2021, pp. 1105-1110. https://doi.org/10.1109/SMC52423.2021.9659241

Statement of contributions

I developed the concept of discrete nonlinear stiffness for a SEA, the implementation of an extended state observer for parameter estimation, and the formulation of a real-time model predictive controller for active ankle-foot orthoses. The design, construction, and programming of the presented methods were also completed. Dr. Hosseini and Dr. Rossa assisted in analyzing the proposed contributions, developing the prototype and experimental setup, and assisted in revising manuscripts.

Acknowledgments

I WANT to express my immense appreciation to my research supervisors Dr. Hosseini and Dr. Rossa for their endless support over the last two years. You have inspired me to continue in research and strive to reach my fullest potential.

Sincere love and appreciation is expressed to my fiancé and family for their endless support throughout this time.

I would also like to acknowledge Peter Kahr from the Faculty of Engineering and Science at Ontario Tech University for providing the material and manufacturing process to construct the prototype. Additionally, I would like to thank Dr. La Delfa and the Faculty of Health Sciences at Ontario Tech University for providing the clinical facilities to test the proposed concepts and developed prototype.

Table of Contents

List of Figures

List of Tables

List of Abbreviations and Symbols

Abbreviations	
AAFO	Active Ankle-Foot Orthosis
ADRC	Active Disturbance Rejection Control
AFO	Ankle Foot Orthosis
CAD	Computer-Aided Design
DAQ	Data-Acquisition-Card
DC	Direct-Current
DOF	Degree-of-Freedom
EMG	Electromyography
ESO	Extended State Observer
FSR	Force Sensitive Resistor
GRF	Ground Reaction Force
MPC	Model Predictive Control
MR	Magnetorheological
NSGA-II	Non-dominated Sorting Genetic Algorithm II
PAM	Pneumatic Artificial Muscle
PD	Proportional-Derivative
PEA	Parallel Elastic Actuator
PID	Proportional-Integral-Derivative
PME_1	Plant Modelling Error 1
PME_2	Plant Modelling Error 2
RMS	Root Mean Squared
SEA	Series Elastic Actuator
SMC	Sliding Mode Control
VSA	Variable Stiffness Actuator

Symbols (all chapters)	
$\dot{\square}$	Indicates the first time directive
$\ddot{\square}$	Indicates the second time directive
$\square^T$	Indicates the vector or matrix is transformed

Symbols in **Chapter 1**	
$\dot{\delta}_K$	Rate of change of a SEA stiffness element [m/s]
F_K	Axial force within a SEA stiffness element [N]
K	SEA stiffness [N/m]
P_m	Motor power [W]
θ_a	Ankle joint angle [Rad]

Symbols in **Chapter 2**	
A_1, A_2, t_1, t_2	PAM force vs. displacement curve fitting values
$F_{0_{PAM}}$	PAM force vs. displacement curve offset value
P_x, P_y	Location of the slider or crank mounting point in the X and Y direction, respectively [m, m]
S	The slider of a slider-crank mechanism
δ_S	Change in the slider position [m]
F_S	Axial force of the slider [N]
Δb	Axial displacement of link b [m]
F_b	Axial force in link b [N]
P_{SC}	Power of the slider in a slider-crank actuator [W]
P_{CR}	Power of the crank in a crank-rocker actuator [W]
α	Gain scalar for convergence of θ_b
β	Penalty scalar for optimization
a	Length of the lever arm a mounted to the ankle joint [m]
b	Length of the connecting link b in a four bar-mechanism [m]
b_0	Initial length of link b [m]

c	Length of the crank link a in a crank-rocker mechanism [m]
d	Length of the virtual link d between the origin and point (P_x, P_y) [m]
e	Length of the virtual link e between the end of link c and point (P_x, P_y) [m]
t	Time [s]
θ_a	Angular position of the ankle joint [Rad]
$\theta_{a_{invalid}}$	Angular position of θ_a that is not a part of the desired trajectory [Rad]
θ_{adj}	Angular offset of link a from θ_a [Rad]
θ_b	Angular position of link b with respect to the Y axis. [Rad]
θ_c	Angular position of link c with respect to the X axis. [Rad]
θ_{ad}	Angle between links a and d [Rad]
θ_{ce}	Angle between links c and e [Rad]
θ_e	Angle between link e and the Y axis [Rad]
τ_a	Torque at the ankle joint [Nm]
τ_c	Torque at link c point of rotation [Nm]
τ_m	Torque applied by a DC motor [Nm]
F_{PAM}	Axial force within a pre-inflated PAM [N]
δ_{PAM}	The axial displacement of a pre-inflated PAM [m]
P_{PAM}	Internal pressure of a PAM [kPa]
P_{max}	Maximum motor power [W]
k_n	Linear stiffness of spring n [N/m]
n	Number of employed linear springs
$F_{Limit}(n)$	Limit where discrete spring n engages [N]
k_τ	Torque constant of a DC motor [Nm/A]
k_ω	Speed constant of a DC motor [Rad/Vs]
i_m	DC motor armature current [A]
δ_{Off_n}	Displacement where spring n engages [m]
L	Total length of a four-bar mechanism [m]

P_s	Optimization penalty scaler
V_m	DC motor input voltage [V]
n_{gb}	Gearbox efficiency [%]
g_{gb}	Gearbox gear ratio
P_{Cx}, P_{Cy}	The end point of link c in X and Y coordinated [m, m]

Symbols in **Chapter 3**

$\hat{\square}$	Estimate of $\square$
$\tilde{\square}$	Error between the real and estimated value of $\square$
$\square_0$	Initial value of variable $\square$
J_P	AAFO rotational inertia [kg $\cdot$m^2]
B_P	AAFO viscous damping coefficient [Nm $\cdot$ s / Rad]
K_P	AAFO stiffness coefficient [Nm/Rad]
$A(\cdot)$	AAFO state matrix
$B(\cdot)$	AAFO input matrix
$C(\cdot)$	AAFO output matrix
$\vec{\theta}$	AAFO state vector
θ_a	AAFO and ankle joint actual position [Rad]
θ_d	AAFO and ankle joint desired position [Rad]
k	State feedback gain
L	Observer gain
Obs	Observability matrix
u	Controller torque signal [Nm]
u_a	Actuator torque signal [Nm]
u_d	Disturbance torque signal [Nm]
$u_{d_{Nom}}$	Nominal gait disturbance [Nm]
$\vec{\theta}$	AAFO plant state vector [Rad]
$\epsilon_1, \epsilon_2, \epsilon_3$	Scalar gains for the ESO
ϕ_1, ϕ_2, ϕ_3	Saturation gains for the ESO
$\delta_1, \delta_2, \delta_3$	Sampling rate for the ESO

$\tau_{d-model}$	Disturbance due to error in the plant model [Nm]
γ_h	High gain for the adaptive laws
γ_l	Low gain for the adaptive laws
κ	Nominal disturbance torque scaling factor
ζ	Penalization scaler for gains γ_h and γ_l
a_κ, a_J, a_B	Scalar gains for the κ, J_P, B_P adaptive laws

Symbols in **Chapter 4**

$\vec{\theta_a}$	AAFO actual angular position trajectory ($N \times 1$) [Rad]
$\vec{\theta_d}$	AAFO desired angular position trajectory ($N \times 1$) [Rad]
θ_t	AAFO position at time t [Rad]
Δ_t	Discretization time of the control and prediction horizon [s]
$\vec{u_t}$	Control value at time t [Nm]
$\vec{u}$	MPC control vector ($M \times 1$) [Nm]
$\vec{u}_j$	MPC control vector at iteration j [Nm]
Δu_{j+1}	MPC control update vector at iteration $j+1$ [Nm/iteration]
j	Current iteration of the MPC optimization
x	Total number of optimization iterations
z	Number of Newton-Raphson optimization iterations
$\vec{\tau_m}$	Motor torque vector ($M \times 1$) [Nm]
$\vec{\tau_{m_{max}}}$	Peak allowable motor torque [Nm]
G_j	Jacobian at iteration j
λ	Small scalar to ensure matrix inversion
I	$M \times M$ identity matrix
υ	Newton step scalar
Q	Linear decreasing positive definite weighting matrix ($N \times N$)
R, S	Linear increasing positive definite weighting matrices ($M \times M$)
N	Prediction horizon length
M	Control horizon length

C	Cost function
ϕ	Saturation gain

Chapter 1

Introduction

FOOT drop is a result of dorsiflexion deficiency in which the tibialis anterior is unable to provide 60% of the nominal muscle strength [1–4]. Lower motor neuron disease and spinal upper motor neuron pathology can both result in foot drop, both of which are present after a stroke [4]. It is estimated that $62,000$ Canadians suffer a stroke each year, and $405,000$ Canadians are currently suffering from the effects of a stroke [5], out of which $14\% - 20\%$ are affected by some degree of foot drop [3, 4].

Stroke rehabilitation is divided into three stages: acute stage, early-recovery stage, and mid-to-late stage [6]. In the acute stage, the patient has recently suffered a stroke, and rehabilitation is based on manually moving the patient's paretic limb to regain their range of motion [6, 7]. The early-recovery phase implements therapist-assisted static-training exercises to regain muscle control [6, 7]. Dynamic exercises follow in the mid-to-late stage, where the patient is asked to walk, ascend and descend stairs, resulting in further locomotion and muscle development [6,7]. The final rehabilitation stage identifies the presence of long-term paresis of the tibialis anterior, characterized by the foot slapping the ground upon heel contact and toes coming into contact with the ground during the swing phase, creating a tripping hazard [1, 2]. In response, the patient adapts their hip and knee flexion to increase toe clearance, known as steppage gait [2, 8]. The biomechanics of locomotion must be understood to compensate for gait deficiencies due to foot drop.

1.1 Ankle Biomechanics

The functionality of the ankle joint and its plantarflexion torque and power is a critical part of everyday locomotion as it is the joint with the highest torque in the lower body [9]. The role of the ankle, as a joint with three degrees-of-freedom (DOF), in locomotion is to facilitate plantarflexion and dorsiflexion about the talocrural axis, known as the lowering and raising of the toes, respectively. The two additional rotational axes are responsible for inversion/eversion and internal/external rotation about the subtalar and tibial axes [10]. Fig. 1.1 depicts the respective ankle axes of rotation

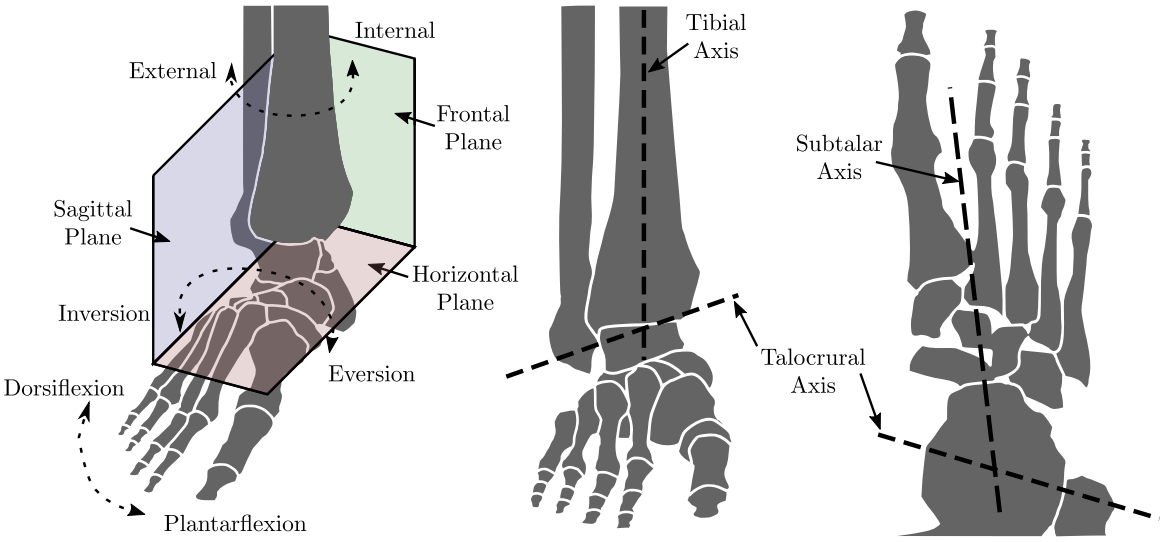

Figure 1.1: Rotational axes and planes of the ankle joint. Plantarflexion/dorsiflexion occurs along the talocrural axis, inversion/eversion about the subtalar axis, and internal/external rotation is about the tibial axis. The figure is redrawn from [10] and [11].

and normal planes of the body. The range of motion for each axis are talocrural $-50° - 20°$, subtalar $-35° - 25°$, and tibial $-25° - 20°$ [10]. In locomotion, the cyclic rotation of the ankle occurs about the talocrural axis. The respective trajectory of the ankle joint angle, applied torque, and power for one step is depicted in Fig. 1.2. The gait cycle is measured from heal-contact to subsequent heal-contact with the ground. In a natural gait, the tibialis anterior provides the dorsiflexion assistance and the soleus and gastrocnemius muscles, also known as the calf muscle, in combination with the Achilles tendon, facilitate plantarflexion. A weakened tibialis anterior is slow or latent to dorsiflex the foot, creating the foot drop deficiency, shown as the dashed line in Fig. 1.2. In the presence of foot drop, the ankle joint is significantly plantarflexed upon heal contact, is slow to plantarflex during the pre-swing phase, and cannot dorsiflex thereafter. To reduce the hazard foot drop presents, patients with persistent foot drop are prescribed an ankle-foot orthosis (AFO) [12].

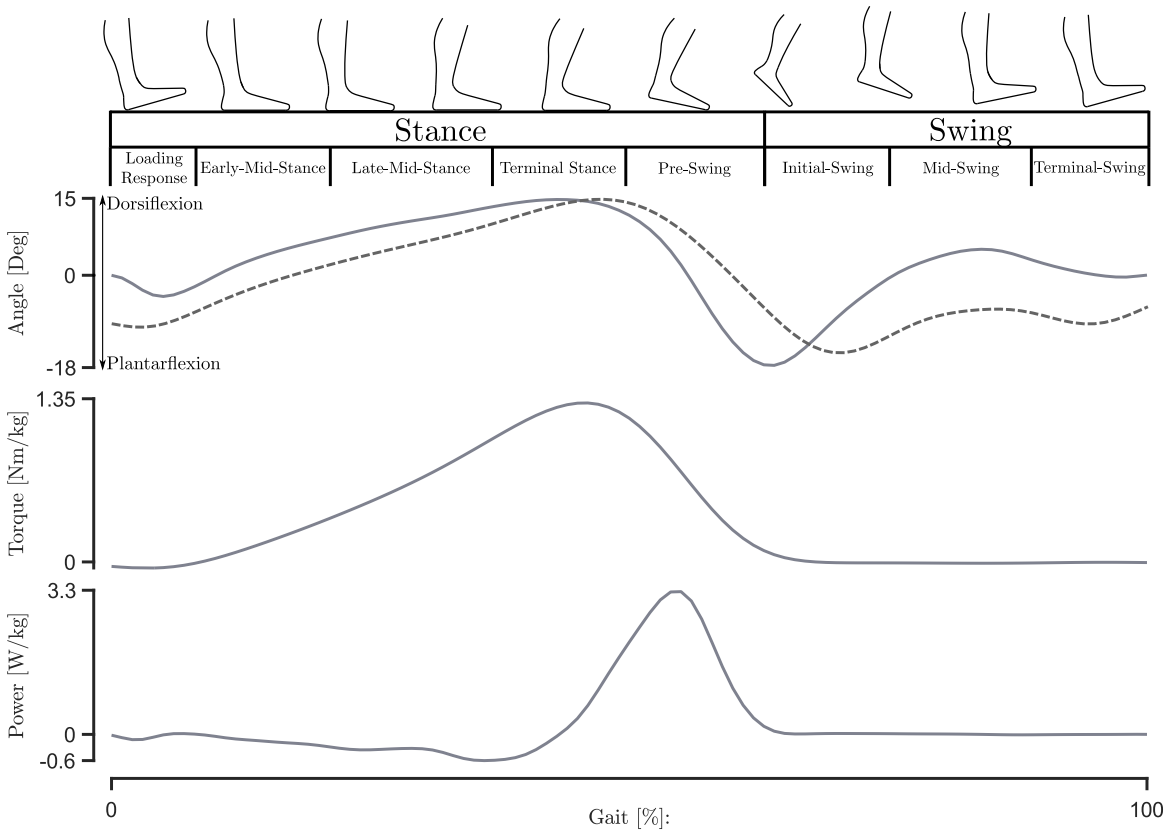

Figure 1.2: Nominal gait angular, torque, and power trajectory, in which the torque and power of the ankle joint are dependent on the mass of the user. The dashed line represents the ankle trajectory in the presence of foot drop. Data from: [9, 13, 14].

1.2 Passive Ankle-Foot Orthoses

A passive AFO limits the user's plantarflexion range of the foot using a mechanical device. The AFO is designed to reduce toe contact during the swing phase while facilitating the dorsiflexion motion of the ankle joint. There are many market available AFO designs, however, the prominent passive AFO designs are either rigid, articulated, or soft (see Fig. 1.3). The first two may be prescribed by a physician.

Rigid AFOs are designed with only one structural component cradling the bottom of the foot and lower calf muscle (see Fig. 1.3b). The rigid structure limits the plantarflexion range of the ankle joint throughout the swing phase. Additionally, the elastic properties and thickness of the material allow adequate dorsiflexion of the brace, inherently storing energy due to the change in ankle position throughout

a) b) c) d)

Figure 1.3: Various types of market available AFOs. a) Soft AFO Device. (Reproduced from [15]). b) Rigid AFO Device. (Reproduced from [16]). c) Articulated AFO Device. (Reproduced from [16]). d) Common methods of rotation for Articulated AFOs. (Reproduced from [17]).

the stance phase (see Fig. 1.2). The energy is then released during push-off to assist in locomotion [10, 18]. Push-off occurs during the pre-swing phase, where a high ankle torque and power is present to propel the user forward (see Fig. 1.2). Articulated AFOs encompass one or more rotational axes, commonly facilitated by a Tamarack Flexure Joint™ or a Scotty joint™, connecting the foot-bed and shank of the AFO [19]. The foot-bed supports the bottom of the user's foot, where the shank surrounds the calf muscle to secure the AFO to the user, depicted in Fig. 1.3c. A Tamarack Flexure Joint™ is comprised of polyurethane with the rotation of the joint based on the compliance of the material, whereas the Scotty Joint™ is a low-profile rotational joint. Fig. 1.3d shows each design [17]. In articulated AFOs, the plantarflexion range of motion is limited using intentional contact between the bottom of the shank and back of the foot-bed, allowing free ankle joint rotation before the limit is met. These configurations are lightweight and robust, manufactured from materials capable of absorbing energy and vibrations, such as polypropylene and carbon fibre [10, 20, 21]. Polypropylene is a popular choice due to its flexibility, allowing minor flexion in alternative rotational axes without an additional joint [20]. To manufacture an AFO, the user's leg is cast and used to form the carbon fibre

or heated polypropylene, followed by the trimming of material and joint installation if applicable [19, 22–24]. Fig. 1.3b and 1.3c show an articulated and rigid AFO manufactured using the process mentioned above.

Advances in rigid and articulated passive AFOs are limited. Instead, most research has focused on energy storage and release methods for additively manufactured rigid AFOs and multi-DOF designs as a revision of the articulated design. Rigid AFOs have been designed for additive manufacturing using 3-dimensional scanning data to create a slim and lightweight design [25] and achieve the desired stiffness for regenerative braking using embedded metal components [18]. The issue surrounding articulated AFOs is that the ankle rotation is commonly assumed to occur along an altered talocrural axis (normal to the body's sagittal plane) [22, 26, 27]. The misaligned axis results in the patient conducting a combination of plantarflexion/dorsiflexion and inversion/eversion to achieve a gait. Correction of the misaligned axis has been explored by adding suspension to a single DOF device to allow limited inversion/eversion during the gait [28]. More elaborate 2 DOF designs facilitate plantarflexion/dorsiflexion and inversion/eversion about the respective axes [10, 12].

The passive AFOs described limit the plantarflexion range of the ankle, however, the devices only reduce the effects of foot drop by failing to replace the required dorsiflexion assistance. The limited plantarflexion range reduces the adaption of steppage gait but increases the use of circumduction gait, indicated by the swinging of the hip [29]. Another category of AFOs, active AFOs (AAFO), can initiate or selectively resist ankle joint motion using linear or rotary actuators. Currently, no known market-ready AAFO is available.

1.3 Active Ankle-Foot Orthoses

An AAFO is designed to aid a patient in eliminating the effects of foot drop by selectively applying assistive or resistive torque to achieve a nominal gait cycle (see Fig. 1.2). The ideal AAFO assists in dorsiflexing the foot in the swing phase and is capable

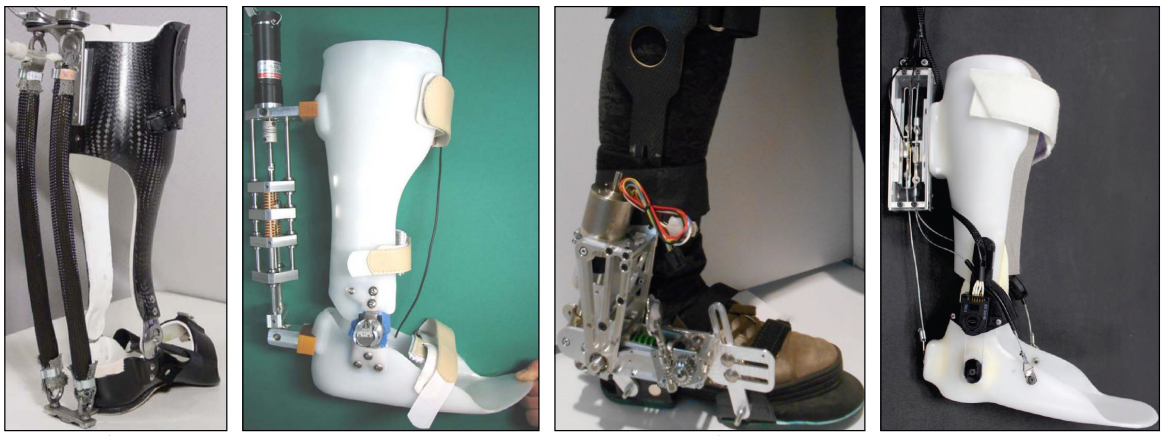

a) b) c) d)

Figure 1.4: Articulated active ankle-foot orthoses with various structures and actuators. a) Carbon fiber AAFO with pneumatic artificial muscle for plantarflexion assistance[1], b) Polypropylene AAFO with a series elastic actuator[2], c) AAFO comprised of aluminum and carbon fiber with a variable stiffness[3], and d) Articulated AAFO driven by Bowden cables for dorsiflexion and plantarflexion assistance[4].

of full plantarflexion power assistance during push-off, reducing the need for an altered gait present in AFO applications. Therefore, an AAFO must be able to provide sufficient dorsiflexion/plantarflexion assistance, all while detecting and correcting improper or undesired motion [6]. An AAFO comprises three main elements: the base mechanical design to house the calf and foot, an actuator providing assistive/resistive torque, and a control system.

The AAFO mechanical design comprises a shank, foot-bed, articulated joint, and an actuator. These designs assume the talocrural axis is normal to the sagittal plane and apply plantarflexion and/or dorsiflexion assistance via various actuator configurations (see Fig. 1.4) [8, 19, 21, 34, 35]. Advances in AAFOs mechanical designs have been limited, with AAFO research focusing on developing a powerful actuator and control system, which can later be combined into a passive AFO design. The mechanical

[1]Reprinted from Journal of biomechanics, vol. 39, Keith E. Gordon, Gregory S. Sawicki, Daniel P. Ferris, Development of an active ankle foot orthosis for the prevention of foot drop and toe drag, p.1832-1841, Copyright 2006, with permission from Elsevier [30].

[2]Development of an active ankle foot orthosis for the prevention of foot drop and toe drag, S. Hwang, [31] © 2006 IEEE, Copied from original

[3]Mechanical design of a lightweight compliant and adaptable active ankle foot orthosis, M. Moltedo, [32] © 2016 IEEE, Cropped from original.

[4]Design and evaluation of an active/semiactive ankle-foot orthosis for gait training, Y. Zhang, [33] © 2018 IEEE. Cropped from original.

structure of an AFO is sufficient for an AAFO by altering the design to include the actuator and sensors. However, designed actuators need to be lightweight while providing significant power to the ankle joint. Intelligent systems must control these actuators that only apply assistance when required. Therefore, the optimal AAFO is lightweight, capable of supplying full assistance if required, while minimizing the assistance to the user.

1.3.1 Actuation Methods for AAFOs

The main focus of AAFO actuator design is the ability to provide the desired ankle stiffness to resist undesired motion or control torque while simultaneously minimizing its mass. To apply assistive or resistive torque to an AAFO, various actuation methods, configurations, and implementations have been explored. The most common actuator being used is the series elastic actuator (SEA) and its evolution in the form of the variable stiffness actuator (VSA). Pneumatic and other actuation methods have been explored but have not been widely adopted due to the designs' power storage density and complexity.

1.3.1.1 Series Elastic Actuators for AAFOs

In the lower body, the Achilles tendon reacts in a similar nature to a tensile spring; human locomotion loads the tendon to store energy, resulting in a high tensile force within the tendon and applied torque at the ankle joint [36]. The robotic tendon actuator proposed by Hollander *et al.* [36], is an optimized SEA that is focused on the optimal loading of a linear spring during the stance phase to minimize the input power required by the SEA driving motor. The SEA was initially developed in 1995 [37]. A SEA employs an element of a known stiffness profile between the driving unit (i.e., gearbox, linear actuator) and the output (i.e., ankle joint), with the controlled output force as a function of the stiffness profile and displacement, converting a force control problem into a position control problem [37]. The first AAFO developed used a SEA with a direct-current (DC) motor and ball screw with the output link

connected to the driving link by two sets of compression springs [19]. SEAs have been continually used in AAFOs due to their safety and force capabilities. Actuator compliance, the inverse of stiffness, allows variance between the device's desired and actual position, allowing an unnatural or sudden motion to be absorbed. In addition, SEAs are intrinsically stable and allow for the filtering of high frequencies when in contact with a human [19, 38]. Previous work has found that the SEA is efficient for regenerative braking throughout the gait cycle, storing energy during the stance phase and then releasing the energy back to the user during instances of high power. The optimal SEA design may be achieved by minimizing the objective function [36]:

$$P_m = F_K \cdot \dot{\delta_K} + \frac{F_K \cdot \dot{F_K}}{K} \tag{1.1}$$

where P_m is the motor power, K is the linear spring stiffness, F_K and $\dot{F_K}$ are the axial force and change in the force of the elastic element, respectively, and $\dot{\delta}_K$ is the change in length of the elastic element. Many applications have used the basic and optimized SEAs, including active prostheses [39, 40]. However, to achieve the ultimate stiffness profile for AAFO actuation, the VSA has been implemented, closer resembling the stiffness of the ankle joint.

1.3.1.2 Variable Stiffness Actuators for AAFOs

The applied ankle torque in reference to the ankle angle is nonlinear. Therefore, a linear spring is insufficient to recreate the normal ankle stiffness. VSAs have been developed to apply a nonlinear or adjustable stiffness. Designs range from linear spring and linkage configurations to cantilever beams and magnetic antagonistic configurations.

VSAs can be separated into two types. The first uses a linear stiffness element to achieve variable stiffness at the ankle joint using mechanical configurations. An example is the rotary VSA designed in [41] and implemented for an AAFO in [32] (see Fig. 1.4c). The actuator applies a torque when the angle between the driven and output link is non-zero, with the torque to angle differential expressing a nonlinear

relationship. The design had a maximum output torque of 25 Nm and a mass of 1.7 kg. Another example is a passive actuator for an AFO in which linear springs are mounted between a fixed and rotating plate. The stiffness is altered by rotating the plate, resulting in a nonlinear force vs displacement characteristic [42]. Gear and cam-based VSAs have also been developed with linear springs. Combining a gear, ballscrew, and linkage combination, Dong *et al.*, stored energy within a linear spring, which reduced the peak input power to an ankle prosthesis by 34% [43]. A complex cam-based VSA is presented in [44], where the rotation of the cam alters the distance between the pivot point and spring points of contact on the output link, resulting in a varied stiffness.

The second type uses known material and magnetic properties to create a varying stiffness. Using the known stiffness of a parabolic beam, Shao *et al.*, developed a VSA based on the interaction between a designed cam and two parabolic beams with the stiffness as a function of beam deflection, depicted in Fig. 1.5 [45]. The design had a mass of 0.77 kg with a peak torque output of 60 Nm. Other works have explored magnetic antagonistic configurations, such as [46], which modulated stiffness by altering the distance between opposing magnets. The configuration has a mass of 1.2 kg with a maximum applied torque of 1.95 Nm.

While VSAs can assist the ankle joint, their implementation results in a bulky and heavy final product. Therefore, with the mean AAFO design mass of 1.69 kg, research has also explored lightweight pneumatic options of actuation [47].

1.3.1.3 Pneumatic Actuators for AAFOs

Pneumatic actuators have been widely used in AAFOs due to their high force-to-weight ratio. The McKibben muscle, also known as the pneumatic artificial muscle (PAM), is an actuator that uses air pressure to generate a tensile force, mimicking the

[1]Reprinted from Journal of Mechanism and Machine Theory, vol. 161, Yixin Shao, Wuxiang Zhang, Yujie Su, Xilun Ding., Design and optimisation of load-adaptive actuator with variable stiffness for compact ankle exoskeleton, Article 104323, Copyright 2021, with permission from Elsevier [45].

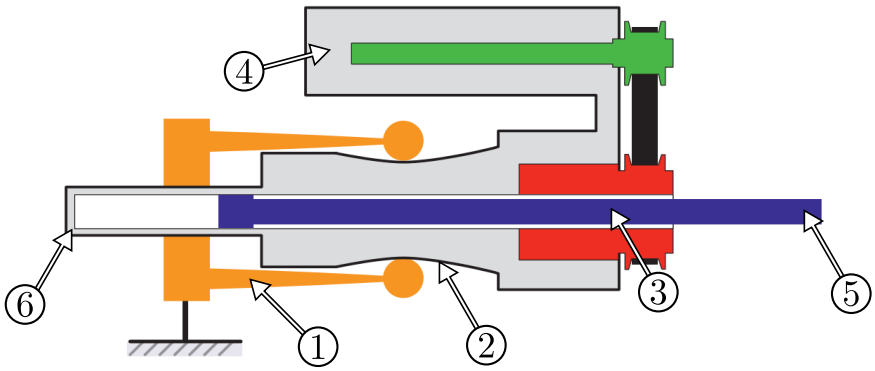

Figure 1.5: Parabolic beam VSA for an ankle exoskeleton[1]. The parabolic beams ① are loaded by the cam ② in tension and compression. The ballscrew ③ alters the length of the actuator using a DC motor ④ to create tension or compression in the actuator, where ⑤ attaches to the exoskeleton shank and ⑥ connects to a lever arm on the foot-bed.

muscle characteristics of a human [30,48]. Many pneumatic driven AAFO designs have two PAMs to assist both the calf and tibialis anterior muscles [24, 35, 48]. However, some methods only use one actuator to assist the calf in plantarflexion [30].

Thanks to their high force-to-weight ratio, pneumatic actuators have been extensively used in multi-DOF AAFOs [47, 49, 50]. For example, two pneumatic bladders may be used to aid in plantarflexion and support inversion/eversion motion again, mounting one bladder on either side of the foot [49]. To control both plantarflexion/dorsiflexion and inversion/eversion, the number of actuators may be increased [50]. Such as [50], which used four PAMs controlled in tandem to assist motion in 2-DOF, thereby eliminating the need for bearing components, metallic and/or plastic materials. To reduce the number of actuators while maintaining 2 controlled DOFs, [47] proposed a mechanical configuration, where two PAM actuators provided plantarflexion assistance and inversion/eversion control

Further, passive AFOs have been developed with pneumatic components, which utilize bellows to generate pressure within the system [8]. The pressure then activated a pneumatic cylinder to lock and unlock the ankle joint during specific gait phases [8]. Another approach is [26], which utilizes a cam and ratchet mechanism to store and release energy within the PAM. Although pneumatic actuators have a high force-to-weight ratio and can apply sufficient torque, utilizing them in a wearable device is

challenging, as a supply of compressed air is required to apply the actuation force. In order to facilitate sufficient torque for a standalone system, various other actuation methods have been attempted.

1.3.1.4 Other Actuation Methods

Alternative actuation methods were developed but have not been widely adopted. An example is magnetorheological (MR) brakes to apply resistive torque during the gait cycle [1, 51]. The ankle joint is locked during the stance phase to store energy within the spring and unlocked to release the stored energy during push-off [1]. A rotary voice coil actuator at the ankle joint has also been considered to apply assistance [52]. Further, an internal combustion walking engine was also proposed by [53] to apply full plantarflexion assistance using a modified pneumatic cylinder as a combustion chamber for propane. Upon ignition and plantarflexion assistance, the exhaust is routed to a second cylinder to be used for dorsiflexion assistance.

The aforementioned methods of actuation have proved to be feasible in a research context. However, to move towards a market-ready solution, the focus of research must shift towards creating a lightweight and power-efficient actuator located in a discrete manner.

1.3.2 AAFO Control

The most commonly used control methods for AAFOs can be divided into four categories: electromyography (EMG) control, gait phase control, variable impedance control, and trajectory control. Each controller is beneficial in assisting/resisting the user's ankle to achieve a nominal gait; however, they differ from one another with regards to input variables and methods of control (i.e., impedance vs trajectory-based).

1.3.2.1 Electromyography-Based Control

AAFO control using EMG signals is simple to implement in a controlled environment. EMG is the measurement of muscle activation using a surface electrode placed on the

periphery. In EMG-base control, also known as myoelectric control, the measured muscle activation signal is amplified by a proportional gain and used as the desired input to a controlled system [35, 48, 54, 55]. Adaptive gains have been explored, with adjustments based on the peak measured EMG values within a set time frame [55]. Despite these explorations, no significant advancements have been made in EMG-controlled AAFOs, as it is only effective if muscle activation can be measured.

1.3.2.2 Gait Phase Control

The gait phase controller uses information from ground contact sensors to determine the current gait phase of the user and apply a designated control output [56, 57]. The controller segregates the gait into three main phases: powered dorsiflexion during the swing phase, minimal assistance during the stance phase, and powered plantarflexion at the end of the stance phase [35, 56, 57]. A sequence of ground reaction force (GRF) triggers deciphers the gait phases, commonly measured by force-sensitive resistors on the sole of the paretic foot [56]. The GRF sensors are commonly used in pairs of two and are mounted at the heel and toe of the paretic foot but may also be installed under both feet to better segment the gait phase [49, 56, 58]. Similarly, a passive pneumatic actuator with two pneumatic switches on the heel and toe has been demonstrated to provide sufficient information to determine the gait cycle and control the AFO without the need for any electronics [8]. Although the control scheme of the gait phase controller is relatively simple, it is used as the base and guide for variable impedance and trajectory control methodologies.

1.3.2.3 Variable Impedance Control

Variable impedance control exploits the fact that the foot impedance changes throughout the gait cycle. Previous works have divided the gait into the three phases outlined above [1, 51, 59], where each phase results in a different impedance for the AAFO. In [59], a three-phase impedance control method was implemented to keep a required tension or compression in the springs of a SEA. The phases consisted of impedance

controlled plantarflexion to reduce foot slap, zero impedance control during the stance phase, and variable impedance to control the ankle angle during the swing phase [59]. Similarly, an MR brake may be used to create variable damping or lock the ankle joint of an AFO designed for ascending and descending stairs [51]. Another work implemented a two-phase system, which applied low impedance from flat foot to toe-off and high impedance toe-off to flat foot [21].

1.3.2.4 Trajectory Control

Trajectory control is the most widely utilized control method in the literature. Fig. 1.2 shows the distinct gait trajectory of the ankle, in which multiple controllers have been developed to track the angular trajectory. The popular proportional-integral-derivative (PID) controller has been implemented for trajectory tracking [58,60]. However, the PIDs are tuned for a stiff response in the fast-moving system, resulting in high torque output in the presence of low tracking error. Therefore, more advanced control methods have been explored to track the trajectory. An improved PID used a proxy-based slide mode controller to filter the desired position while simultaneously tuning the gains of a PID controller to track the filtered trajectory [14]. Other methods, such as backstepping control, have also been used to track the angular trajectory [40]. Although these control methods can reduce the tracking error of undisturbed systems, the ankle joint can be subject to a large disturbance torque during locomotion. This disturbance is due to the expected push-off force of the ankle to propel the user forward. A disturbance torque is present at the ankle joint if the user is unable to apply the propulsion torque, as the rest of the body translates the expected force to the lower leg for locomotion.

Active disturbance rejection control (ADRC) [61] has been implemented in an AAFO and ankle exoskeleton by [62] and [63] for its ability to reject all disturbances acting on the system. In [64], a sliding mode controller (SMC) is combined with an ADRC to minimize the chattering effect of the high SMC switching gain for an ankle in the presence of disturbance [64]. An ADRC encompasses an extended state observer

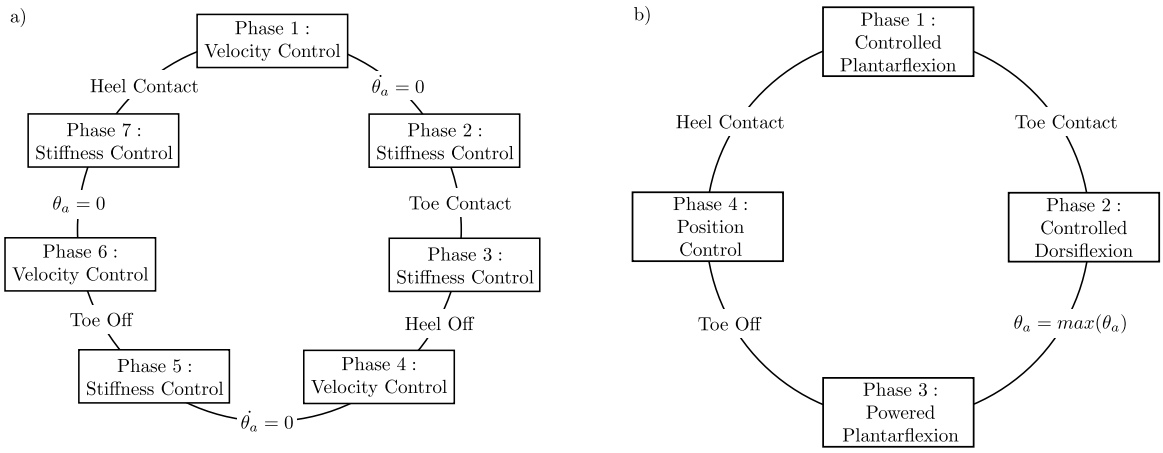

Figure 1.6: Two examples of gait phase control systems that encompass stiffness control, velocity control, and position control. a) Demonstrates a seven gait phase control system developed by [39]. b) Illustrates a four gait phase control scheme presented by [66], where θ_a is the angle of the ankle joint, and $max(\theta_a)$ is the point of maximum dorsiflexion.

(ESO) in which the extended state multiplied by the inertial component is the total observed disturbance applied to the system, creating an estimate of the induced disturbance [61]. The ADRC can be combined with most trajectory tracking algorithms to reduce the tracking error due to unknown disturbances.

To create a smooth angular trajectory from the user's current position to distinct instances of the gait cycle, adaptation of the angular trajectory has been proposed [2, 14]. When a change in the gait phase occurs, the controller recomputes the desired trajectory using a cubic spline and specified angular targets throughout the gait cycle [2, 14]. The time between each phase is then used to map the duration of the proceeding phases [2, 14].

Trajectory control is not always based on the ankle angle. Many control schemes such as the ones presented in [38, 39, 65] follow a torque or force trajectory. Trajectory control schemes can be split into multiple gait phases like the variable impedance method. Boehler *et al.* [39], developed a seven gait phase controller, depicted in Fig. 1.6a, that relied on a combination of variable impedance and variable angular velocity based on the current gait phase . A similar force controller was developed by Jardim *et al.*, using the gait phase division from [66] (see Fig. 1.6b), creating the resultant torque by monitoring the speed and position of a spring [38].

1.3.2.5 Adaptive Control

It is well-known that highly nonlinear disturbances are present when tracking the angular trajectory. Additionally, the plant parameters of the AAFO in combination with the ankle cannot be directly measured, resulting in increased disturbance in the form of modelling uncertainties [62].

Previous research has focused on modelling and rejecting the disturbance torque through adaptive control laws. Many approaches have been explored to model the gait disturbance adaptively. In [40], the disturbance was modelled by summing numerous sine waves of varying scales, frequencies, and phase shifts. Another work modelled the disturbance as a combination of feasible disturbance torque origins, such as friction, gravity, inertia, etc. [2]. The adaptive control laws scale the respective disturbance sources to minimize the error between the actual and modelled disturbance based on the s-plane used in SMC and measured variables, including the acceleration, velocity, and position of the desired trajectory and current ankle velocity and position [67]. Other works have developed models to determine the plant parameters, such as an adaptive SMC to estimate the stiffness and damping parameters of the whole control system in reference to the employed SEA [68].

1.4 Towards Optimal Actuation and Control of an AAFO

The optimal AAFO is lightweight and responsive but not overbearing, as a productive rehabilitation process requires active user engagement, such that a student and teacher relationship is present [69]. The primary source of weight in the AAFO is the employed actuator, increasing the metabolic cost of locomotion. The ideal AAFO actuator is lightweight yet capable of providing full power assistance. Previous works have employed optimized stiffness elements to minimize the peak input power, directly related to the driving motor's mass and size. The peak input power is maintained only for a short time [36, 70], and thus other stiffness methods can be employed to

maintain the peak power for an extended time to increase the efficiency of regenerative braking. Others developed variable stiffness actuators capable of providing a range of stiffness to assist the user but result in a heavy and complex mechanism. However, optimizing a variable stiffness element for regenerative braking has not been presented.

Optimal control of an AAFO is resistant to disturbances, can identify the unmeasurable time-variant model parameters, and limits its assistance to the user. Previous control systems focus on minimizing the trajectory tracking error by modelling the cyclic disturbance to the system and compensating for them in the controller. However, these disturbances are time-variant in a normal locomotion environment. To identify the model parameters, adaptive controllers are implemented to minimize the trajectory tracking error, which requires aggressive trajectory tracking methods. The main control methods of AAFOs depend only on the tracking error and do not consider the torque being applied to the user, which must also be minimized.

Consequently, this thesis is divided into four objectives: (1) Minimization of the actuator mass and size, (2) identification and rejection of the applied disturbance, (3) estimation of time-variant AAFO model parameters, and (4) a control method capable of limiting assistance interactions with the user. To obtain the objectives, this thesis is structured in the following manner:

Chapter 2 proposes a low-power actuator for AAFOs capable of recreating the torque and power profile of the ankle joint while reducing the input power. The actuator uses a novel discrete nonlinear SEA that engages multiple linear stiffness elements to optimize its regenerative braking and energy application capabilities. The design uses a crank-rocker four-bar mechanism, in which the motor and gearbox drive the crank, and the rocker is connected to the ankle joint. The connecting link employs the variable stiffness element, where one linear spring provides constant stiffness, and another is engaged when the link surpasses a specified length. The design surpasses the optimized permutations of the parallel elastic actuator (PEA) and SEA combinations, which saw a 70% decrease in the peak input power compared to the biological ankle joint power [71]. Implementing a uni-direction PEA employed with a SEA further

reduces the peak power input by 74.4% in comparison to a direct-drive design [70]. An AAFO is developed and manufactured to test the actuator model. The proposed discrete nonlinear actuator is optimized to minimize the peak motor power and total link length. The optimization achieves the first thesis objective of mass minimization, as a low peak power reduces the motor and gearbox size and weight, and link length minimization enables a tight form factor.

Chapter 3 presents an adaptive ESO to estimate the disturbance experienced by the plant while estimating the model parameters, achieving the next two objectives. To reject disturbance to the system, an ESO is employed. The rejected disturbance is a combination of external disturbances and internal disturbances due to the error in plant modelling. In an AAFO, the plant model is time-variant and unmeasurable. Therefore, the adaptive ESO extracts the disturbance due to the plant modelling error by subtracting the scale nominal gait torque (see Fig. 1.2) from the measured disturbance. Adaptive laws then adjust the respective inertial and damping parameters to minimize the error between the nominal and measured disturbance torque. The proposed adaptive control system is based on the error in the cyclic disturbance rather than the trajectory tracking error, allowing the central controller to focus on the optimal trade-off between trajectory tracking and required assistance. The developed adaptive ESO can identify the AAFO plant parameters and estimated disturbance, subsequently decreasing the trajectory tracking error.

Chapter 4 describes a nonlinear model predictive controller (MPC) for an AAFO, addressing the final objective of the thesis. The previously proposed trajectory tracking control methods for AAFOs have solely focused on minimizing the trajectory tracking error. The presented MPC controller allows for the optimal trade-off between assistance and trajectory tracking, with the ability to proactively assist the user. The average gait cycle occurs in 1.1 s in which many significant acceleration instances are present [9]. An MPC controller has knowledge of the upcoming ankle trajectory, known as the prediction horizon, and optimizes a set of control variables to achieve the trajectory, known as the control horizon. The control variables are determined by

minimizing a cost function containing the tracking error and control effort, therefore, trajectory tracking error and applied assistance can both be minimized. To ensure real-time operation of the MPC controller, fast optimization methods are required, with close initial estimation of the optimal control horizon. This thesis proposes a method to determine the initial control horizon, the cost function to be minimized for trajectory tracking of an AAFO, and a fast optimizer to quickly identify to optimal control horizon. The implemented MPC controller can reduce the trajectory tracking error by 58.3% compared to a proportional-derivative (PD) controller with high gains while operating in real-time at a frequency of 100 Hz.

Chapter 5 summarizes the work presented in the thesis and proposes avenues for future work.

Chapter 2

Design of a Novel Variable Stiffness Actuator for Active Ankle-Foot Orthoses

Reprinted, with permission, from B. DeBoer, A. Hosseini, and C. Rossa,

A Discrete Non-linear Series Elastic Actuator for Active Ankle-Foot Orthoses,

IEEE Robotics and Automation Letters, in press, 2022

THE ankle joint is subject to a peak biological power of 263 W for an 80 kg user with a step speed of 1.1s, rendering direct-drive systems bulky and impractical [9]. The goal of the AAFO actuator is to provide the required power to the ankle joint while minimizing the size and mass of the design. Elastic actuators, such as SEA and VSA, allow a safe and controllable torque or force to be provided to a user during human-machine interaction.

Previous research has shown that AAFOs significantly benefit from regenerative braking; energy is stored in an elastic element during the early portion of the stance phase and released to the patient at push-off [36]. Previously designed AAFO actuators utilize regenerative braking to provide significant input power reduction with a linear SEA. Other works have explored the combination of SEA, uni-directional and directional PEA to minimize the input power to the AAFO [70], resulting in a 74.4% input power reduction compared to the peak biological ankle power. To recreate the stiffness profile of the ankle joint, VSAs are employed to generate the desired stiffness throughout the gait cycle. However, these actuators are becoming increasingly complex, as outlined in Chapter 1. These designs are beneficial for ankle-foot prostheses as the mass of a prosthesis can be designed to match the mass of the amputated limb. In the case of AAFOs, the user's lower limbs are present, resulting in a significant increase in the metabolic cost of walking due to the actuator's mass [72]. The use of a SEA for peak input power reduction and VSA for stiffness variation has not been thoroughly explored.

The design of an AAFO actuator must be focused on mass minimization while still providing the required assistance. The objective can be reached by minimizing the size and complexity of the actuator while reducing the peak required power, consequently reducing the size of the driving motor. The elastic element connecting the motor to the ankle joint can also be further explored to minimize the size and weight of a functional AAFO.

This Chapter outlines the design of an optimal VSA for AAFOs. Two actuator topologies are explored, using a pre-inflated PAM as the elastic element, followed by the

conceptualization of the novel discrete nonlinear stiffness element. These elements target the optimal combination of the optimized SEA and VSA. The slider-crank and crank-rocker topologies are explored to determine the best configuration for mechanical and electrical power reduction.

The Chapter is structured as follows: Section 2.1 describes the two actuator topologies, section 2.2 proposes two variables stiffness elements and presents initial results. The optimization of the discrete nonlinear stiffness element in a crank-rocker is presented in section 2.3, with a discussion of the optimization results in section 2.4. An AAFO prototype is presented and manufactured in section 2.5 to conduct experimental tests in section 2.6. Concluding remarks are presented in section 2.7.

2.1 AAFO Actuator Configurations

Four-bar mechanisms are a fundamental aspect of SEAs and VSAs, decoupling the motor and ankle joint with a compliant connecting link. The slider-crank four-bar mechanism has been widely used in AAFO literature, in which a slider driven by a ballscrew induces linear motion, a compliant link connects the slider and crank, and the crank is mounted to the foot-bed of the AAFO. While the slider-crank mechanism is popular, other four-bar mechanisms can be considered due to their intrinsic properties.

An inherent property of the crank-rocker mechanism is the torque required by the crank during a rotation. When the crank and coupling links are parallel, the driving torque is reduced to zero. Consequently, a crank-rocker mechanism has the potential to reduce the input power for an AAFO. There has been no implementation of a crank-rocker four-bar mechanism in AAFOs, where active ankle prostheses have used the configuration for regenerative braking [73]. The design proposed in [73] utilized the mechanical advantage inherent to the crank-rocker mechanism, reducing the input torque by aligning the crank and connecting link. The goal was to reduce the mass,

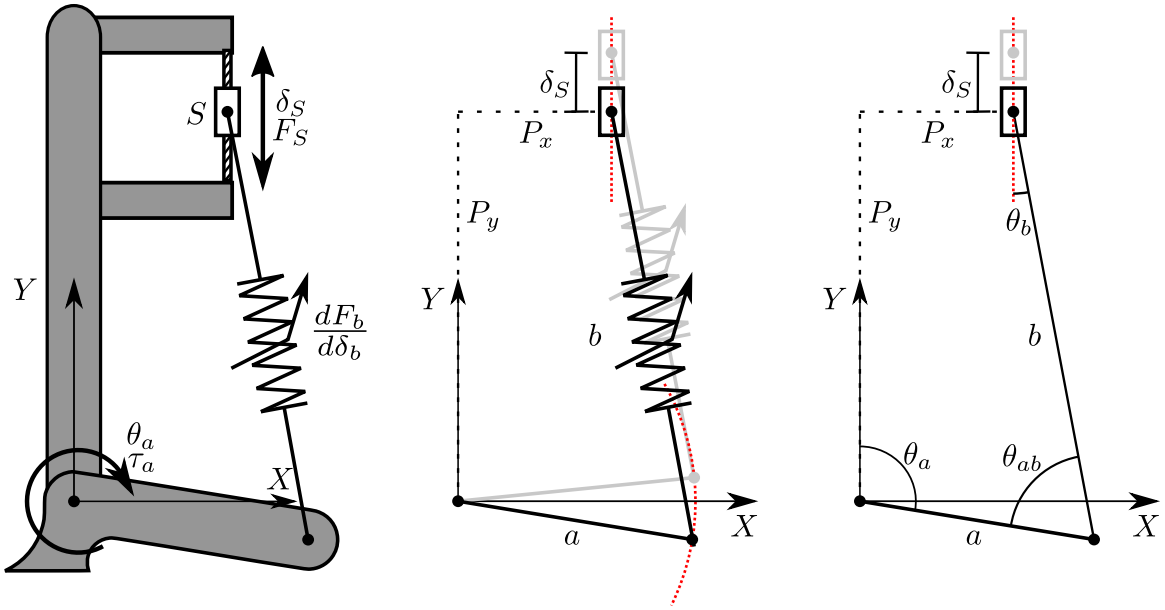

Figure 2.1: Slider-crank actuator topology, in which the slider at point (P_x, P_y) is driven by a lead screw to generate displacement δ_S. The displacement of the slider generates an axial force within connecting link b, joining the slider to link a. The axial force in b directly results in a torque at the origin, representing the ankle joint.

peak power, and energy consumption required to apply full biological power to the ankle joint.

To analyze the effects of implementing a slider-crank and crank-rocker configuration on AAFO actuation, the angular and torque trajectory for the ankle joint presented in Fig. 1.2 can be referenced as the desired output trajectory and applied torque, simulating full assistance for a nominal gait.

2.1.1 Slider-Crank Configuration

A slider-crank SEA actuator, depicted in Fig. 2.1, employs a motor and ballscrew to translate the slider (S). Link b transmits the force (F_S) and displacement (δ_S) of the slider to the crank (a), which rotates about the ankle joint. The applied force (F_S) on the slider and torque (τ_a) at the ankle joint can be determined by analyzing the displacement (Δb) and stiffness ($\frac{dF_b}{d\Delta b}$) of compliant link b.

To track the angular position (θ_a) and torque (τ_a) of the gait trajectory, the displacement of the slider (δ_S) and axial force (F_S) throughout the trajectory can be

determined, with the applied power (P_{SC}) of the slider expressed as:

$$P_{SC} = \frac{d\delta_S}{dt} F_S. \tag{2.1}$$

Since the actuator is designed to apply the required torque for a known angular and torque trajectory, the trajectories are discretized, and the respective slider position and force are solved using the following series of equations.

The force in compliant link b (F_b) to achieve torque τ_a is determined by the required ankle joint position and the angle (θ_b) of link b as:

$$F_b = \frac{\tau_a}{a \sin(\theta_a - \theta_b)} \tag{2.2}$$

resulting in the extension or compression of compliant link b to the length:

$$b = b_0 + \Delta b \tag{2.3}$$

where

$$\Delta b = \frac{F_b}{\frac{dF_b}{d\Delta b}} \tag{2.4}$$

and b_0 is the initial length of link b. The angle of θ_b is then determined from:

$$\theta_b = \arcsin\left(\frac{a \sin\theta_a - P_x}{b}\right). \tag{2.5}$$

Since θ_b is dependent on b and thus F_b, and F_b is dependent on θ_b, θ_b is initially assumed as 0, and Eqs. (2.2) to (2.5) are iterated, with θ_b updated as:

$$\theta_b(i+1) = \alpha \underbrace{(\theta_b(i) - \theta_b(i-1))}_{\text{error}} + \theta_b(i-1), \tag{2.6}$$

where $\alpha \in [0, 1]$ is a scalar modified for convergence, and i is the current iteration. A solution is seen as acceptable when the error between $\theta_b(i-1)$ and $\theta_b(i)$ is within a set tolerance. Once θ_b is determined, the displacement of the slider (δ_S) is calculated

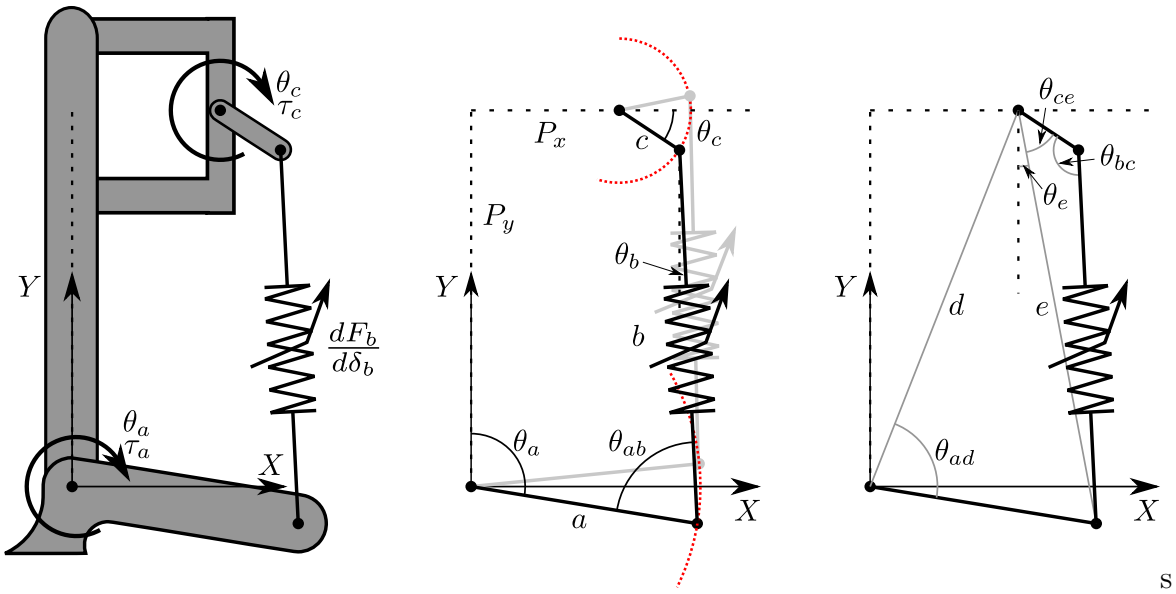

Figure 2.2: Crank-rocker actuator topology, in which a motor mounted at point (P_x, P_y) drives rotational link a, creating tensile or compression in connecting link b between the ends of link a and c. The axial force generated in b directly results in a torque at the origin, representing the ankle joint.

as:

$$\delta_S = a\cos\theta_a + b\cos\theta_b - P_y \tag{2.7}$$

with the axial driving force of the slider evaluated as:

$$F_S = \frac{F_b}{\cos\theta_b}. \tag{2.8}$$

The speed $\frac{d\delta_S}{dt}$ of the slider is then determined based on time (t) required to take a step to evaluate and Eq. (2.1). Using the above formulations, the power required by the slider can be minimized by optimizing the stiffness ($\frac{dF_b}{d\Delta b}$) of link b.

2.1.2 Crank-Rocker Configuration

The crank-rocker SEA actuator, see Fig. 2.2, is driven by a crank (c) and is connected to the rocker (a) using a compliant link b. The rocker rotates about the ankle joint and is fixed to the foot-bed, providing angular motion (θ_a) and torque (τ_a). The

power required by the crank is determined by:

$$P_{CR} = \frac{d\theta_c}{dt}\tau_c \tag{2.9}$$

where the position θ_c and torque τ_c at the rotation point of link c can be solved for a discretized trajectory. The crank-rocker mechanism is solved in a similar manner to the slider-crank, with the added complexity of a rotary driving link. The force within link b (F_b) and subsequent displacement (Δb) is found using Eqs. (2.2) - (2.4), with:

$$\theta_b = \arctan\left(\frac{a\sin\theta_a - P_x - c\cos\theta_c}{a\cos\theta_a - c\sin\theta_c + P_y}\right). \tag{2.10}$$

To determine the position θ_a, the crank-rocker mechanism can be separated into two triangular sections, shown in Fig. 2.2, where the unknown lengths d and e of triangle dec can be determined with the rotational point of link a (P_x, P_y) and θ_a, as:

$$d = \sqrt{P_x^2 + P_y^2} \tag{2.11}$$

and:

$$e = \sqrt{a^2 + d^2 - 2ad\cos\left(\theta_{ad}\right)}, \tag{2.12}$$

with angle between links a and d determined by:

$$\theta_{ad} = \theta_a - \arctan\left(\frac{P_x}{P_y}\right). \tag{2.13}$$

Therefore, the position of link c, is found to be:

$$\theta_c = \theta_{ce} + \theta_e - \frac{\pi}{2} \tag{2.14}$$

where θ_{ce} is the angle between link c and calculated length e as:

$$\theta_{ce} = \arccos\left(\frac{e^2 + c^2 - b^2}{2ce}\right) \tag{2.15}$$

and θ_e is the angular position of link e relative to the Y axis, determined by:

$$\theta_e = \arctan\left(\frac{P_{Ax} - P_x}{P_{Ay} + P_y}\right). \tag{2.16}$$

Eq. (2.10) can be evaluated with the known position θ_c. Once again, F_b is dependent on θ_b, where θ_b is also dependent on θ_c. Additionally, θ_c depends on the length of link b and thus on F_b. Therefore, the iteration method for θ_b presented in Eq. (2.6) is used. Eqs. (2.2) - (2.4), (2.10), and (2.14) - (2.16) are iterated until a set error is reached. Finally, the torque of link c can be defined as:

$$\tau_c = cF_b \sin\left(\theta_c + \frac{\pi}{2} - \theta_b\right). \tag{2.17}$$

The angular speed ($\frac{d\theta_c}{dt}$) is then determined for the specified gait time (t), and the power required by the crank is determined using Eq. (2.9).

2.1.3 AAFO Topology Comparison

It is known that the SEA can reduce the mechanical input power to an AAFO [36]. However, when considering the electrical power reduction, the crank-rocker mechanism has the benefit of reduced holding torque when links a and c are parallel. A simulation of the mechanical and electrical power required for a slider-crank and crank-rocker mechanism is conducted to analyze the electrical power and energy required. The simulation tracks the actuator's motor position profile while a simulated torque is applied to either the slider-crank or crank-rocker configuration. Both simulations use the same brushed DC motor (Maxon RE 35 - 24V - 150W). The slider-crank mechanism is equipped with a ballscrew (THK BNK1208, 8 mm pitch, 90% efficiency) mounting to a planetary gearbox (Maxon GP42C - 15 : 1 reduction, 81% efficiency). The combination is required to generate the torque to overcome the maximum force applied in the axial direction of the slider. The highest feasible planetary gearbox ratio (Maxon GP42C - 66 : 1 reduction, 72% efficiency) is selected for the crank-rocker configuration. The results, shown in Fig. 2.3 and Table 2.1, indicate that the

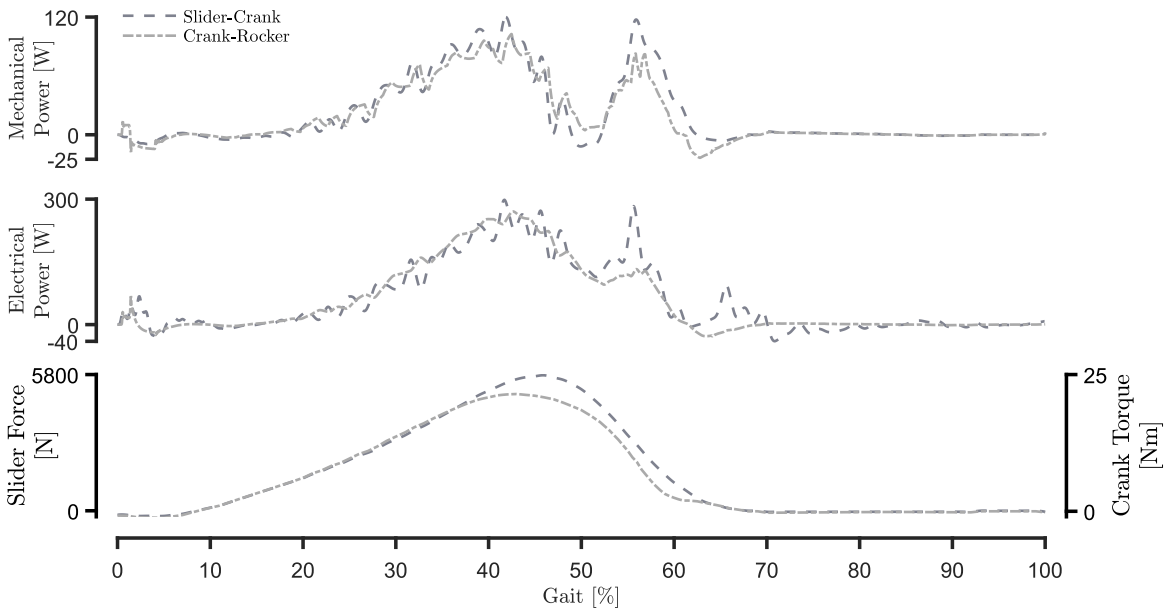

Figure 2.3: Simulated slider-crank and crank-rocker mechanical and electrical power comparison. The slider force and crank torque show the benefits of a crank-rocker mechanism in reducing the holding torque at instances of high biological ankle power.

Table 2.1: Slider-crank & crank-rocker electrical simulation results

Actuator	Peak Electrical Power	Peak Mechanical Power	Electrical Energy
Series elastic slider-crank	298.41 W	120.04 W	94.48 J
Series elastic crank-rocker	270.52 W	102.73 W	50.91 J

crank-rocker mechanism leads to the lowest electrical power and energy required by the motor. The crank-rocker is more efficient due to the reduced torque when links a and b are parallel, whereas the motor driving the slider-crank is always reacting to a large torque as a function of the force within link b, presented at the bottom of Fig. 2.3.

Therefore, the crank-rocker is a beneficial SEA topology for an AAFO. The inherent characteristic of decreased holding torque at high instances of gait power reduces the electrical power required to apply full assistance. One can now target a simple and compact variable stiffness element to further minimize the input power to the device, where the power reduction is strongly coupled to the optimal stiffness of the compliant link, investigated in the following section.

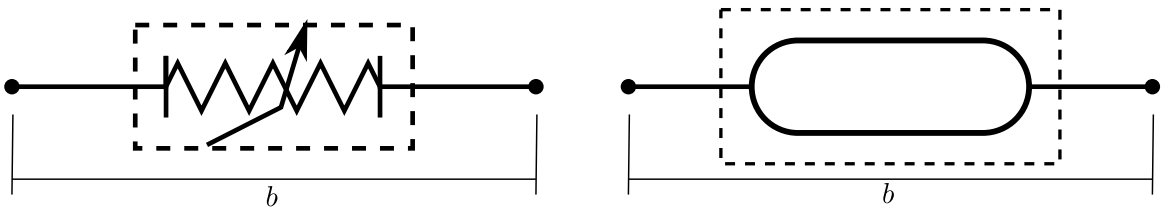

Figure 2.4: A PAM compliant link b, consisting of a pre-inflated PAM as the stiffness element.

2.2 Design of a Variable Stiffness Element

The stiffness element ($\frac{dF_b}{d\Delta b}$) in the proposed topologies is typically a linear or variable stiffness element described in Section 1.3.1.2. This section aims to identify a compact stiffness element optimized for regenerative braking via a nonlinear variable stiffness design. Two stiffness elements are explored, a pre-inflated PAM and the novel discrete nonlinear element.

2.2.1 Pre-Inflated Pneumatic Artificial Muscle for Variable Stiffness

PAMs are widely used in AAFOs to apply assistive torque. In operation, compressed air is applied to the PAM causing the internal bladder to expand in the radial direction, resulting in an axial contraction. A pre-inflated PAM has a nonlinear force vs. displacement relationship given by [74]:

$$F_{PAM}(\delta_{PAM}) = A_1 e^{\frac{-\delta_{PAM}}{t_1}} + A_2 e^{\frac{-\delta_{PAM}}{t_2}} + F_{0_{PAM}} \tag{2.18}$$

where A_1, A_2, t_1, t_2 and $F_{0_{PAM}}$ are curve fitting constants and δ_{PAM} is the axial displacement of the PAM. The stiffness profile can be altered by adjusting the pre-inflation pressure. Using the PAM as a stiffness element within the series elastic crank-rocker configuration (see Fig. 2.4) could result in an actuator with a reduced peak input power. With this method, Leclair *et al.*, developed an unpowered AFO using a pre-inflated PAM to conduct regenerative braking [26]. The design used a

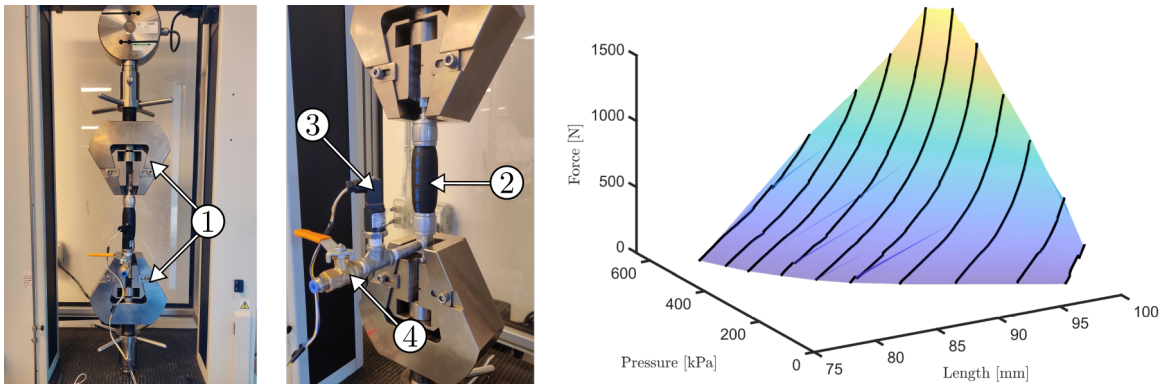

Figure 2.5: Left: Stiffness measurement of a PAM using the LLOYD tensile test machine ①. The PAM ② is pre-inflated to a set pressure, measured by a pressure sensor ③, sealed by a shutoff valve ④, and placed in the jaws of the machine. The machine then displaces the difference between the pressured and unpressurized PAM length. Right: The resulting force, displacement, and PAM internal pressure from the conducted tests. Measured data is presented as the plotted black lines, interpolated to generate the surface plot.

ratchet mechanism to store elastic potential energy within the PAM, benefiting from the PAM's nonlinear force vs. displacement relationship.

Physical testing was completed with a pre-manufactured PAM containing a 100 mm unpressurized bladder length (Festo Fluidic Muscle to determine the feasibility of applying a PAM as a nonlinear stiffness element DMSP-20-100N-RM-CM). The total length of the pre-manufactured PAM is 235 mm, encompassing the bladder, pneumatic ports, and mounting points (see Fig. 2.5). The stiffness of the PAM was experimentally determined using a tensile test machine (LLOYD LS100), in which the PAM was pre-inflated with a set pressure, and the initial displacement was measured. The PAM was sealed before fastening the two ends within the jaws of the tensile test machine. The length of the tensile test was determined by subtracting the measured length of the compressed muscle from the initial PAM length. Tests were started with the initial pressure of 100 kPa and continued to 550 kPa at 50 kPa increments, recording the PAM's force, displacement, and internal pressure. The results are presented in Fig. 2.5, demonstrating the PAM's nonlinear force vs displacement curve. It is evident that the stiffness of the pre-inflated PAM actuator is a function of the internal pressure and displacement.

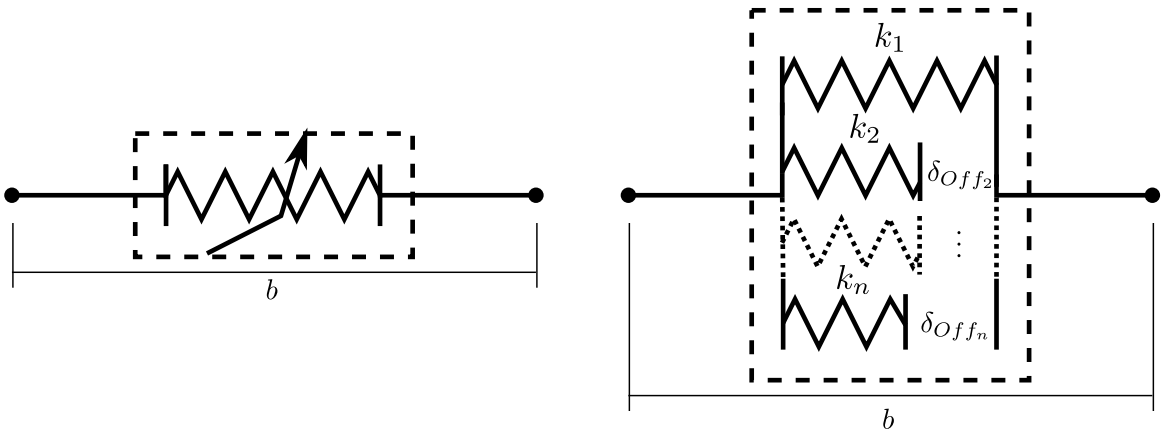

Figure 2.6: The discrete nonlinear compliant link, in which link b has stiffness k_1 until the displacement δ_{Off_2} is reached and $k_1 + k_2$ until δ_{Off_3} is achieved, in which the stiffness has another discrete change.

If used as the stiffness element in a SEA, the stiffness of compliant link b can be expressed as:

$$\frac{dF_b}{d\Delta b} = \frac{F_{PAM}(\Delta b, P_{PAM})}{\Delta b}, \tag{2.19}$$

where $F_{PAM}(\Delta b, P_{PAM})$ is the tensile force within the pneumatic muscle at displacement Δb and internal pressure P_{PAM}, obtained by interpolating the measured data.

2.2.2 Discrete Nonlinear Design for Variable Stiffness

The second proposed elastic element design is a novel discrete nonlinear stiffness, building on the advances of a uni-directional PEA for power reduction. The discrete nonlinear method is simple: a set of linear springs are engaged in parallel at discrete displacement intervals to generate the optimal trade-off between power consumption and actuator mass.

A visual representation of the discrete nonlinear design can be seen in Fig. 2.6. The design is hypothesized to reduce the input power to the AAFO by obtaining the optimal stiffness and displacement values using a select number of linear springs. The configuration allows the nonlinear stiffness of the ankle joint to be approximated with

various linear segments. The stiffness can be represented as follows:

$$\frac{dF}{d\Delta b} = \begin{cases} k_1, & \text{if } \Delta_b < \delta_{Off_2} \\ k_1 + k_2, & \text{if } \Delta_b < \delta_{Off_3} \\ \vdots & \vdots \\ \sum_{i=1}^{n} k_i, & \text{if } \Delta_b < \delta_{Off_n} \end{cases} \tag{2.20}$$

where $[\delta_{Off_2}, \ldots, \delta_{Off_n}]$ is a continually increasing vector representing the discrete distance in which each spring activates, $[k_1, \ldots, k_n]$ is the positive definite linear spring stiffnesses, and n is the number of employed springs. The resulting displacement of link b is determined by:

$$\Delta b \begin{cases} \frac{F_b - F_{Limit}(0)}{\sum_{j=1}^{1}[k_j]}, & \text{If } F_b < F_{limit}(1) \\ \delta_{Off_2} + \frac{F_b - F_{Limit}(1)}{\sum_{j=1}^{2}[k_j]}, & \text{If } F_b < F_{limit}(2) \\ \vdots & \vdots \\ \delta_{Off_n} + \frac{F_b - F_{Limit}(n-1)}{\sum_{j=1}^{n}[k_j]}, & \text{If } F_b < F_{limit}(n) \end{cases} \tag{2.21}$$

governed by:

$$F_{Limit}(n) = \sum_{i=1}^{n} \left[\sum_{j=1}^{i} [k_j] \left(\delta_{Off_{i+1}} - \delta_{Off_i} \right) \right] \tag{2.22}$$

The discrete change in stiffness allows few or many springs to approximate a nonlinear increasing stiffness curve.

2.2.3 Variable Stiffness Comparison

To compare the implementation of the above variable stiffness methods, they are implemented in a PEA configuration, in which the position of the crank-rocker driving link a is fixed. The pre-inflated PAM variable stiffness element was selected to have an initial internal pressure of 350 kPa, as its stiffness profile best fits the gait stiffness.

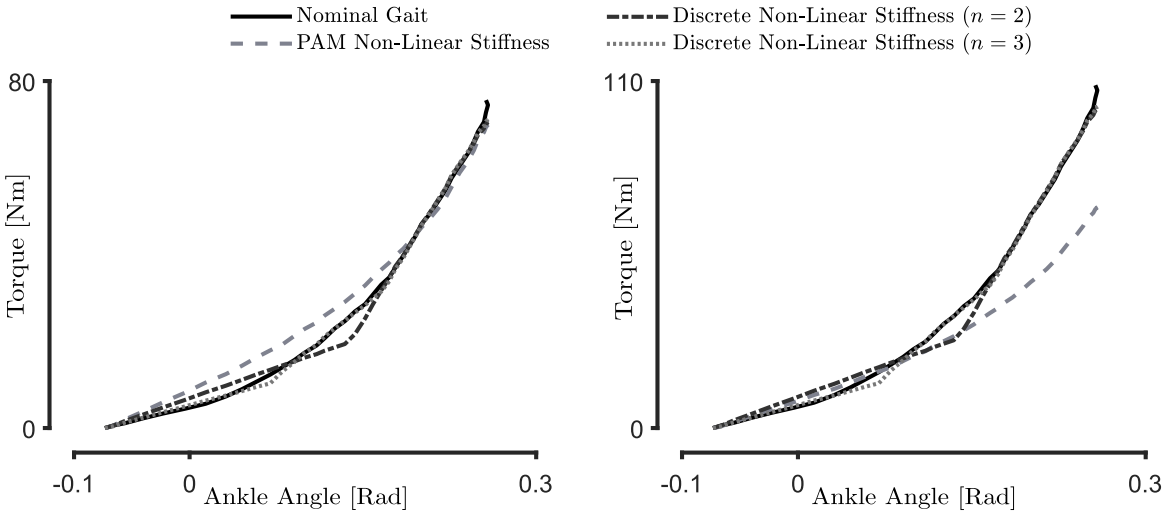

Figure 2.7: Comparison between the pre-inflated PAM stiffness element and the discrete nonlinear stiffness element with one ($n = 2$) and two ($n = 3$) discrete stiffness changes. Each configuration is compared to the stiffness of the ankle joint for 5% - 45% of the gait cycle, known as the loading phase. Each plot shows the regenerating braking capability of each actuator in in the loading phase of the gait cycle, where the left plot is the torque based on 56 kg user and the right an 80 kg user.

The discrete nonlinear stiffness method is also explored with one ($n = 2$) and two ($n = 3$) discrete stiffness changes. Fig. 2.7 displays the result when the pre-inflated PAM and the discrete nonlinear stiffness design are used in a PEA configuration. The ankle joint rotation is simulated and the torque applied by the stiffness element via lever arm c is calculated and compared to the nominal ankle torque for 80 kg user, a value between the average Canadian male and female mass, and 70% of the average mass (56 kg) as users may have some push-off capability [75]. The results show that the pre-inflated PAM has a similar stiffness profile to the gait cycle in the loading phase. However, the proposed discrete nonlinear actuator can achieve a similar stiffness profile with one discrete stiffness change. Both designs could be capable of adequate regenerative braking, resulting in a reduced peak input power to the system. Nevertheless, the pre-inflated PAM as a stiffness element is not practical compared to the simplicity of the discrete nonlinear method. The utilized PAM is long, with an initial length of 235 mm and lacks versatility in lever arm lengths and stiffness profiles.

The discrete nonlinear stiffness method is versatile and straightforward, approximating an ever-increasing stiffness profile with a few discrete stiffness changes. Therefore, to minimize the size, complexity and mass of an AAFO actuator, the discrete nonlinear stiffness element proposed will be optimized with the crank-rocker mechanism.

2.3 Actuator Optimization

The proposed discrete nonlinear stiffness method is more versatile than the pre-inflated PAM in a PEA configuration. Therefore, to find the best design for the crank-rocker and discrete nonlinear SEA combination, with one discrete stiffness change ($n = 2$), optimization of the various link lengths, offsets, and spring stiffnesses is performed. Non-dominated Sorting Genetic Algorithm II (NSGA-II) [76] is employed to minimize the peak power and total length of two actuator configurations:

1. Discrete nonlinear stiffness crank-rocker ($n = 2$)

2. Linear stiffness crank-rocker (as in $n = 1$)

The decision variables are $[P_x, P_y, a, b_0, c, k_1, k_2, \delta_{Off_2}, \theta_{adj}]$, where θ_{adj} is an angular offset between θ_a and the ankle joint. The objective functions of the multi-objective optimization are to minimize the mechanical input power to the device while minimizing the overall length of the employed linkage configuration, defined as:

$$\text{Minimize: } \begin{cases} P_{max} = \max(|P|) \\ L = a + b + c + d \end{cases} \quad (2.9)$$

to target the reduction in mass of the actuator while providing the necessary power to the ankle joint. Minimizing the motor's peak power results in a smaller (and thus lighter) motor and gearbox combination. Minimization of the link length limits the size and mass of the linkages.

The optimization of the crank-rocker mechanism is subject to the constraints of trajectory tracking compliance of a nominal gait, as link a limits the displacement range of

b. Therefore, if the desired response of θ_a is not achieved, then the values of the minimization objective functions are divided by the penalty scalar $P_s \in [0, 1]$, determined as:

$$P_s = \begin{cases} P_s = 1, & \text{if } valid = 1 \\ P_s = valid \cdot \beta, & \text{otherwise} \end{cases} \tag{2.23}$$

with:

$$valid = \frac{|\theta_a| - |\theta_{a_{invalid}}|}{|\theta_a|} \tag{2.24}$$

where $\beta \in [0, 1]$. To conduct the optimization, the selected actuator configuration population is randomly generated within a set decision variable range. Any population member that results in $P_s < 1$ is discarded. Each iteration of NSGA-II is conducted by solving for link c position (θ_c) and torque (τ_c) for a complete gait cycle. The objective function L is calculated, and P_{max} is determined from Eq. (2.9).

Optimization can be conducted in three steps to determine a feasible design with available market springs. The first step is to fix the length of b_0 to allow sufficient room for the spring assembly. The simulation is conducted, and the optimized value of k_1 for power reduction is reviewed; a spring with the closest stiffness and displacement larger than that required of k_1 is selected. Step two re-conducts the simulation with a fixed value of k_1 identified in the previous step, in which the same selection process is used for k_2. The final step has fixed values for k_1, k_2, and b_0, in which the final link lengths and offsets are acquired. A complete simulation of the designs is recorded, including the displacement and force within link b, to study each design's regenerative braking and power application instances.

2.4 Optimization Results & Discussion

The power the actuator applies to the ankle joint is a combination of spring and motor power. As seen in [36], the total ankle power is:

$$P_{Total} = \underbrace{\tau_a \dot{\theta}_a}_{\text{ankle}} = \underbrace{F_b \dot{b}}_{\text{spring}} + \underbrace{\tau_c \dot{\theta}_c}_{\text{motor}} \tag{2.25}$$

The optimization results can be seen in Fig. 2.8a. The discrete nonlinear design results in a lower peak motor power for a longer duration than the equivalent linear design (see Fig. 2.8b). The power reduction stems from the discrete nonlinear design's early energy storage and late energy dispersion. The energy stored in the springs combines the user applied (regenerative braking principle) and motor applied energy. The linear and discrete nonlinear crank-rocker mechanisms see a 62.4% and 77.2% peak power reduction, compared to the peak biological ankle joint power, respectively. The peak power reduction stems from the reduced velocity of the motor (see Fig. 2.8b) during instances of high torque and power within the gait cycle. The energy consumption for the linear and discrete nonlinear cracker-rocker is 23.6 J and 19.3 J, respectively. Repeating the electrical simulation presented in section 2.1.3 with the linear and discrete nonlinear crank-rocker shows that the linear crank-rocker mechanism has a peak power increase of 2.9% compared to the peak biological ankle power, where the discrete nonlinear method sees a 21.1% decrease, as shown in Fig. 2.9. The results prove the effectiveness of design, reducing the input power by an additional 2.8% compared to the best result presented in the literature [70].

2.5 AAFO Fabrication

To validate the proposed discrete nonlinear crank-rocker, an AAFO prototype was designed and constructed, shown in Fig. 2.10(a-c). The structure is manufactured from aluminum, nylon, and steel of stock thicknesses (see Fig. 2.10d). Two aluminum rails make up the main structure of the foot-bed, encompassing the crank for the actuator and bushings to facilitate ankle rotation, shown as green in Fig. 2.10a. Nylon pads are placed under the toe and heel of the foot and mounted to the main rails with an aluminum bracket, allowing minor flexion in the foot-bed during locomotion. The pad placed under the heel is adjustable in two directions using square slots in the main rails and aluminum brackets. The nylon pad under the toe is adjustable in one direction and includes a rotational joint to allow flexion of the toes during locomotion. The AAFO shank design focuses on mounting the DC motor and wired connections

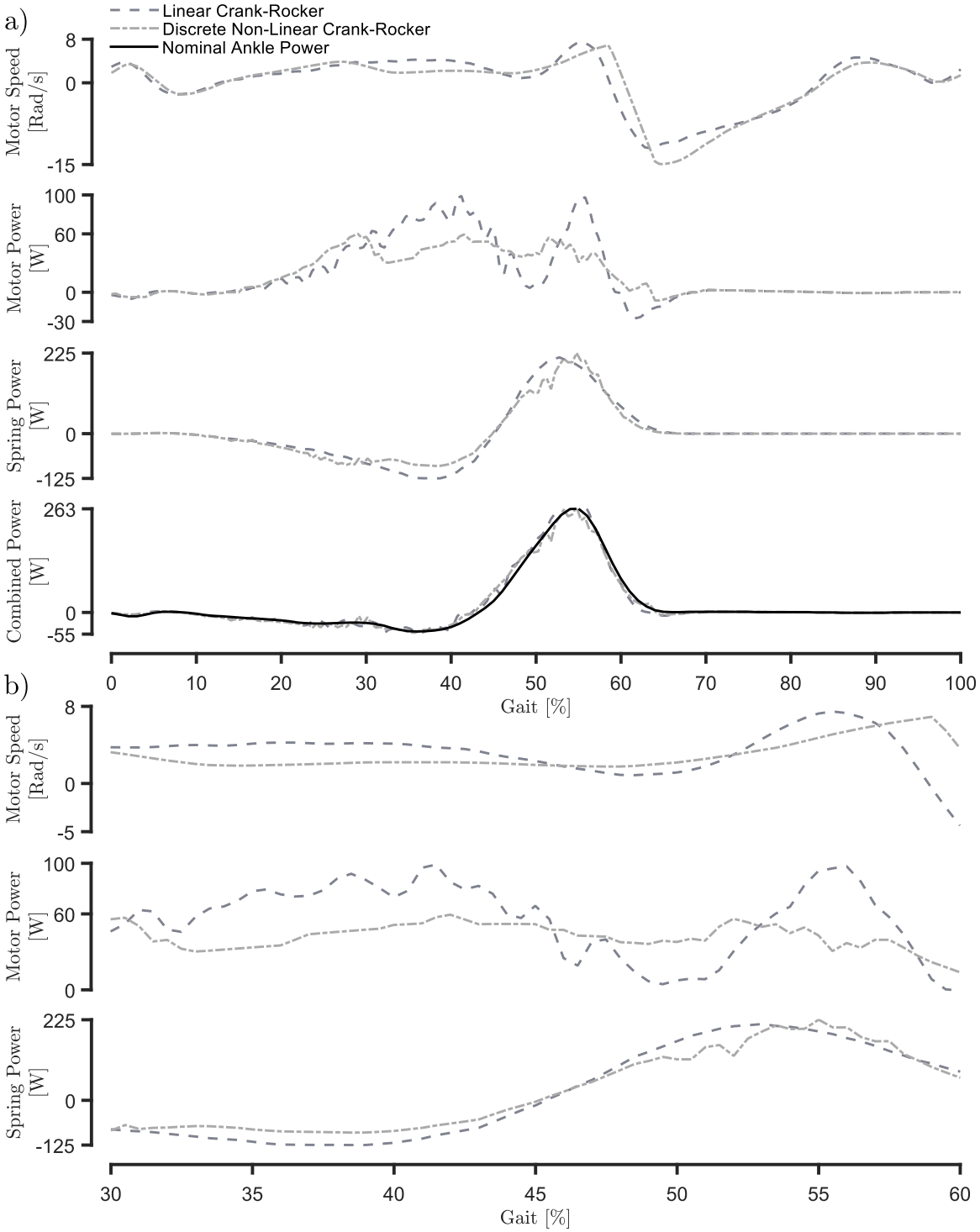

Figure 2.8: a) Motor and spring power, matching the required nominal power for a gait cycle. b) A sectioned view of a) (30% - 60%) showing the decrease in power of the discrete nonlinear design is attributed to the lower motor velocity at high torque instances.

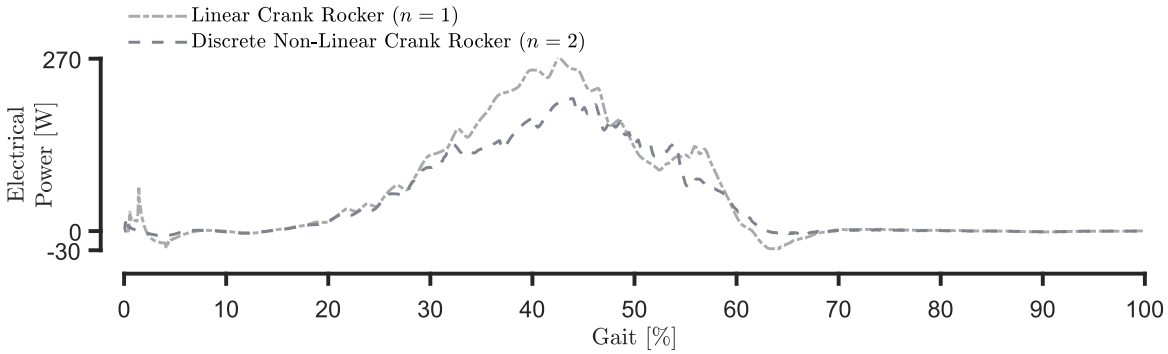

Figure 2.9: Simulated electrical power to actuate an AAFO using the crank-rocker mechanism encompassing linear and discrete nonlinear stiffness.

Table 2.2: Optimized Crank-Rocker Design: Full assistive torque for a 56 kg user.

Parameter	Value	Parameter	Value
P_x	117.83 mm	P_y	173.78 mm
a	51.86 mm	b	200 mm
c	13.49 mm	θ_{adj}	-0.38 rad
k_1	42.80 N/mm	k_2	51 N/mm
F_{Limit}	739.49 N	δ_{Off}	17.28 mm

while encompassing the calf muscle. Straps are installed on the shank and foot-bed, as depicted in Fig. 2.10e, securing the AAFO to the user.

The discrete nonlinear SEA is employed to provide assistive/resistive torque to the AAFO. The actuator was optimized using the procedure presented in section. 2.4, yielding the values listed in Table 2.2. The motor's output power, torque, and angular velocity are presented in Fig. 2.11, presenting a 76% power reduction compared to the nominal gait power. The crank-rocker mechanism is employed in Fig. 2.10b, with the discrete nonlinear link presented in Fig. 2.10c. The design places the discrete spring (k_2) within the inner diameter of spring k_1, creating a compact linkage. The actuator materials are steel for the tensile springs and connecting rods, aluminum for the top and bottom plates, and a PLA enclosure to aligns the springs. The bounding box dimensions of the discrete nonlinear system are 103x45x94 mm with a mass of 460 g. The fully assembled AAFO mass is 2.85 kg, most of the mass stems from the aluminum structure designed for user variations.

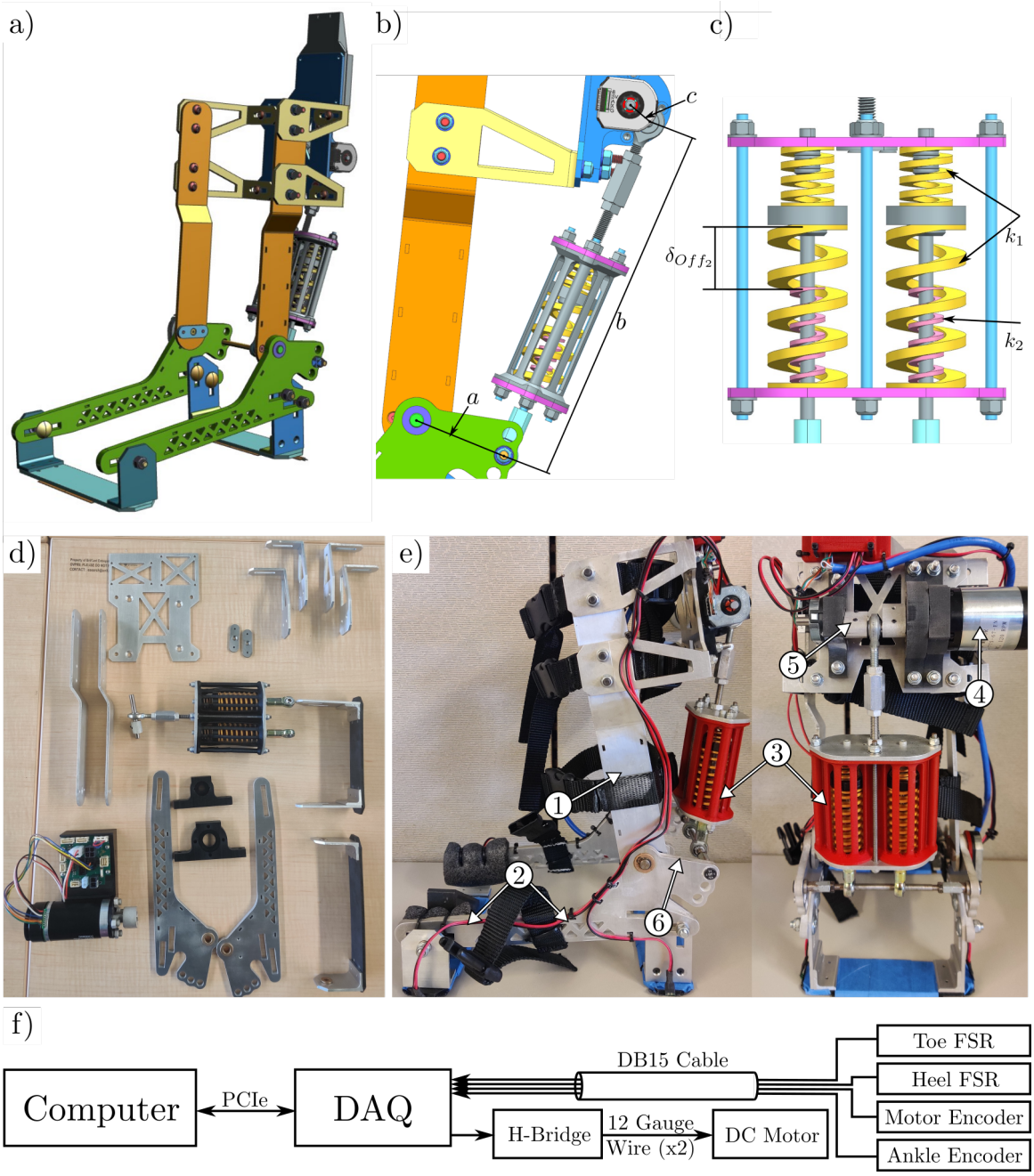

Figure 2.10: a) Computer-aided-design (CAD) model of the AAFO prototype. b) Application of the crank-rocker configuration within the CAD model. c) Discrete nonlinear linkage design, in which k_2 is placed within k_1. d) Manufactured parts for AAFO construction, including the driving motor. e) The constructed AAFO prototype. ① Shank, to be attached to the users leg, ② is the foot-bed to house the users foot. ③ is the constructed discrete nonlinear SEA. ④, ⑤, and ⑥ are the DC motor and gearbox, crank, and rocker linkages, respectively. f) Electrical system flow chart. The computer reads the FSR states and encoder angles from the DAQ and provides the required motor speed to the DAQ.

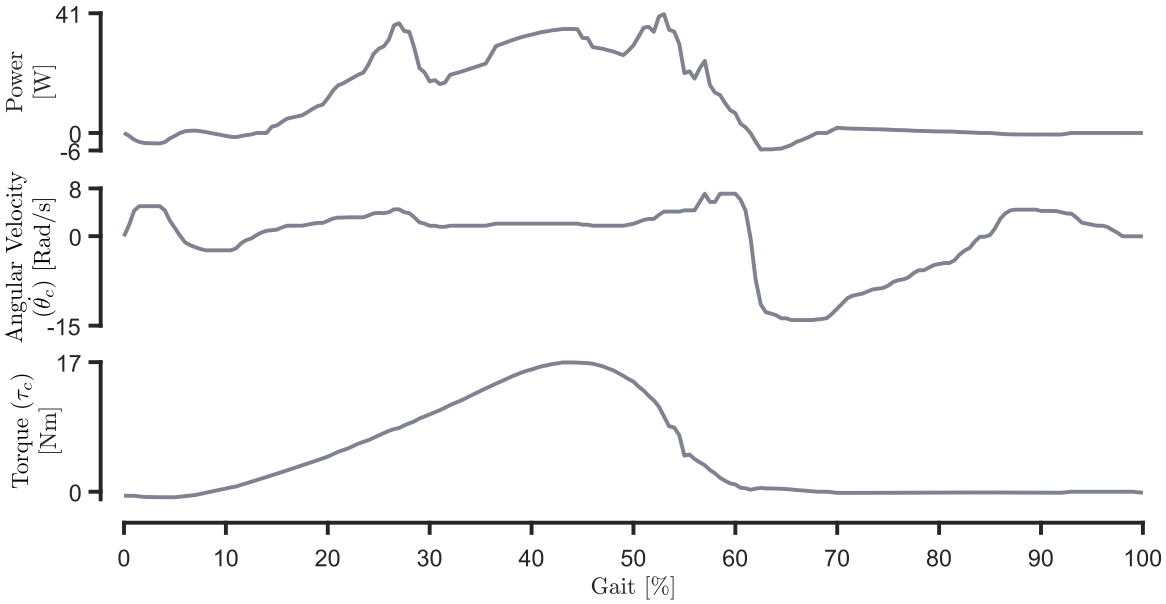

Figure 2.11: Motor output for the actuator optimized to applied full assistive power for a 56 kg user. The design results outputs a peak power of 174 W at the ankle joint with a peak input power of 41 W.

Ankle and motor position must be known for the proposed actuator to apply an accurate torque to the ankle joint. Therefore, two quadrature encoders (CUI AMT102 & AMT103) with a resolution of 0.088 degrees are incorporated to measure the ankle and motor angle. Two sets of force-sensitive resistors (FSR) are mounted under the nylon heel and toe pads. A voltage divider circuit is developed to measure the change in voltage upon force application. The FSRs are implemented to synchronize the known nominal angular trajectory in Fig. 1.2 with the user's current gait. To drive the proposed actuator, a 24V geared DC motor (ES-Motor 150W with a $67:1$ planetary gearbox) is controlled by an H-bridge (Devantech MD04), with the armature current measured by a bi-directional current sensor (Allegro ACS758-DS).

The sensors and driving electronics communicate with a Windows computer (Intel Core2 Quad 2.50 GHz, 6 Gb DDR2) through a data-acquisition-card (DAQ) (Humusoft MF634) (see Fig. 2.10f). A control system is programmed in C++, using the Windows application-programming-interface to set the system to the highest priority, giving the controller immediate access to the CPU. The program is structured into three threads: PD motor position control (20 kHz), data logging (100 Hz), and the

main control loop (100 Hz), which determines the required torque at the ankle joint and calculates the required motor position. Internal functions within the control system measure the time elapsed between gait phases, measured by the heel or toe FSR change in state. The desired trajectory is then scaled to match the new gait speed.

The developed and constructed AAFO prototype enables experimental testing of the proposed discrete nonlinear SEA and control methods in the following Chapters.

2.6 Experimental Validation

In order to verify the actuator model and above formulations, a static loading and human walking trial are carried out. The output ankle and motor torque of the actuator are determined by the measured rotation of links a and c, by analyzing the change in actuator length:

$$\Delta b = \sqrt{(P_{Ay} - P_{Cy})^2 + (P_{Ax} - P_{Cx})^2} - b_0 \tag{2.26}$$

where:

$$P_{Cx} = P_x + c\cos\theta_c, \quad P_{Cy} = P_y - c\sin\theta_c$$

Resulting in an axial force in link b of:

$$F_b = \begin{cases} \Delta b\,(k_1)\,, & \Delta b < 0 \\ \Delta b\,(k_1)\,, & \Delta b < \delta_{Off} \\ \delta_{Off}k_1 + (\Delta b - \delta_{Off})(k_1 + k_2), & \text{otherwise} \end{cases} \tag{2.27}$$

in which the resulting torque at the motor (τ_c) is presented in Eq. (2.17) and ankle joint torque (τ_a) can be expressed as:

$$\tau_a = aF_b \sin(\theta_a - \theta_b); \tag{2.28}$$

where θ_b is determined as:

$$\theta_b = \arctan\left(\frac{P_{Cx} - P_{Ax}}{P_{Cy} - P_{Ay}}\right), \tag{2.29}$$

Both the torque at the ankle and motor joint can be verified with the motor and ankle position and current measurements.

2.6.1 Static Loading Test

A static loading test is conducted with the AAFO mounted on a rigid test stand. The end of the AAFO foot-bed is placed on a dynamometer (KISTLER Type 9255C) depicted in Fig. 2.12a to measure the component reaction force that the AAFO applies to the ground. The length of the lever arm is measured to be 188.5 mm to determine the applied torque by the AAFO. The test required the AAFO to apply torque to the ankle joint in response to a step input. The corresponding modelled torque and measured torque for the experiments are shown in Fig. 2.13a. The results prove that the model is accurate. Any discrepancies in the measurements can be attributed to the stiffness accuracy of the manufactured springs, assembly of the components, and encoder calibration.

2.6.2 Human Walking Trial

A human walking trial is also conducted on a clinical treadmill by a user with no gait impairment, see Fig. 2.12(b-c). The model calculated assistive ankle torques of up to 53 Nm throughout the test, resulting in the discrete nonlinear actuator exceeding the δ_{Off_2} displacement multiple times. To validate the motor torque model, the torque constant of the motor is inferred from the measured motor current and modelled motor torque, as the torque of a motor is directly co-related to the armature current ($\tau_m = k_\tau i_a$). Fig. 2.13b shows the result at high modelled motor torque and current instances. The signal noise can be linked to the response of the motor position controller. These tests show that the presented model is accurate.

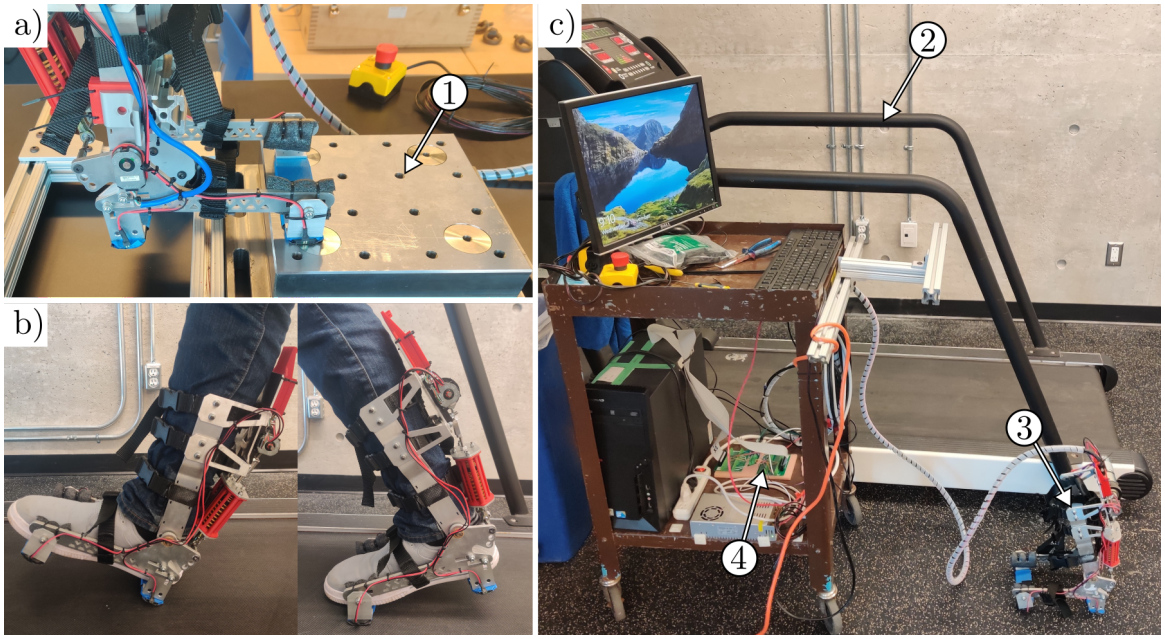

Figure 2.12: a) Static actuator test setup using the AAFO to apply a torque, which is measured by the dynamometer ①. b) Demonstration of the AAFO during the human walking trial. c) Experimental walking trial setup, containing a clinical treadmill ②, the AAFO ③, and respective processor and driving electronics ④.

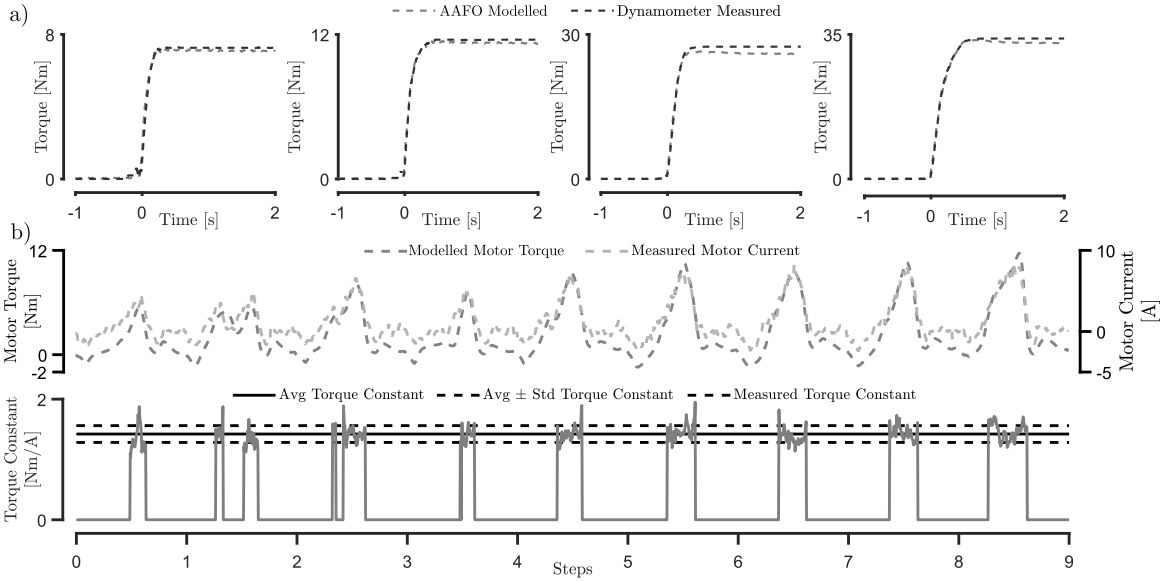

Figure 2.13: a) AAFO static load dynamometer testing at various step inputs. The results compare the modelled ankle torque based on the actuator displacement Eqs. (2.26)-(2.28) to a measured torque on a dynamometer. b) Human walking trial modelled motor torque, current, and inferred torque constant results.

2.7 Concluding Remarks

This Chapter explored the optimal actuator topology and stiffness element for AAFOs. The goal of the actuator design is to minimize the mass and size of the device while providing the required power at the ankle joint. The crank-rocker mechanism can reduce the peak input power to the device by reducing the required holding torque of the motor at instances of high ankle joint torque. When combined with the discrete nonlinear stiffness method with one discrete stiffness change ($n = 2$), the actuator can reduce the peak mechanical and electrical input power by 72.2% and 21.1%, with respect to the peak biological ankle joint power.

The presented discrete nonlinear actuator is capable of accurately approximating an increasing nonlinear stiffness. The stiffness in the loading phase is ever increasing for the ankle joint, resulting in a high peak power reduction. However, the design is insufficient in the presence of a decreasing stiffness required for regenerative braking. Instead, discrete springs must be engaged in series, where k_2 would be preloaded with force equal to $k_1\delta_{Off_2}$. To obtain the best performance from the proposed actuator, a control system must be developed to estimate the push-off torque required by the AAFO while tracking the angular trajectory.

Chapter 3

Adaptive Extended State Observer for an Active Ankle-Foot Orthosis

Reprinted, with permission, from B. DeBoer, A. Hosseini, and C. Rossa,

Adaptive Extended State Observer for an Active Ankle-Foot Orthosis,

2021 IEEE International Conference on Systems, Man, and Cybernetics (SMC), p.1105-1110, Melbourne, Australia, 2021

TRAJECTORY tracking is a popular method of AAFO control, in which the goal is to track the angular trajectory of an unimpaired gait, shown in Fig. 1.2. The PID controller is a commonly introduced tool to track the desired position for a simple control system, where the AAFO can be modelled as a simple rotary system. However, the AAFO is subject to a large cyclical disturbance originating from the push-off force required for locomotion. If the user cannot provide the torque required in push-off, a subsequent disturbance torque is presented to the AAFO, known as an exogenous disturbance. When the user has minor plantarflexion capability, the AAFO must compensate for the nominal push-off torque (1.32 Nm/kg of user mass, see Fig. 1.2). In the case of a PID controller, high control gains and significant positional error would be required to account for the disturbance. A high gain controller is undesirable as minor deviations will result in a significant reaction torque from the AAFO. Previous works have modelled and rejected the exogenous disturbance to the system. However, the model is cyclic and rejects the same torque regardless of the user's step-by-step need. The second origin of disturbance is also present in AAFOs. Guerrero *et al.* [62], stated that the exact rotational inertia of the user's foot could not be measured directly, presenting an endogenous disturbance to the system. This disturbance results from the unmeasurable and time-invariant model parameters of the combined AAFO device and ankle joint. Adaptive control schemes have been introduced, reducing the dynamics modelling error by estimating the plant parameters. However, the presented methods conduct parameters estimation based on the trajectory tracking error, applying additional assistance to the user to minimize the tracking error.

This chapter presents an adaptive ESO for AAFOs. The concept employs an ADRC to identify and reject the exogenous and endogenous disturbances for each step. The ARDC does not require the main trajectory tracking controller to encompass high gains to reject the presented disturbance. Parameter estimation is also isolated from the trajectory tracking error. The nominal ankle torque (exogenous disturbance shown in Fig. 1.2) is subtracted from the rejected disturbance to reveal the endogenous disturbance. An analysis is conducted to identify the root of the endogenous disturbance,

taking the current gait percentile and angular velocity of the AAFO into consideration. Consequently, the inertial and damping parameters of the plant and ankle joint combination can be identified, minimizing the presence of the endogenous disturbance.

The chapter is structured as follows: Section 3.1 presents the dynamic model of the AAFO, with the ESO described in section 3.2. Section 3.3 presents adaptive laws to minimize the error in dynamics modelling, proven by simulations in section 3.4. Results of the proposed adaptive ESO are discussed in section 3.5, and section 3.6 states the concluding remarks.

3.1 Ankle-Foot Orthosis Model

An AAFO can be expressed as a rotary system with the dynamics:

$$J_P\ddot{\theta}_a + B_P\dot{\theta}_a + K_P\theta_a = u_d + u_a \tag{3.1}$$

where J_P, B_P, and K_P are the rotational inertia, viscous damping coefficient, and stiffness coefficient of the AAFO device and ankle joint combination. Control signals u_a and u_d are the torque applied by the actuator and disturbance torque, respectively, and θ_a is the ankle joint angle. Static friction in the model is assumed to be negligible. The model presented in state-space form is:

$$\begin{bmatrix}\dot{\theta}_1\\ \dot{\theta}_2\end{bmatrix} = \underbrace{\begin{bmatrix}0 & 1\\ -\frac{K_P}{J_P} & -\frac{B_P}{J_P}\end{bmatrix}}_{A}\underbrace{\begin{bmatrix}\theta_1\\ \theta_2\end{bmatrix}}_{\vec{\theta}} + \underbrace{\begin{bmatrix}0\\ \frac{1}{J_P}\end{bmatrix}}_{B}(u_d + u_a)$$

$$\theta_a = \underbrace{\begin{bmatrix}1 & 0\end{bmatrix}}_{C}\begin{bmatrix}\theta_1\\ \theta_2\end{bmatrix}$$

where $\theta_1 = \theta_a$, $\theta_2 = \dot{\theta}_a$. The main goal of a trajectory tracking controller is to minimize the error between the ankle position and the desired trajectory, which can be obtained through the nominal gait cycle shown in Fig. 1.2. The nominal torque ($u_{d_{Nom}}$) required at the ankle joint can be treated as the exogenous disturbance ($u_d = u_{d_{Nom}}$)

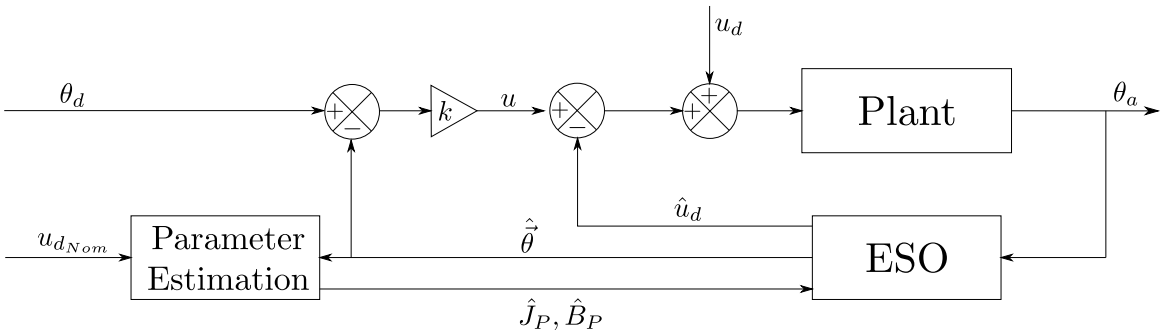

Figure 3.1: Control system topology. θ_d is the desired trajectory, θ_a is the plant output, u_d is the disturbance, $\hat{u_d}$ is the estimated disturbance, and k is the state feedback gain to eliminate tracking error.

to the AAFO. If the user has partial to full muscle activation, the disturbance to the system is scaled down. The torque disturbance must be identified and compensated to accurately track the angular trajectory.

3.2 Disturbance Rejection for Trajectory Tracking

The proposed AAFO control system is presented in Fig. 3.1. It is comprised of the AAFO device (plant), an ESO, and a state feedback controller. In this thesis, the stiffness coefficient (K_P) of the AAFO and ankle joint combination is assumed to be negligible based on limited AAFO designs that implemented constant stiffness at the ankle joint (see Fig. 1.4). The ESO rejects both exogenous and endogenous disturbances. Based on the identified torque disturbance and the nominal torque at the ankle joint, the plant parameters J_P and B_P are estimated to minimize the endogenous disturbance.

3.2.1 State Feedback Controller

State feedback control is applied to track the desired trajectory of the AAFO, using manual pole placement to select the state feedback gains. While state feedback is efficient at minimizing tracking error, the output deteriorates in the presence of significant disturbances. Therefore, implementing the ESO with state feedback will improve the AAFO tracking capability.

3.2.2 Extended State Observer

A linear state observer estimates the current plant states based on the difference between the modelled and measured plant output and is defined as [77].

$$\dot{\hat{\vec{\theta}}} = A\hat{\vec{\theta}} + Bu + LC(\theta_a - \hat{\theta_a}) \tag{3.2}$$

where A, B, C, L and $\hat{\theta}_a$ are the plant state, input, and output matrixes, observer gain and observer ankle position, respectively. When a disturbance is applied to the system, the observer states do not match the plant states. Therefore, the ESO is designed to approximate the disturbances of the system using an additional extended state. By adding an extended state to the system, i.e., $\dot{\theta}_3 = \dddot{\theta}_a$ with $\theta_3 = \ddot{\theta}_a$, the value of the state is used with the inertial plant component as the disturbance rejection control effort. The ESO is expressed as

$$\begin{cases} \dot{\hat{\theta}}_1 = \hat{\theta}_2 + \epsilon_1 fal\left(e, \phi_1, \delta_1\right) \\ \dot{\hat{\theta}}_2 = \hat{\theta}_3 + \frac{u - \hat{u}_d - \hat{B_P}\hat{\theta}_2}{\hat{J_P}} + \epsilon_2 fal\left(e, \phi_2, \delta_1\right) \\ \dot{\hat{\theta}}_3 = \epsilon_3 fal\left(e, \phi_3, \delta_3\right) \end{cases} \tag{3.3}$$

where $fal\left(e, \phi_i, \delta_i\right)$ is a nonlinear gain function defined by [61] for $i = 1, \ldots, n$, and n is the number of states. The scalar values of ϵ_i are selected by poles placement or optimization, such as work in [78]. The nonlinear gain function is evaluated as [61]:

$$fal\left(\tilde{\theta}_a, \phi_i, \delta_i\right) = \begin{cases} |\tilde{\theta}_a|^{\phi_i} \text{sign}(\tilde{\theta}_a) & |\tilde{\theta}_a| > \delta_i \\ \frac{\tilde{\theta}_a}{\delta_i^{1-\phi_i}} & |\tilde{\theta}_a| \leq \delta_i \end{cases} \tag{3.4}$$

where $\delta_i > 0$, $\phi_i > 0$, and $\tilde{\theta}_a = \theta_a - \hat{\theta}_a$. For the torque-controlled system, the estimated disturbance value of $\hat{u_d} = \hat{\theta}_3 \hat{J}_P$ is added to the state-feedback control signal (u) to compensate for the disturbances (u_d), as shown in Fig. 3.2. The observability matrix is constructed to ensure the AAFO can be observed and is determined as:

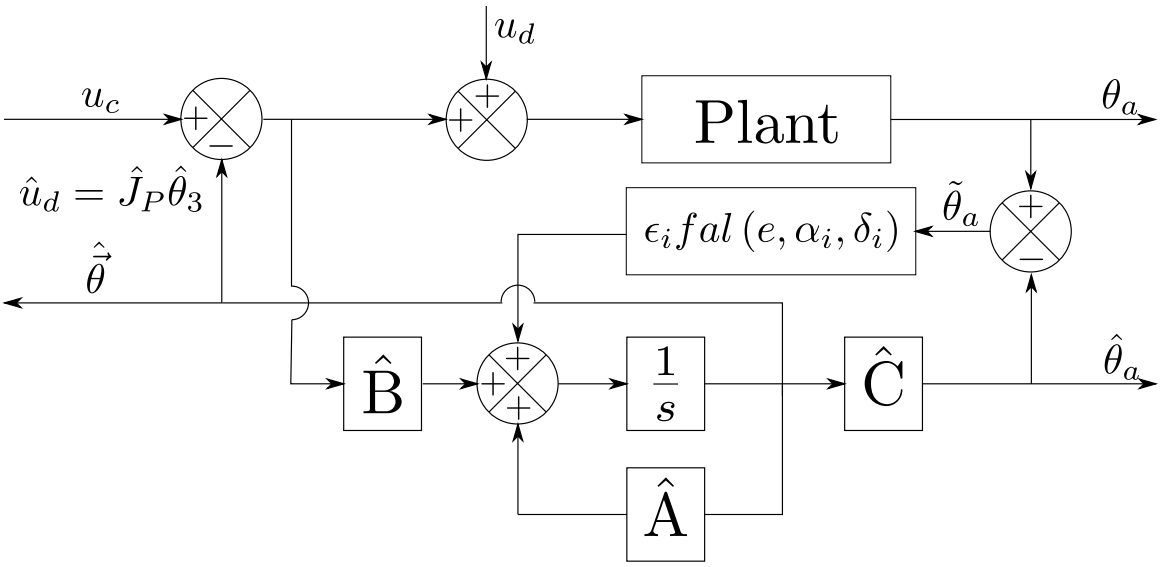

Figure 3.2: Nonlinear ESO topology in which the disturbance rejection torque is the estimated extended stated (θ_3) times the estimated inertia ($\hat{J}_P$).

$$Obs = \begin{bmatrix} C & CA & CA^2 \end{bmatrix}^T$$

where:

$$A = \begin{bmatrix} 0 & 1 & 0 \\ 0 & 0 & 1 \\ 0 & 0 & 0 \end{bmatrix}, C = \begin{bmatrix} 1 & 0 & 0 \end{bmatrix}$$

leading to:

$$Obs = \begin{bmatrix} 1 & 0 & 0 \\ 0 & 1 & 0 \\ 0 & 0 & 1 \end{bmatrix}$$

The observability matrix is full rank; therefore, the plant is observable, and an ESO can be used for disturbance rejection.

3.3 Parameter Estimation

This section introduces a novel method to estimate the inertial J_P and frictional B_P parameters of the AAFO and ankle joint, based on the difference between the observed disturbance and nominal ankle torque disturbance.

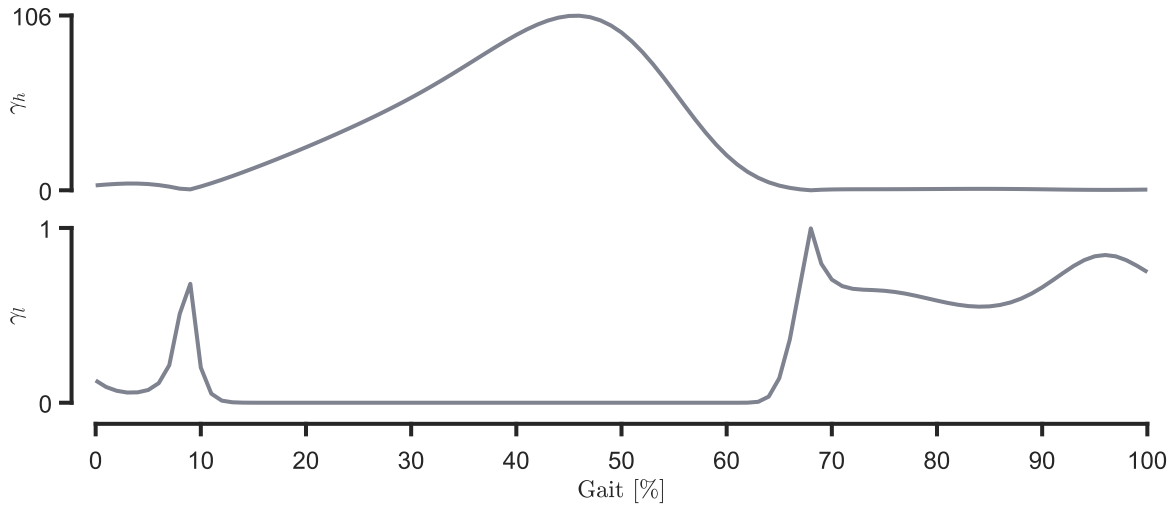

Figure 3.3: Gain value with respect to the gait cycle for instances of estimation at high (γ_h) and low (γ_l) disturbance instances, where $\zeta = 2$ and $\kappa = 1$ in Eqs. (3.6) and (3.7) based on a 80 kg user.

To determine J_P and B_P using online estimation, the known cyclic disturbance trajectory can be referenced, see Fig. 1.2. The parameter estimation laws identify J_P and B_P by minimizing the endogenous disturbance, modelled as:

$$\tau_{d-model} = \tilde{J}_P \ddot{\theta}_a + \tilde{B}_P \dot{\theta}_a \tag{3.5}$$

where $\tilde{J}_P$ and $\tilde{B}_P$ represent the error between estimated ($\hat{J}_P, \hat{B}_P$) and real model parameters. The endogenous torque is extracted by comparing the observed disturbance to the scaled nominal disturbance, using the scaling factor κ. Adaption is designed to occur during optimal parameter estimation portions of the gait cycle. Instances with significant disturbances are insufficient in determining the plant parameters, but lower disturbance levels can be used to estimate parameters. Therefore, two gain functions are developed for parameters estimation, where the high gain

$$\gamma_h = ||\kappa u_{d_{Nom}}|| \tag{3.6}$$

is used for estimating parameters that have a more significant effect on the distur-

bance when the magnitude of the disturbance is large, and the low gain

$$\gamma_l = \frac{1}{\zeta^{||\kappa u_{d_{Nom}}||}} \tag{3.7}$$

is used for estimating parameters at low disturbances. In Eqs. (3.6) and (3.7), $\zeta > 1$ is a scalar that penalizes larger instances of the nominal disturbance, see Fig. 3.3. Since parameter estimation is based on the difference between the nominal torque u_d and estimated torque $\hat{u_d}$, the rejected torque from the ESO must be scaled so that the magnitude matches that of the nominal torque. The scaling factor κ is determined iteratively based on the difference between the peak disturbance instances, using estimation gain γ_h, as:

$$\dot{\kappa} = a_\kappa \gamma_h \underbrace{\left(u_{d_{Nom}} + \kappa \cdot \hat{\theta}_3 \hat{J}_P\right)}_{\text{disturbance error}} \kappa \tag{3.8}$$

where $a_\kappa > 0$ is a scalar gain modified to optimize convergence. Parameters J_P and B_P can now be determined using the scaled nominal disturbance torque, where the inertial parameter J_P can be estimated by:

$$\dot{\hat{J}}_P = -a_J \gamma_l \underbrace{\left(u_{d_{Nom}} + \kappa \cdot \hat{\theta}_3 \hat{J}_P\right)}_{\text{disturbance error}} \cdot \hat{J}_P \tag{3.9}$$

where $a_J > 0$ is the inertial scaling factor, and damping parameter B_P is determined by:

$$\dot{\hat{B}}_P = -a_B \gamma_l \hat{\theta}_2 \underbrace{\left(u_{d_{Nom}} + \kappa \cdot \hat{\theta}_3 \hat{J}_P\right)}_{\text{disturbance error}} \hat{B}_P \tag{3.10}$$

where $a_B > 0$ is the scalar gain. Since the disturbance due to $\tilde{B_P}$ is a function of velocity, θ_2 is included in the estimation. It is noted that the disturbance torque due to the error $\tilde{J_P}$ depends on $\hat{\theta_3}$, however, the use of the observed value, which is the extended state, would not lead to convergence as the disturbance error is based on the same state.

Since the estimation law of J_P and B_P depends on the same disturbance error, their convergence is dependent on one another. Regardless of the scalar gains a_κ, a_J, a_B, the proposed method can converge to the true values of J_P and B_P based on the endogenous torque disturbance relationship presented in Eq. (3.5).

3.4 Adaptive Extended State Observer Simulation

Simulations are conducted in MATLAB using embedded differential solvers to verify the control system and novel estimation law presented in section 3.2. Gait data for the ankle joint is retrieved from the study presented in [9], consisting of the reference ankle trajectory and nominal ankle torque (see Fig. 1.2). The control system simulations first analyze the advantages of the ESO compared to direct state feedback control, followed by implementing the plant parameter estimation. The simulations are conducted based on an 80 kg user with a nominal gait time of 1.1s, as presented in [9].

3.4.1 Extended State Observer Simulation

The first simulation is conducted using state feedback and state feedback in combination with the ESO to identify the advantages of disturbance rejection. The desired torque output of the actuator u_a is a function of state feedback and the ESO rejected disturbance. The state feedback gain was determined by placing poles at $[-100, -100]$ for $[\theta_1, \theta_2]$, resulting in the feedback gain:

$$k = \begin{bmatrix} 10000 & 200 \end{bmatrix} \tag{3.11}$$

where the control effort u is determined by:

$$u = k \begin{bmatrix} \theta_d - \theta_1 \\ -\theta_2 \end{bmatrix} \tag{3.12}$$

In the above equation, θ_1 and θ_2 are the current states of the AAFO. It is assumed that full state measurement of the ankle joint is available for stand-alone state feedback control. Combining the state feedback controller with an ESO, the controller gains are modified to:

$$k = \begin{bmatrix} 10000 & 200 & 0 \end{bmatrix} \tag{3.13}$$

and thus the controller output is determined by

$$u = k \begin{bmatrix} \theta_d - \hat{\theta}_1 \\ -\hat{\theta}_2 \\ -\hat{\theta}_3 \end{bmatrix}, \tag{3.14}$$

where $\hat{\theta}_1, \hat{\theta}_2, \hat{\theta}_3$ are the observed states. The torque applied by the actuator is the sum of the controller and disturbance rejection torque as

$$u_a = u - J_{P_0}\hat{\theta}_3 \tag{3.15}$$

in which $J_{P_0} = J_P$ if known, else $J_{P_0} = \hat{J}_P$ is substituted. The scalar values ϵ_1, ϵ_2, and ϵ_3 were determined by pole placement of a linear observer at $[-100, -100, -100]$ to determine the nonlinear observer gains. The respective values of ϕ_1, ϕ_2 and ϕ_3 were retrieved from [61], and the values of δ_1, δ_2, and δ_3 were determined experimentally as 0.001, by decrementing their values until a transient response is visible in the rejected disturbance. Therefore, the nonlinear observer gain is expressed as:

$$L = \begin{bmatrix} 3 \cdot 10^2 \cdot fal\left(\tilde{\theta}_a, 1.00, 0.001\right) \\ 3 \cdot 10^4 \cdot fal\left(\tilde{\theta}_a, 0.50, 0.001\right) \\ 1 \cdot 10^6 \cdot fal\left(\tilde{\theta}_a, 0.25, 0.001\right) \end{bmatrix} \tag{3.16}$$

The result of implementing the stand-alone state feedback controller and the combination of state feedback control and the ESO is shown in Fig. 3.4a. The state feedback controller can track the required angular trajectory of the system, with only a $6.10 \cdot 10^{-}4$ rad root mean squared (RMS) tracking error between the desired an-

gular trajectory and plant output, applying a control signal similar to the nominal disturbance torque. However, the RMS tracking error is reduced to $5.76 \cdot 10^{-}4$ rad while applying a higher assistive torque when combined with the ESO.

The tracking capability of the stand-alone state feedback controller is linked to the high control gains. Consequently, the controller will have a significantly stiff response to sudden deviation in angular trajectory, seen in the state feedback & ESO controller response in Fig. 3.4a, an unideal response for AAFOs. Therefore, the response in the presence of low control gains, $k = \begin{bmatrix} 100 & 20 & 0 \end{bmatrix}$ with poles at $[-10, -10]$, is explored. In response, the RMS tracking error of the state feedback controller increases significantly to $7.30 \cdot 10^{-}3$ rad compared with the combined system of only $2.10 \cdot 10^{-}3$ rad, see Fig. 3.4b.

3.4.2 Parameter Estimation

Additional simulations with a large and small initial estimate of both J_P and B_P with the static plant parameters of $J_P = 0.03$ and $B_P = 0.02$ are conducted to validate the novel parameter estimation method. The estimation scalar gains a_κ, a_J, and a_B are set to $5 \cdot 10^{-4}$, 5, and 5, respectively. A filter, first-order with a time constant of 2 seconds, was applied to the estimates of J_P and B_P to allow the system to operate with parameter values of low variance for a complete step. The results are shown in Fig. 3.5a, where the raw and filtered parameter estimations can be seen in Fig. 3.5b for two test cases. It is evident in the simulations that the system converges close to the real plant parameters, indicated by the straight dashed lines in Fig. 3.5. Another two test cases were evaluated with only 50% of the nominal disturbance applied to analyze the effects of a reduced disturbance torque on parameter convergence. The results, see Fig. 3.5c, shows the quick convergence of κ and the minimal effect of κ on converging $\hat{J_P}$ and $\hat{B_P}$ to the real plant values. Therefore, the estimation laws are efficient at determining the plant parameters of the AAFO.

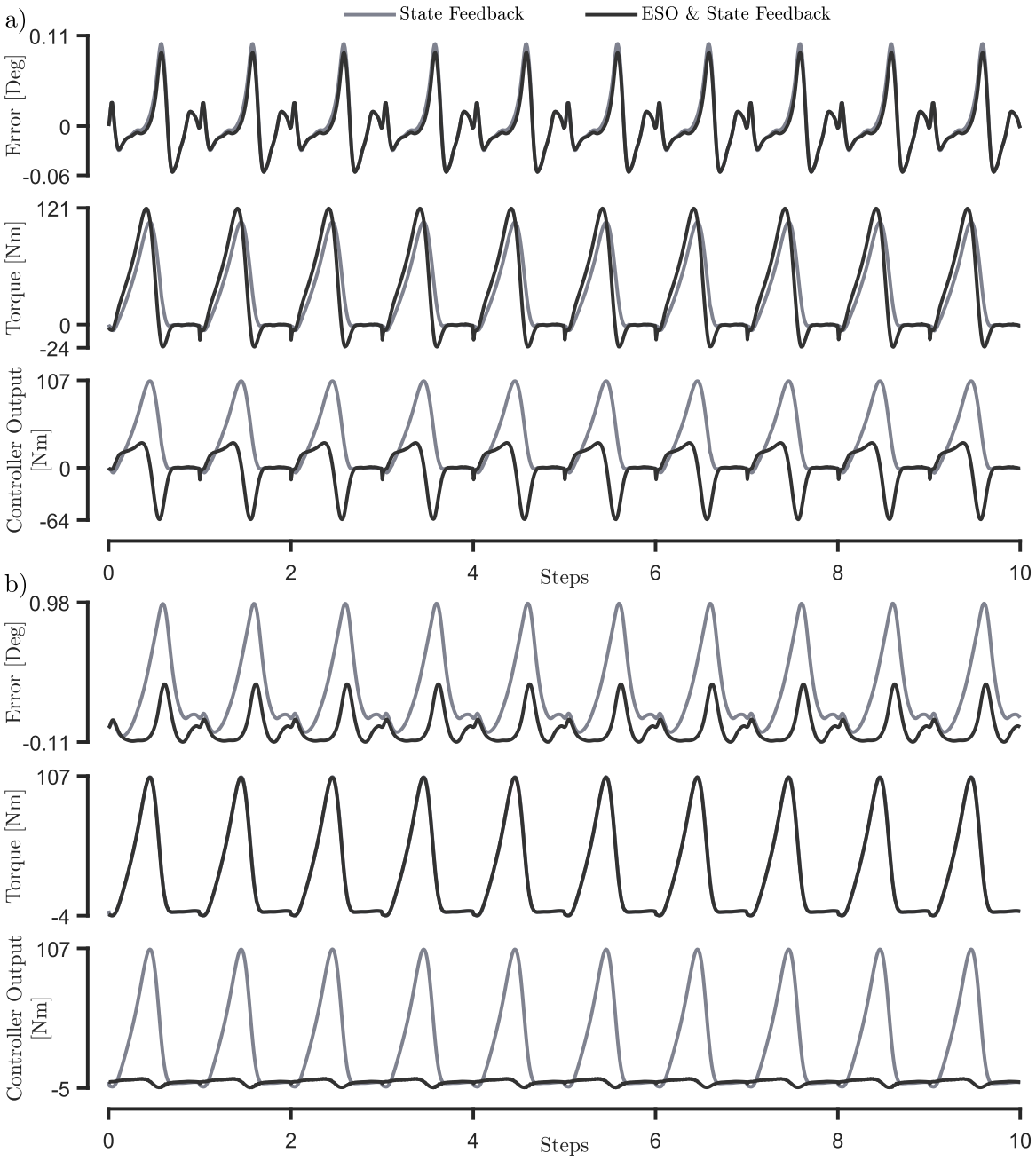

Figure 3.4: Tracking and control comparison results between state feedback and state feedback in combination with the ESO. a) High controller gains b) Low controller gains. The error corresponds to the difference between the desired angular trajectory and AAFO angular position.

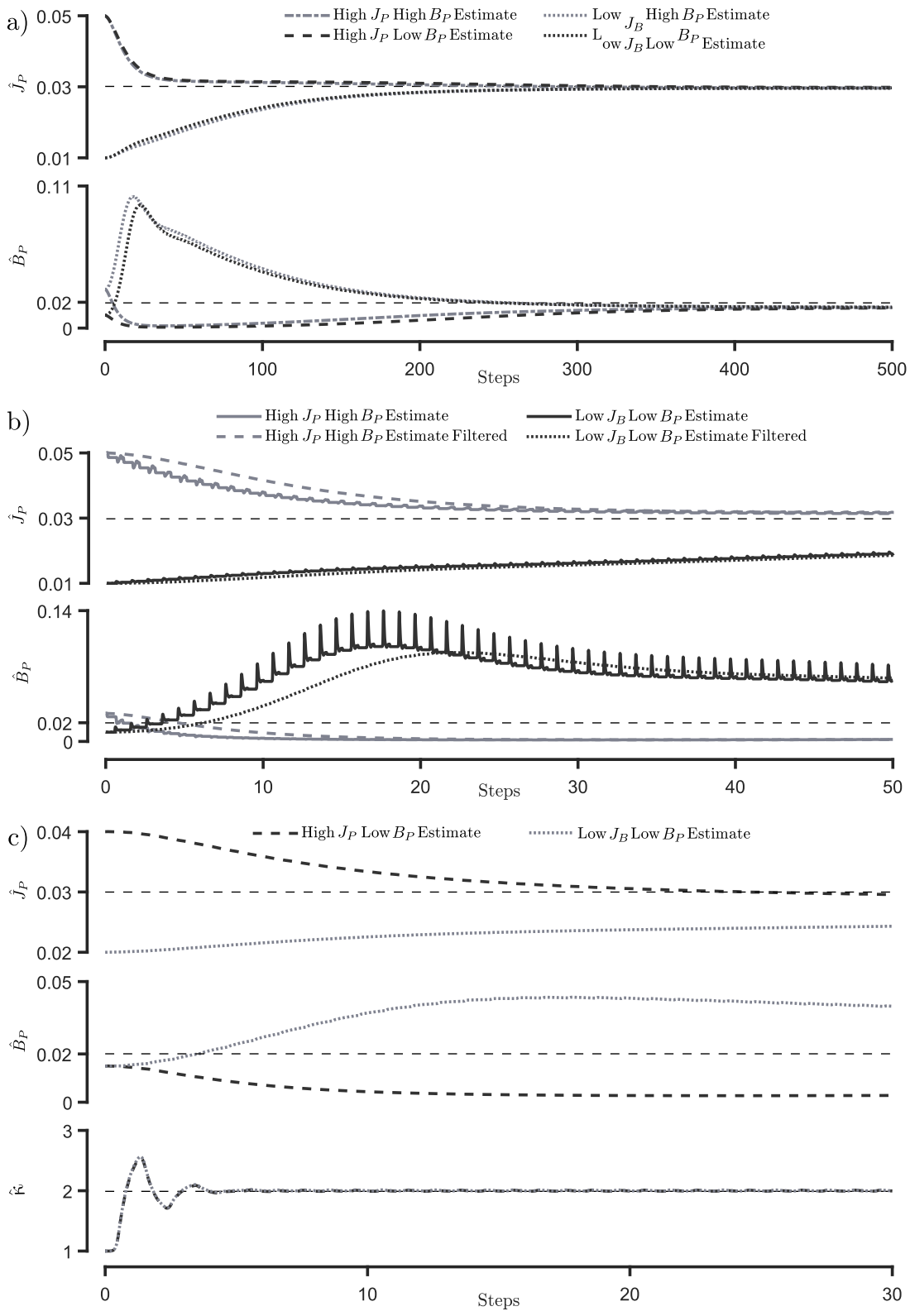

Figure 3.5: a) Filtered parameter estimation results of high and low parameter estimates. b) Raw and filtered parameter estimation results of two estimates. c) Filtered parameter estimation and κ estimation for a 50% disturbance torque. Where the straight dashed lines represent the real plant parameters.

Table 3.1: Parameter settling time per estimation scalar

a_J	5	5	5	10	10	10	15	15	15
a_B	15	20	25	35	40	45	30	35	40
J_P Settling Time [Steps]	9	9	5	5	5	5	3	3	3
B_P Settling Time [Steps]	33	20	29	28	28	34	26	24	32

3.5 Adaptive ESO Results & Discussion

The novel parameter estimation law presented in this Chapter shows the feasibility of identifying and minimizing endogenous disturbance torques. The result is a system that converges to the real plant parameters over a significant number of steps (i.e., > 300). The slow convergence is advantageous for adaptive AAFOs, providing a larger window for the adaptive laws as the rejected disturbance can vary from step to step.

To analyze the effects of the estimation gains a_J and a_B, their values are sampled with the convergence based on the number of steps to achieve a 5% settling time. The results, see Table. 3.1, express that the optimal gain values for convergence are $a_J = 5, a_B = 20$, using a first-order filter with a time constant of 5 seconds. The data shows that increasing $a_J > 5$ increases the settling time of J_P due to transience in convergence. Additionally, it is noted that regardless of the gains a_B and a_J, $\hat{B_P}$ is the last to convergence.

The proposed estimation law can be used for optimal and adaptive AAFO control schemes such as SMC, adaptive backstepping, and MPC. These controllers require an accurate model of the plant parameters to determine the best control signal. In combination with an ESO, the control systems only need to determine the control effort based on the plant parameters, where errors in the plant model will skew the controller's performance. Implementing the novel parameter estimation and disturbance rejection method allows the controller to solely focus on minimizing the trajectory tracking error.

3.6 Concluding Remarks

The adaptive ESO presented in this Chapter efficiently identifies and rejects unknown disturbances to an AAFO while estimating the plant's inertial and damping parameters. The novel parameter estimation law, based on identifying and correcting the error in dynamics modelling, can converge to the real plant parameters of the AAFO under various initial conditions. Implementing the adaptive observer with a state feedback controller can reduce the RMS tracking error by 5.2% and 71.1% in the presence of high and low feedback gains, respectively. Although not required for state feedback control, the estimation of the plant parameters will prove to be effective in model-based control systems, such as MPC, which is the focus of the next Chapter.

Chapter 4

Nonlinear Model Predictive Control of an Active Ankle-Foot Orthosis

THE goal of an AAFO control system is to achieve the nominal gait while minimizing the applied assistance to the user. Previous control systems used advanced SMC and backstepping control methods for AAFOs trajectory tracking. However, these control methods do not consider the middle ground between the magnitude of assistance and the plant's tracking accuracy, making MPC particularly advantageous. The MPC control response is based on minimizing a cost function; by incorporating the magnitude of the control effort in the cost function, the amount of assistance is reduced.

The objective of MPC is to identify the optimal control sequence for a set number of discrete time steps, known as the control horizon, to minimize a cost function. The cost function dictates the controller's response, containing multiple variables imperative to the desired action of the control system. In trajectory tracking, the cost function contains the tracking error and the magnitude of the control effort. The tracking error is determined by simulating the plant and comparing the plant's response to the desired trajectory within a given time, termed the prediction horizon. Following the cost function optimization, the control sequence for the first discrete time step of the control horizon is applied to the plant and repeated for each timestamp of the desired trajectory. The optimization problem is also subject to constraints, such as input saturation and a compliant plant model, to ensure the plant reacts correctly to the optimized control input. In linear MPC, the minimum of the objective function can be found by using quadratic programming methods. When the cost function is quadratic, an unconstrained MPC controller is simply a linear quadratic regulator [79]. However, linear MPC controllers with constraints require iterative computation using the Lagrangian algorithm, Karush-Kuhn-Tucker conditions, or other methods [79]. These methods are computationally expensive and therefore are hard to implement in real-time. Thus, fast MPC methods have been developed, in which the MPC controller computes only one optimization step per discrete time step in the control horizon [80].

In nonlinear MPC, iterative optimization is required to minimize the cost function. The plant must be simulated and the cost function evaluated for a set number of iterations. Due to the high computational cost required to solve the cost function, nonlinear MPC is implemented as suboptimal MPC, a suitable alternative to optimal MPC in most cases [81].

MPC is advantageous for AAFO control in two ways: First, MPC incorporates the magnitude of the control effort when determining the optimal control action, minimizing the assistance to the user while still achieving the desired trajectory. Second, the control method and resulting control values are based on the future trajectory allowing the controller to prepare for large acceleration instances, present multiple times within the gait cycle.

To the best of the author's knowledge, MPC has not been implemented for an AAFO before. The closest implementations are Wang *et al.* [82], which proposed an end-point MPC controller to control the input to the hip and knee joints of the LOPES exoskeleton in the swing phase. Zarandi *et al.* [83], designed and implemented a nonlinear MPC for the hip and knee joint using the active set method and time-varying linearization with constraints on the maximum torque output. To target the effects of foot drop, nonlinear MPC has been used to control functional electrical stimulation in [84]. The controller minimized the applied stimulation to the tibialis anterior to achieve a desired ankle angle in the swing phase. Other works have developed off-line MPC controllers, in which the controller estimates the plant model and calculates two gains to be sent to a low-level controller operating in real-time [85].

This Chapter proposes a novel nonlinear model predictive controller for AAFOs based on the model presented in Eq. (3.1) and its combination with the ESO presented in Chapter 3 for disturbance rejection. The work proposes a cost function for controlling the AAFO, including the nonlinear torque output constraint of the proposed crank-rocker actuator in Chapter 2. Further, this work describes an efficient control horizon estimation and optimization method for fast convergence of the suboptimal MPC controller. The presentation of work is structured as follows: Section 4.1 proposes the

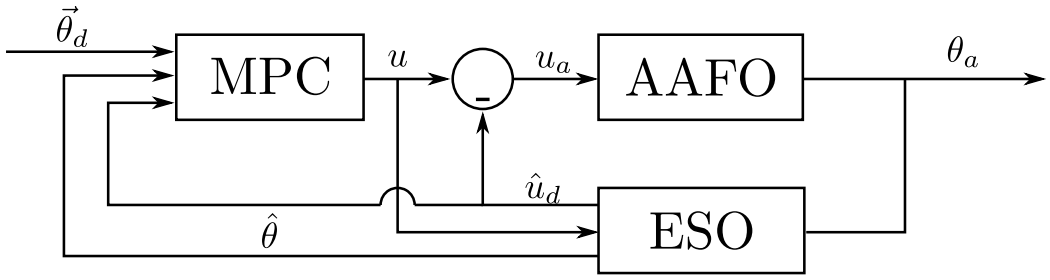

Figure 4.1: Proposed control system combining the MPC controller and an ESO. The MPC controller is provided with the desired trajectory ($\vec{\theta}_d$), plant angular position and speed (θ_a, $\dot{\theta}_a$), and the estimated disturbance torque $\hat{u}_d$. The MPC control provides the optimal control torque u to the plant and ESO. In which the AAFO plant determines the position and feeds the plant position to the ESO.

complete MPC controller from a cost function to optimization, section 4.2 shows the trajectory tracking capabilities of the MPC and ESO combination, and section 4.3 displays the real-time computation ability of the proposed method. Analysis of the theoretical and experimental results is presented in section 4.4, followed by conclusions in section 4.5.

4.1 Nonlinear Model Predictive Control of an AAFO

The nonlinear MPC presented in this Chapter is based on a linear plant model, previously described in Eq. (3.1), with a nonlinear constraint, controlling the AAFO in Fig. 2.10. The device is free to rotate normal to the sagittal plane, using the discrete nonlinear SEA presented in Chapter 2 to apply the required assistive torque to the ankle joint. A modified control topology of Fig. 3.1 is presented in Fig. 4.1, replacing the state feedback controller with a MPC controller. The ESO estimates exogenous and endogenous disturbances acting on the AAFO, and the inverse of the estimated disturbance is added to the control signal to aid the MPC. An MPC has three main components: (1) The cost function determines the controller response to the desired input based on the architecture and weighting matrices, (2) a method of initial control horizon selection to minimize the number of optimization iterations, and (3) subsequent optimization to allow the sub-optimal control sequence to be identified within a short time.

4.1.1 MPC Cost Function

The response of an MPC controller is based on finding the optimal control action for a given prediction horizon, which entails defining and finding the solution of a cost function. For an AAFO, the control system must track the desired trajectory, minimize the amount of assistance to the user, and abide by the nonlinear constraint of the discrete nonlinear actuator. The constraint is applied as a penalty function in a basic MPC quadratic cost function, expressed as:

$$C\left(\vec{u}\right) = \underbrace{\left\|\vec{\theta_d} - \vec{\theta_a}\right\|_Q^2}_{\text{trajectory}} + \underbrace{\left\|\vec{u}\right\|_R^2}_{\text{control}} + \underbrace{\left\|C_a(\vec{\tau_m})\right\|_S^2}_{\text{penalty function}} \tag{4.1}$$

with:

$$\vec{\theta_d} = [\theta_{d_1} \dots \theta_{d_N}], \quad \vec{\theta_a} = [\theta_{a_1} \dots \theta_{a_N}]$$
$$\vec{u} = [u_1 \dots u_M], \quad \vec{\tau_m} = [\tau_{m_1} \dots \tau_{m_M}]$$

where Q, R, and S are positive definite weighting matrices with a linear decreasing weight for Q and linear increasing for R and S. Vectors $\vec{\theta_d}$ and $\vec{\theta_a}$ are the desired ankle angular trajectory and simulated ankle position for prediction horizon size N; $\vec{u}$ and $\vec{\tau_m}$ are the control torque at the ankle and motor for a control horizon of size M, where $M \leq N$. Function C_a is a quadratic penalty ensuring that the maximum torque ($\tau_{m_{max}}$) of the motor and gearbox is not exceeded, defined as:

$$C_a(\tau_m) = \begin{cases} \left(\tau_m - \tau_{m_{max}}\right)^2, & \tau_m > \tau_{m_{max}} \\ 0, & \text{otherwise} \end{cases} \tag{4.2}$$

where $\tau_m = \tau_c$ is determined by Eq. (2.17), dependent on Eqs. (2.2)-(2.5) and (2.10) to (2.16), provided in the description of the discrete nonlinear SEA. The penalty function is a soft constraint and proved to have good performance in previous optimization problems [86]. The plant and cost function defined, the minimization of the objective function can be achieved using various methods. However, nonlinear MPC requires an accurate initial control horizon for fast convergence.

4.1.2 Initial Control Horizon Selection

State measurement of the plant must be obtained through the ESO to estimate the initial values of the control horizon ($\vec{u}$). Since the plant is linear and the desired angular trajectory ($\vec{\theta_d}$) and horizon time discretization (Δt) of the MPC prediction and control horizon are known. Invariant acceleration is assumed and determined for a sufficiently small Δt using:

$$\ddot{\theta}_t = \frac{2\left(\theta_{t+\Delta t} - \theta_t - \dot{\theta}_t \Delta t\right)}{\Delta t^2}, \tag{4.3}$$

where θ_t and $\theta_{t+\Delta t}$ are the initial position, and the next desired position in the prediction horizon, respectively, and t is the current time instance of the plant in the desired trajectory. The determined invariant rotational acceleration is then translated to the control torque (u_t), using the average speed and position:

$$u_t = J_P \ddot{\theta}_t + B_P \left(\frac{\dot{\theta}_{t+\Delta t} + \dot{\theta}_t}{2}\right) + K_P \left(\frac{\theta_{t+\Delta t} + \theta_t}{2}\right) \tag{4.4}$$

with:

$$\dot{\theta}_{t+\Delta t} = \dot{\theta}_t + \ddot{\theta}_t \Delta t.$$

The plant is then simulated with control u_t for time Δt to determine the new plant position. The remainder of the control horizon (M) is incrementally determined, using the position that is reached at the last timestamp and the desired position at the next timestamp ($\theta_{d_{t+\Delta t}}$), where $\vec{u} = [u_t, \ldots, u_{t+(N-1)\Delta t}]$. If $M < N$, the last control horizon value u_M is determined using the last position of the prediction horizon θ_{d_N}.

The method of determining the initial control horizon is tested in response to a step input, see Fig. 4.2a. The system response is marginally stable and is not a suitable initial control sequence. Therefore, to reduce the chattering presented by the initial guess, a portion of the nonlinear gain function defined as [61]:

$$fal\left(u_q, \phi\right) = |u_q|^{\phi} \text{sign}(u_q) \tag{4.5}$$

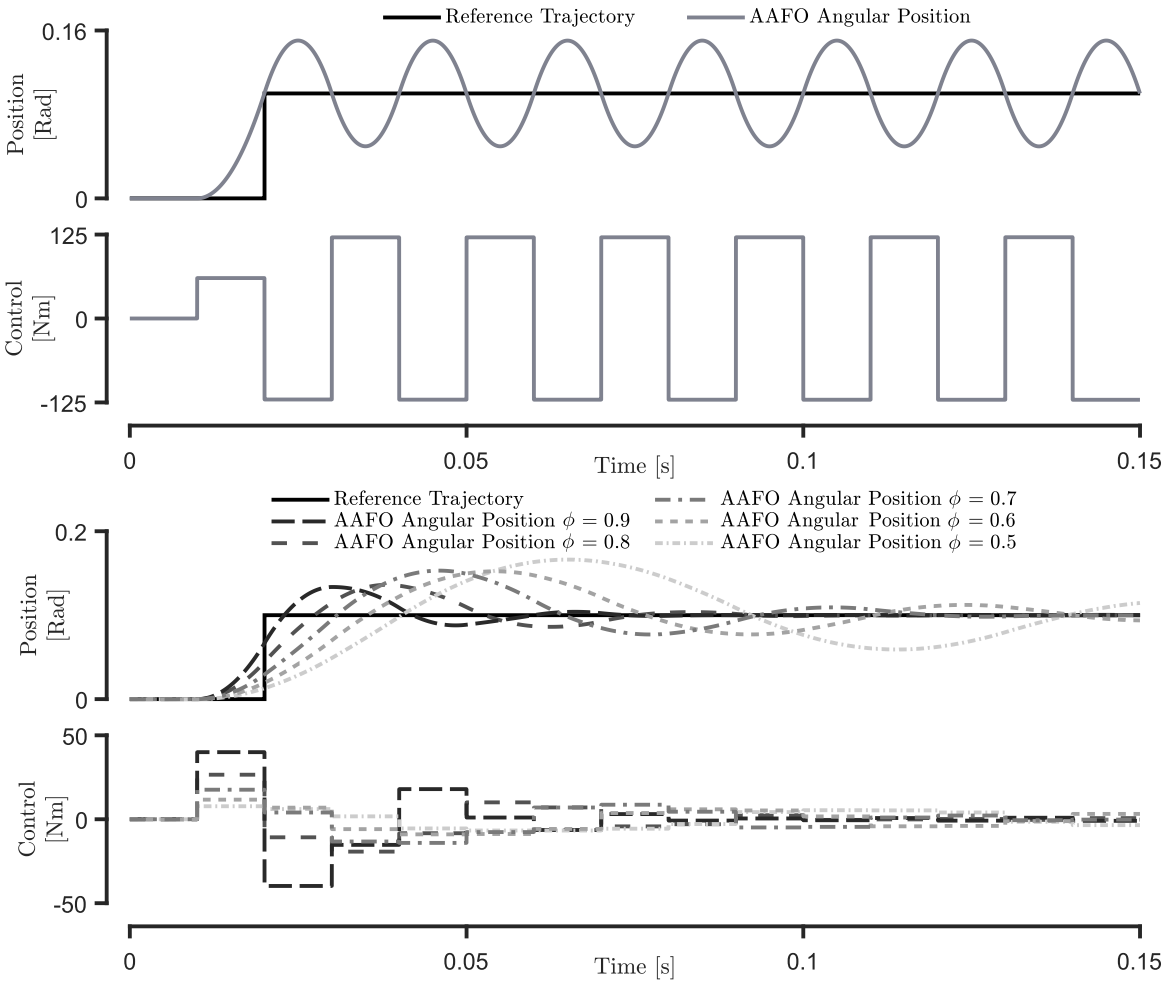

Figure 4.2: a) Linear approximation control in response to a step input of 0.1 rad at $t = 0.2$. b) Result of linear approximation control with varying saturation gains (ϕ).

is used to dampen the determined control input, where $\phi \in [0, 1]$ is the saturation gain, and $q \in [1, M]$ is the index of $\vec{u}$. Implementing Eq. (4.5) before the simulation of time Δt results in a stable response to a step input, see Fig. 4.2b. Therefore, the method of invariant acceleration to determine the required control effort is a sufficient initial guess for the MPC controller.

4.1.3 MPC Cost Function Optimization

The cost function can then be minimized with a stable initial guess. The Gauss-Newton optimizer is commonly used to minimize least-squares objective functions; however, the algorithm targets the closest minima/maxima to the initial guess. The

objective space of an optimization problem with more than 2 dimensions is difficult to visualize, and it is unknown if the objective space has multi-modal attributes due to the designed cost function and nonlinear constraint. To locate the minima in the objective space, another Newton-based method can be used before exploring the minima using Gauss-Newton.

The Newton-Raphson method aims to identify a root of a given function, with the update term $\frac{f(x)}{f'(x)}$. Multi-variate Newton-Raphson updates the decision variables via:

$$\vec{u}_{j+1} = \vec{u}_j + \underbrace{\upsilon G_j^{-1} C(\vec{u}_j)}_{\text{update term}} \tag{4.6}$$

where j indicates the previous iteration, $C(\vec{u}_j)$ is the cost at iteration j, υ is the Newton step scaling factor, and G is the Jacobian matrix, defined as:

$$G_j = \frac{\partial C(\vec{u}_j)}{\partial \vec{u}_j} = \begin{bmatrix} \frac{\partial C(\vec{u}_j)}{\partial u_1} & \cdots & \frac{\partial C(\vec{u}_j)}{\partial u_M} \end{bmatrix}. \tag{4.7}$$

When the Newton-Raphson method falls into a local minimum, the magnitude of the update term increases. Subsequently, the Gauss-Newton method is used to explore the local minimum. The update term of the Gauss-Newton method is determined as:

$$\vec{u}_{j+1} = \vec{u}_j + \underbrace{\upsilon \left(G_j G_j^T + \lambda I \right)^{-1} G_j C(\vec{u}_j)}_{\text{update term}} \tag{4.8}$$

where $G_j G_j^T$ is an approximation of the Hessian matrix, and I is an $M \times M$ identity matrix combined with a small scalar λ to ensure matrix inversion. The search method from the fast jaguar algorithm is adapted to determine the best step size [87]. The jaguar algorithm is based on the hunting nature of the jaguar in which a positive result accelerates the animal, and a negative result decelerates the animal. This method can be used to quickly conduct a local search of the minimum identified by the Newton-based algorithms. Once an instance of a minimum is identified and the following iteration results in an increased objective function value, the variable step method is

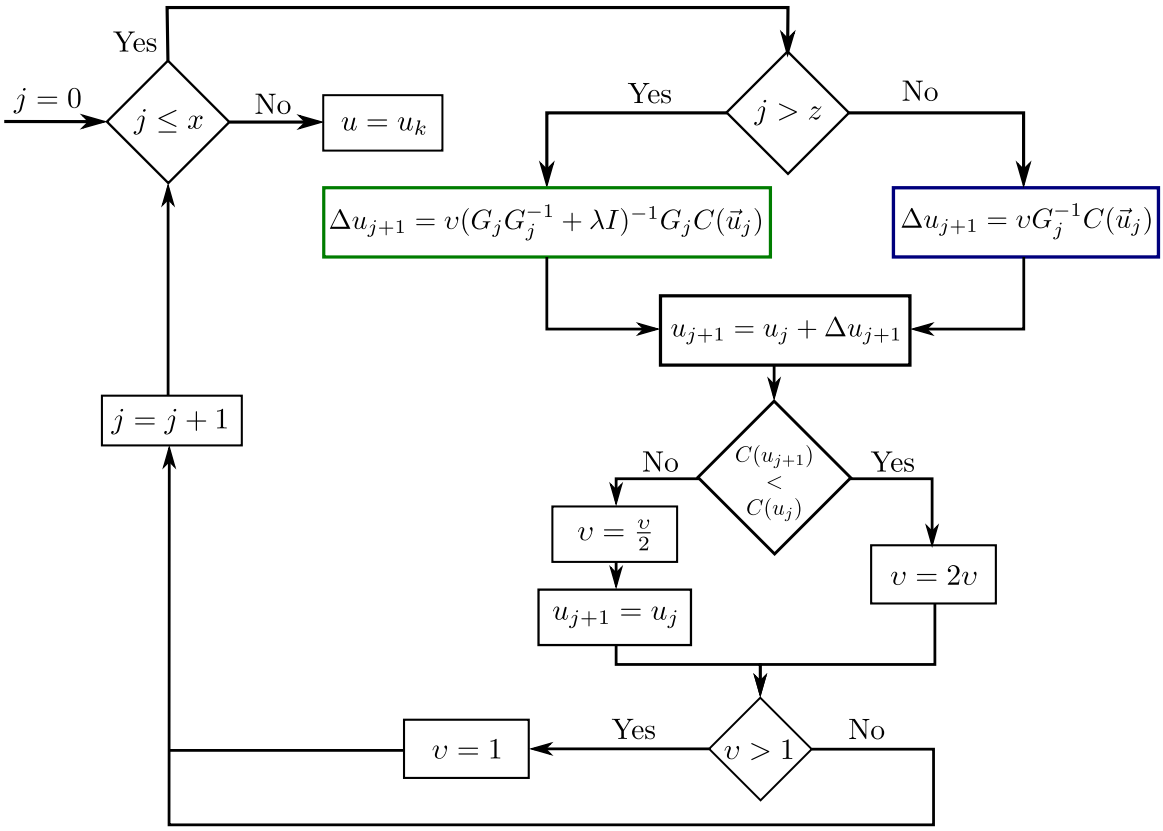

Figure 4.3: MPC optimization method, in which the Newton-Raphson algorithm (blue) is implemented z times followed by $z - x$ Gauss-Newton (green) iterations, where x and j are the total number and current iteration, respectively.

implemented based on the Jaguar algorithm, where the scalar υ is updated as:

$$\upsilon = \begin{cases} 2\upsilon, & \text{if } C(\vec{u}_{j+1}) < C(\vec{u}_j) \\ 1, & \text{if } \upsilon > 1 \\ \frac{\upsilon}{2}, & \text{otherwise} \end{cases} \tag{4.9}$$

in which $C(\vec{u}_{j+1})$ and $C(\vec{u}_j)$ is the result of the objective function at the current and previous iteration and υ is limited to ≤ 1. The flow of the optimization procedure is presented in Fig. 4.3, where x and z are the total number of iterations and the number of Newton-Raphson iterations, respectively.

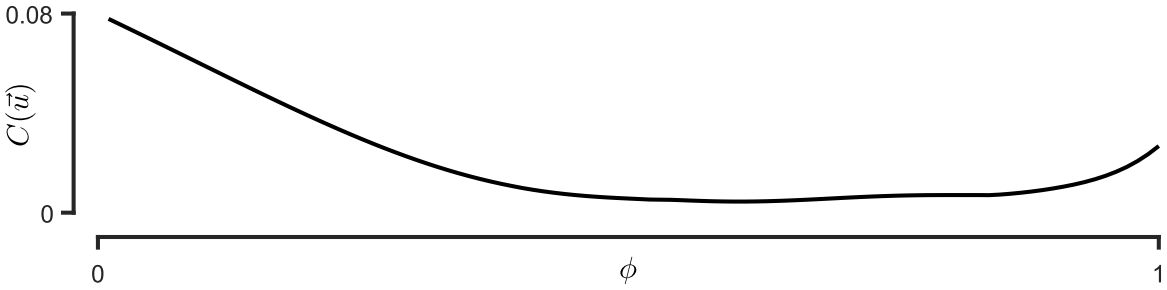

Figure 4.4: Saturation Gain vs MPC Cost Function.

4.2 MPC Simulation Results

Simulations are conducted to analyze the benefits and restrictions of the proposed nonlinear MPC controller and its use in conjunction with an ESO for disturbance rejection. The MPC controller is initialized with a control and prediction horizon of $M = 3$ and $N = 5$, operating at 100 Hz in conjunction with a 200 Hz ESO presented in Chapter 3. The proposed optimizer is given the parameters $x = 50$ and $z = 2$ to minimize the objective function. Prior to simulations, the cost function matrices Q, R, and S are given weights of 10, 10^{-4}, and 1, respectively. The saturation gain $\phi = 0.65$ was determined by finding the minimum between the saturation gain and MPC cost function when exposed to a ramp input, shown in Fig. 4.4. The gait trajectory from [9], shown in Fig. 1.2, is used as the desired angular trajectory of the ankle joint and gait disturbance for the simulations. For comparison, a PD controller with a sampling rate of 1 kHz tuned for trajectory tracking is implemented, achieving a 0.063s settling time for a 0.1 rad step input. The PD controller replaces the state feedback controller as the developed AAFO does not provide accurate full state measurement. An ESO is combined with the PD controller for disturbance rejection to create an accurate comparison.

Three types of simulations are conducted, i.e., with no disturbance, nominal gait disturbance, and sinusoidal disturbance. As expressed in Chapter 1, the plant parameters of an AAFO cannot be measured. Therefore, three variations of the plant model are simulated:

Table 4.1: RMS error simulation results for MPC and PD controller in combination with the ESO in the presence of gait and sinusoidal disturbance (10^{-3}) [Rad]

Controller	No Disturbance	Gait Disturbance	Sinusoidal Disturbance
MPC	2.09	336	540
MPC+ESO	1.80	9.74	8.36
MPC+ESO PME_1	3.29	11.0	9.30
MPC+ESO PME_2	1.56	9.54	7.38
PD	5.20	142	166
PD+ESO	5.16	11.5	9.52
PD+ESO PME_1	5.46	11.7	9.68
PD+ESO PME_2	4.96	11.3	9.41

1. No modelling error: The plant, MPC controller, and ESO have the same plant parameters.

2. Plant Modelling Error 1 (PME_1): The MPC controller and ESO are given the same plant parameters of the first variation. However, the simulated plant is given a 33% higher inertial value.

3. Plant Modelling Error 2 (PME_2): The MPC controller and ESO are given the same plant parameters of the first variation. However, the simulated plant is given a 33% and 50% lower inertial and damping value, respectively.

The simulation results are shown in Fig. 4.5, and the respective RMS tracking error is presented in Table 4.1. The results show that the MPC and ESO combination is the best trajectory tracking controller even in the presence of high amplitude gait and sinusoidal disturbance. The combination allows the MPC controller to focus on accurate trajectory tracking while the ESO rejects any disturbance applied to the plant. In Fig. 4.5a, it is evident that the ESO is able to identify and reject the disturbance due to the plant modelling error, where PME_1 and PME_2 result in opposing disturbance torques due to the large difference in rotational inertia. The trend is also visible in Fig. 4.5b and 4.5c, where the PME_1 and PME_2 traces deviate from the normal disturbance error trend. Fig. 4.5b and 4.5c show that the estimated disturbance lags the simulated disturbance, resulting in an increased trajectory tracking error when

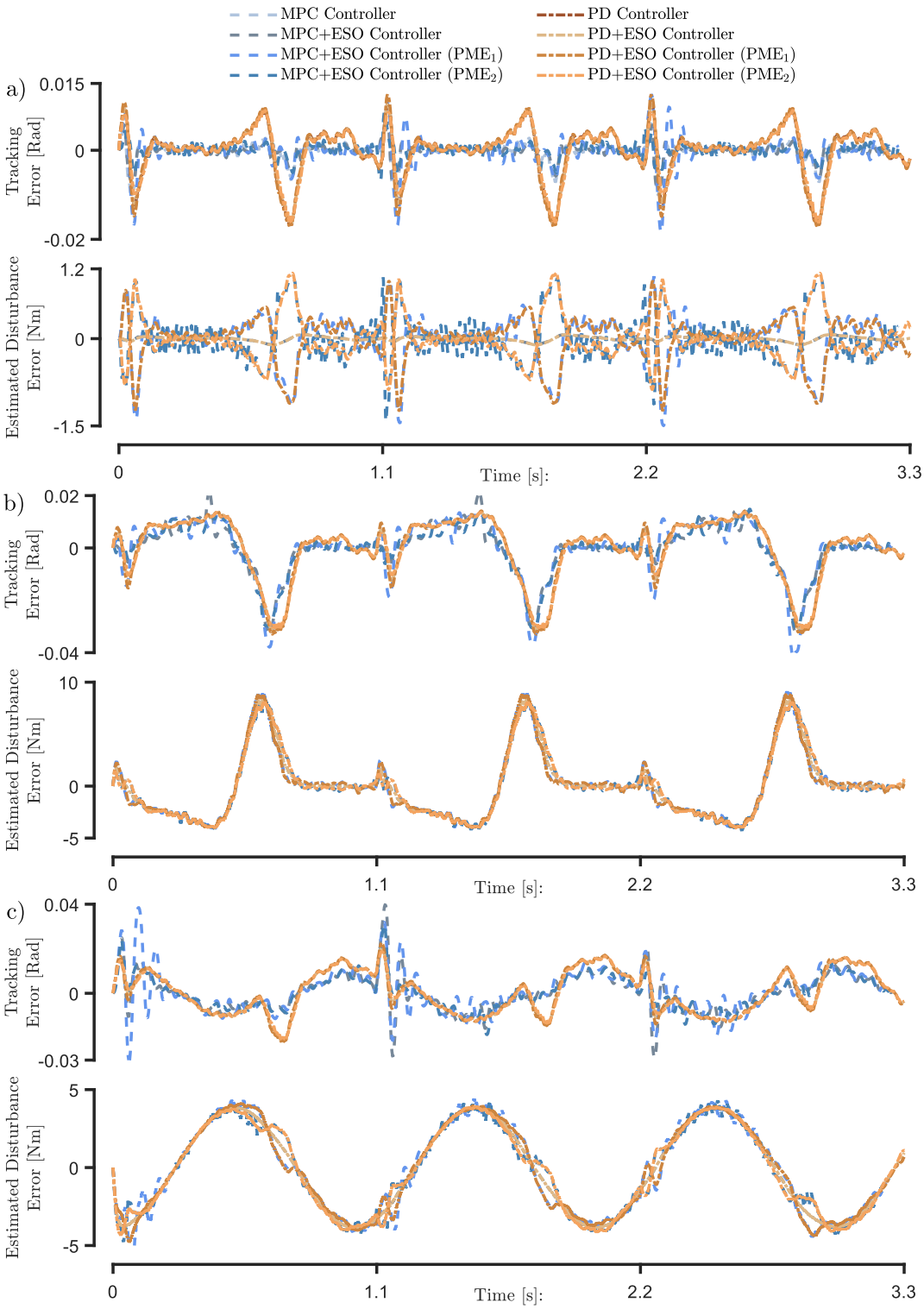

Figure 4.5: a) Simulation results without disturbances, b) simulation results with gait disturbances for a 40 kg users, and c) 1 Hz 40 Nm sinusoidal disturbances. Tracking error is based on the ankle joint's actual and desired angular trajectory. Estimated disturbance error is the difference between the measured and rejected disturbance by the ESO and the induced disturbance torque.

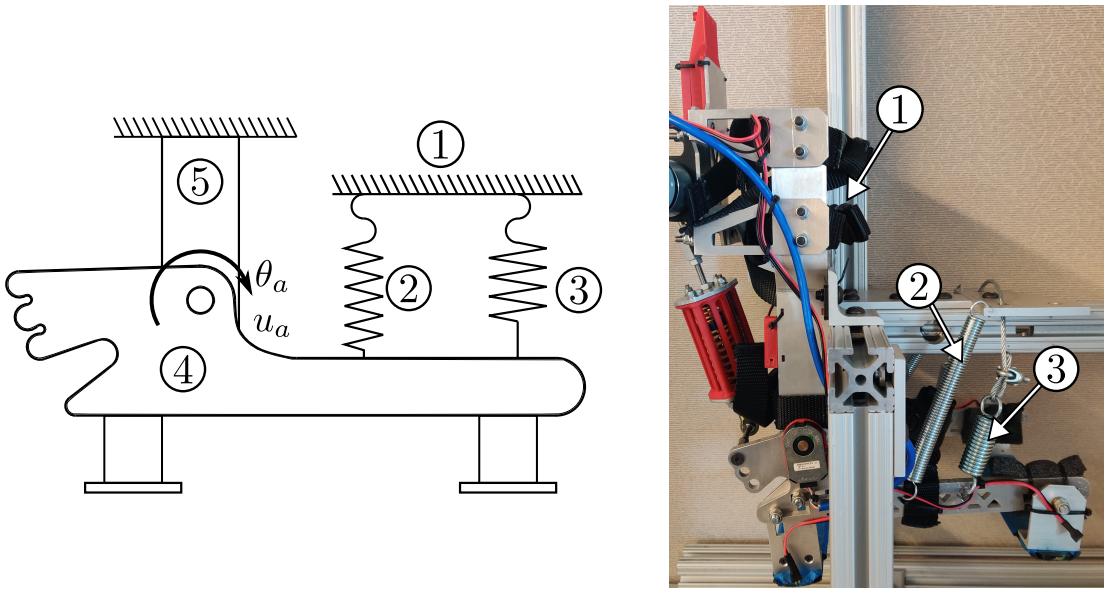

Figure 4.6: MPC experimental setup, with a rigid structure ① to fix the AAFO shank ⑤. Disturbance is created using unidirectional springs with a 3.0 N/mm ② and 13.9 N/mm ③ stiffness, connected between the test structure and foot-bed ④. The springs are combined to create a low, medium, and high disturbance during plantarflexion.

the disturbance torque changes. The MPC and ESO combination is capable of handling both exogenous and endogenous disturbances while achieving better tracking performance compared to an ESO and PD controller tuned for a fast-settling time.

4.3 MPC & ESO Experimental Validation

The AAFO prototype presented in Chapter 2 is used to validate the MPC controller. The MPC and ESO are implemented in C++, with the MPC controller operating at 100 Hz and the ESO at 200 Hz. The PD controller used for comparison is also included, with a sampling frequency of 1 kHz.

Validation of the proposed control system is accomplished by conducting two sets of experiments. In experiment 1, the AAFO is mounted on the test stand (see Fig. 4.6) and is free from external disturbances. For experiment 2, the AAFO remains in the test stand, where two sets of springs are used individually and in combination to generate light, medium, and heavy disturbance during plantarflexion motion (see Fig. 4.6), with a peak torque of 16.7 Nm, 27.94 Nm, and 31.54 Nm, respectively.

Table 4.2: Experimental results

Disturbance	MPC+ESO	PD+ESO	MPC+ESO	PD+ESO
	RMS Tracking Error (10^{-3}) [Rad]		Average Current [mA]	
No Dist.	89.4	70.6	484	467
Light Dist.	95.4	86.9	432	427
Medium Dist.	97.5	90.0	446	448
High Dist.	106.2	105.5	528	648

The MPC and PD controllers are required to track the nominal gait trajectory at a speed of 3.3 s. Fig. 4.7 shows the trajectory tracking results of the MPC+ESO and PD+ESO controllers in the presence of variable disturbance and Table. 4.2 displays the RMS tracking error and average current. The mean, standard deviation, and maximum computation time for the MPC controller are 99.29 μs, 70.66 μs, and 396.9 μs, respectively, where the same metrics for the PD controller are 0.34 μs, 0.08 μs, and 0.7 μs, respectively. Similarly, the computation time of the ESO has a mean, standard deviation, and maximum of 42.8 μs, 3.7 μs, and 89.5 μs in the MPC experiment and 46.5 μs, 3.2 μs, and 120 μs for the PD experiment.

4.4 Nonlinear MPC and Results & Discussion

The simulation and experimental results show the feasibility and benefits of the proposed real-time MPC controller in combination with the ESO. The simulations prove that the proposed architecture has a significant benefit with an RMS tracking error reduction of 58.3%, 12.3%, and 12.6% in the presence of no disturbance, nominal gait disturbance, and sinusoidal disturbance, with respect to the PD and ESO combination. The proposed method to determine the initial control horizon allows the optimizer to find the suboptimal solution, reducing the tracking error quickly. However, the implementation of the ESO must be included to accurately track the nominal trajectory in the presence of high disturbance and errors in the plant model.

Experimental testing outlines two benefits of the MPC controller. First, the required torque from the MPC and ESO combination is reduced by 16.3% compared to the

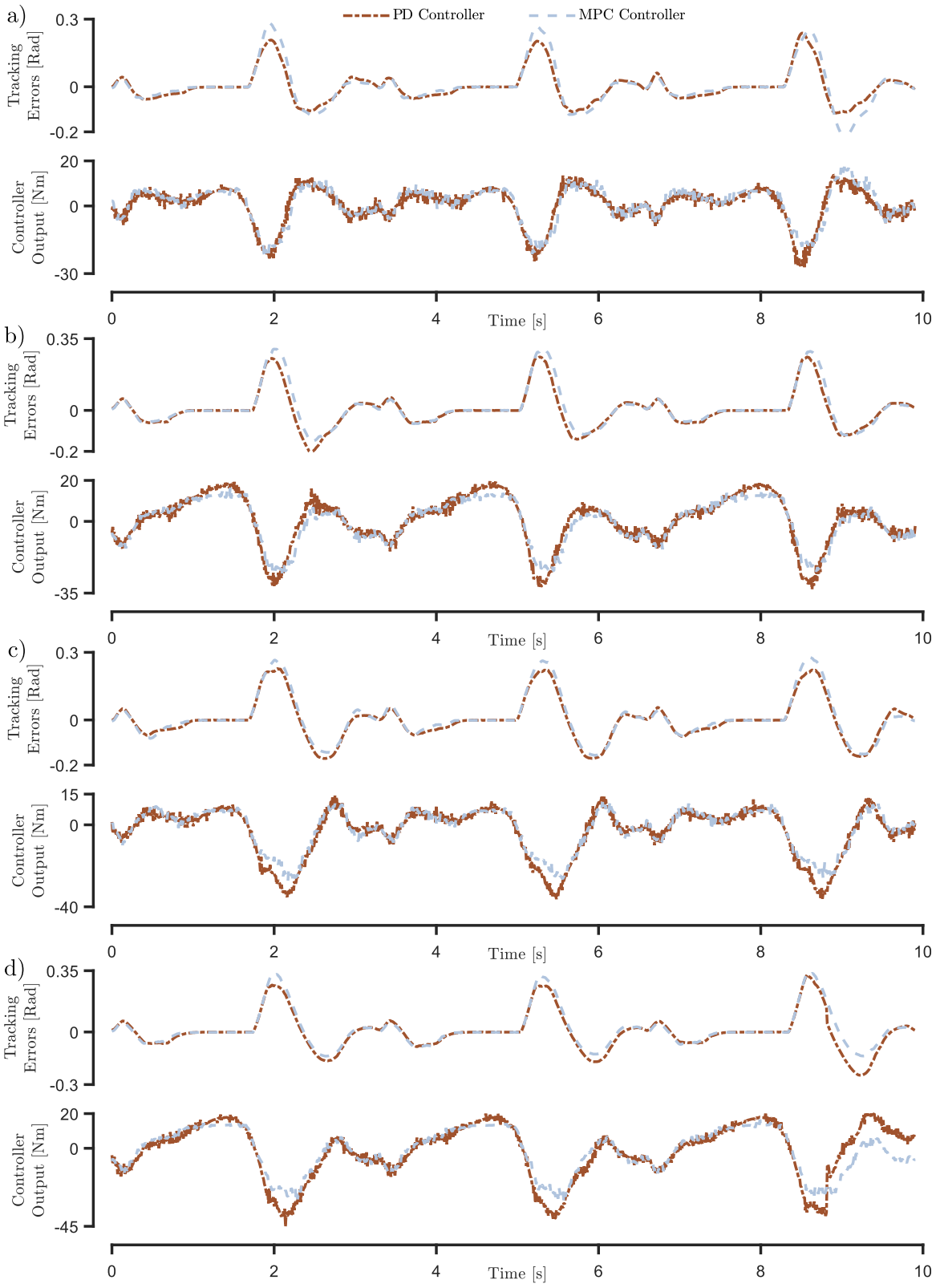

Figure 4.7: Tracking error and controller outputs in the presence of a) no disturbance, b) light disturbance, c) medium disturbance, and d) heavy disturbance is also presented.

PD and ESO combination in the presence of high disturbances. Fig. 4.7 shows the proactive approach of the MPC controller reducing the control value in anticipation of the future trajectory. Table. 4.2 shows that the MPC and PD controller have similar tracking errors with a reduced measured input current seen by the MPC at high disturbances. The results show that the MPC has a balanced control approach, opposed to the high gain PD controller. Second, the experiments show the real-time capability of the proposed controller. The combined maximum MPC and ESO computation time did not exceed 486.4 μs, significantly less than the ESO and MPC controller sampling time (5 and 10 ms, respectively).

However, the control system operates on three threads on a 2.5 GHz processor, which is not an available clock speed for a typical microcontroller, such as the 480 MHz and 240 Dual Arm® core STMicroelectronics STM32H745XI rev X device. To compare the two devices, the CoreMark® score is referenced. The experimental setup CPU has a score of 5115.18, whereas the STMicroelectronics STM32H745XI has a score of 3223.82. Therefore, the 1/10 computation time vs MPC sampling period factor of the presented experimental step shows that the control system should still be sufficient in achieving real-time operation when adjusted for operation in microcontrollers.

Fig 4.7 shows the trajectory tracking capability of the proposed real-time MPC and ESO and the PD and ESO controller. A large contribution to the observed error is torque application delay. A significant delay is present between the MPC and PD controllers' desired and actual trajectory (see Fig 4.8a). The delay results from the activation time of the DC motor and gearbox combination. Fig 4.8b shows the motor's position response to a step input position. It is evident that 90 ms elapses before motion is present at the gearbox. The delay can be included in future plant models to reduce the tracking error. Consequently, the PD controller has increased trajectory tracking performance in the presence of an actuation delay, as the high tuning gains generate a substantial torque in the presence of increased tracking error. The MPC and ESO combination does outperform the PD controller at higher disturbances, closing the RMS tracking error difference between the controller while maintaining a

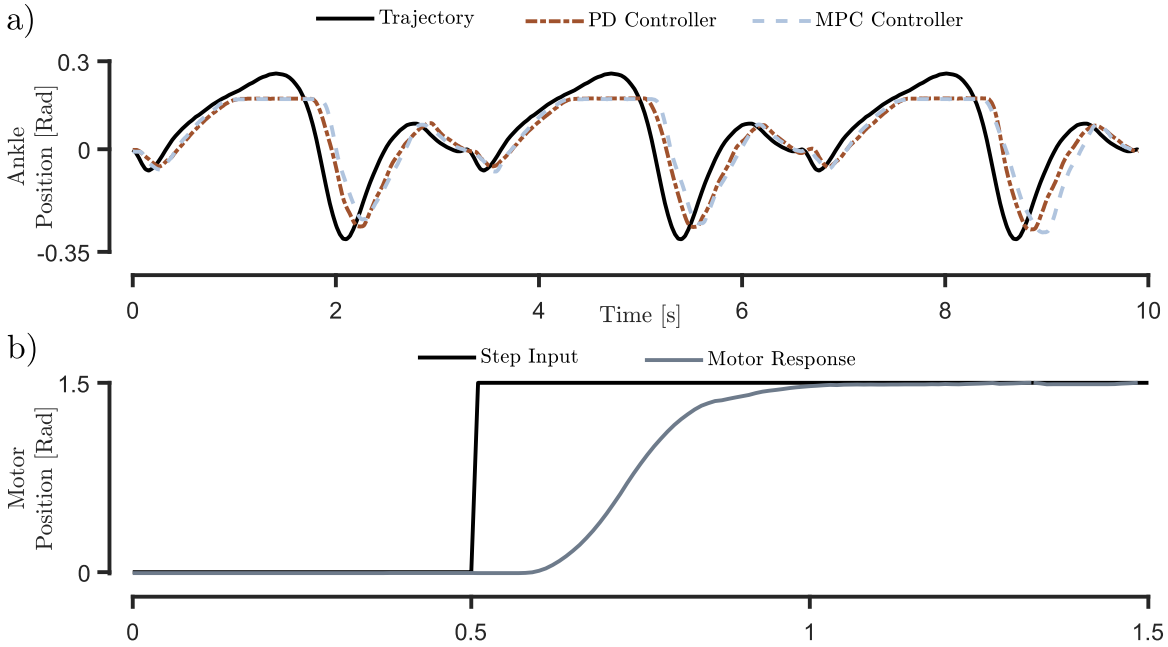

Figure 4.8: a) MPC and PD controller tracking without disturbance. It is noted that the physical limitations of the AAFO actuator in the presence of no disturbance restrict the dorsiflexion range of motion to 0.174 rad. The significant lag in the trajectory tracking is due to the slow response of the DC motor driving the actuator, in which the step response is shown in b).

balance between the tracking error and control effort, resulting in a reduced average current.

The proposed system is an effective control strategy for AAFOs. The MPC targets accurate trajectory tracking required to achieve a nominal gait with the conscious effort to minimize the system's applied torque. The ESO identifies and rejects exogenous and endogenous disturbances to the system. An ESO is seen as an AAFO user dependency, as the ESO supplements the exogenous disturbance due to insufficient push-off from the users. Therefore, limits can be applied to the ESO to allow only a certain percentage of the nominal ankle torque to be rejected. In the presence of increased muscle activation of the user during operation, the weight matrix R of the MPC cost function can be incremented, and the percentage of nominal ankle torque from the ESO decremented until there is no longer assistance required for user locomotion.

4.5 Concluding Remarks

This Chapter presents a nonlinear MPC controller for AAFOs, combined with the ESO in Chapter 3. The AAFO is considered a linear plant with nonlinear constraints due to the design of the discrete nonlinear SEA. Therefore, a nonlinear MPC controller is developed and combined with an ESO to minimize the effect of gait disturbances and errors in plant modelling while achieving accurate trajectory tracking. Simulation and physical tests show the tracking accuracy of the proposed control topology and the capability of real-time operation. The benefit of MPC implementation is the inclusion of the control magnitude in the cost function, allowing the controller to minimize assistance to the user.

Chapter 5

Conclusions & Recommendations

THE design and control of AAFOs target the reduction of gait deficiencies, such as foot drop. The optimal AAFO aids a user in achieving the nominal gait cycle while restricting the amount of provided assistance. An AAFO has three components: the mechanical structure, an actuator to provide torque assistance, and a control system designed to achieve a nominal gait. Advances in the AAFO mechanical structure have been minimal, with research focusing on the actuator and control system design. The ideal AAFO is lightweight yet capable of providing full assistance to the user. Previous designs have targeted an ideal actuator, employing pneumatic actuators for their high force-to-weigh ratio, optimizing the SEA actuator to reduce the input power, and developing VSAs to recreate the stiffness of the ankle joint. On their own, each actuator design is sub-optimal. The pneumatic actuators provide sufficient force with a low footprint and mass, but require a constant tethered supply of air. The optimized SEA reduced the peak power input to the device but can be further improved using variable stiffness methods. VSAs are excellent at creating the desired stiffness at the ankle joint; however, they are complex with low assistive torque capability. Therefore, the research in this thesis is based on identifying a lightweight actuator capable of providing the required assistance to the ankle joint. The optimal AAFO control system can decipher the required amount of assistance without overbearing the user. Previous control methods are based on gait phase and trajectory tracking control. Trajectory tracking is the favoured method of achieving the desired gait motion. The control methods previously employed only target the reduction in tracking error and do not consider the amount of assistance provided to the user. In addition, the model parameters of an AAFO and ankle joint combination cannot be measured, thus affecting the performance of model-based control methods.

This thesis targets the design and optimization of a low-power actuator for AAFOs and a control method that allows angular trajectory tracking, while minimizing the applied control signal. Chapter 2 presented the novel discrete nonlinear SEA bridging the advantages of the optimized SEA and VSA. The actuator is designed to minimize its mass while applying the necessary power to the ankle joint. A novel elastic element for a SEA is proposed to address this objective. The discrete nonlinear method is

simple; a set of linear springs are engaged in parallel at set displacement intervals to create an increasing stiffness correlated to the number of active springs. In the stance phase of the gait cycle, the ankle joint continually increases stiffness until push-off is achieved. Therefore, the discrete nonlinear stiffness is optimal for regenerative braking in AAFOs. The implementation of the novel stiffness method results in a peak power reduction of 77.2% compared to the biological ankle power. The best power peak reduction was 74.4% in recent literature and required two stiffness elements, using both a SEA and uni-directional PEA. The proposed design has one stiffness element within a small footprint, encompassing one discrete stiffness within the other. A crank-rocker mechanism is used to actuate the optimized SEA, minimizing the amount of electrical power required during instances of high torque at the ankle joint. The configuration also allows for a compact design, where the crank, rocker, and connecting link can all be optimized to reduce the link lengths and thus the mass, presenting a lightweight actuator with an optimized stiffness element for regenerative braking. A prototype AAFO with the proposed actuator is developed and verified using static load tests and experimental walking trials.

The control system presented in this thesis targets the optimal control interaction with the user. The goal of an AAFO is to limit the assistance to the user while ensuring a nominal gait is achieved. Two components are developed in this thesis; the first is the identification of the disturbances presented to an AAFO, and the second is a nonlinear MPC. AAFO disturbance is known to be exogenous, the torque required for push-off, and endogenous, the torque due to the error in the dynamics model. The adaptive ESO presented in Chapter 3 is designed to first reject the total disturbance to the system, followed by an estimation of the model parameters, such that a model-based control scheme can be used. The adaptive determination of the parameters is based on extracting the endogenous disturbance torque by subtracting the scaled nominal gait disturbance from the ESO estimated disturbance. The adaptive ESO can identify the actual plant parameters and subsequently improve the trajectory tracking of a state feedback controller. Identifying the plant parameters opens the door for MPC to be applied to an AAFO. The second proposed component is the nonlinear MPC

presented in Chapter 4, such that the AAFO tracks the desired angular trajectory but limits the amount of assistance to the user. The nonlinear MPC model is based on a linear plant with a nonlinear constraint due to the implementation of the discrete nonlinear actuator. A cost function, a method to determine the initial control horizon, and optimization procedure are presented to track the desired trajectory efficiently. Combining the ESO and nonlinear MPC controller results in an effective trajectory tracking method, reducing the RMSE by 58.3%, 12.3%, and 12.6% in the presence of undisturbed, gait disturbed, and sinusoidally disturbed environments, respectively. Physical testing shows the ability of the MPC and ESO to track the gait trajectory while minimizing the assistance to the ankle joint.

5.1 Road Map for Future Work

Future work related to the presented design and control of the proposed AAFO can focus on the following:

1. Continued in-depth optimization of the discrete nonlinear actuator can be explored. The material properties, standard spring sizes and stiffness, and motor and gearbox combinations can all be included in the optimization to further reduce the mass of the actuator assembly. Increasing the number of discrete stiffness changes can also be exploited ($n > 2$) to increase the optimality of regenerative braking.

2. Further actuator development can focus on a lightweight gearbox for the proposed discrete nonlinear crank-rocker SEA. Currently, the employed gearing is a 3-stage planetary gearbox with a length of 53.5 mm. Implementing a strain wave or cycloidal gearbox would reduce the motor and gearbox combination's size while targeting the optimal gear reduction.

3. The 90 ms actuation delay presented in Section 4.3 can be incorporated into the model of the MPC controller to improve the trajectory tracking capability of the experimental setup.

4. Adapting the MPC cost function and allowable ESO torque would add autonomy to the control system, another step towards achieving a market-ready device. As stated in Chapter 4, the user could reduce the dependence on the AAFO by increasing the weighting matrix Q and reducing the reject torque's allowable magnitude.

5. Further, the control system proposed in this thesis can be implemented on an embedded processor, creating an untethered AAFO that does not require a clinical setting to operate.

6. The development of a 2-DOF AAFO by combining the discrete nonlinear SEA with the 2-DOF design presented in [47]. The presented discrete nonlinear design in Fig. 2.6 has two sets of springs, which can be separated into two actuators to control plantarflexion/dorsiflexion and inversion/eversion.

7. Applying embedded sensors in an AAFO is vital to present a product to market. The AAFO presented in this thesis surrounded the user's shoe and had a mass of 2.85 kg, in which a significant amount of mass is due to the aluminum structure of the device. Both the lever arm and sensors presented can be incorporated into a passive polypropylene AFO to reduce the mass and size of the AAFO

Addressing the above recommendations will enable the developed actuator and control system presented in this thesis to become an everyday solution for a user suffering from foot drop.

References

[1] T. Oba, H. Kadone, M. Hassan, and K. Suzuki, "Robotic ankle–foot orthosis with a variable viscosity link using mr fluid," *IEEE/ASME Transactions on Mechatronics*, vol. 24, no. 2, pp. 495–504, 2019.

[2] V. Arnez-Paniagua, H. Rifaï, Y. Amirat, M. Ghedira, J. Gracies, and S. Mohammed, "Adaptive control of an actuated ankle foot orthosis for paretic patients," *Control Engineering Practice*, vol. 90, pp. 207–220, 2019.

[3] A. E. Carolus, M. Becker, J. Cuny, R. Smektala, K. Schmieder, and C. Brenke, "The interdisciplinary management of foot drop," *Deutsches Ärzteblatt International*, vol. 116, no. 20, p. 347, 2019.

[4] F. D. Westhout, L. S. Paré, and M. E. Linskey, "Central causes of foot drop: rare and underappreciated differential diagnoses," *The journal of spinal cord medicine*, vol. 30, no. 1, pp. 62–66, 2007.

[5] "Stroke report," Heart and Stroke Foundatino of Canada, Tech. Rep., 2018.

[6] J. Jiang, K.-M. Lee, and J. Ji, "Design criteria for developing an anatomy-based ankle-foot-orthosis: A state-of-the art review and needs of mind, motor and motion recovery following stroke," in *2018 IEEE/ASME International Conference on Advanced Intelligent Mechatronics (AIM)*. IEEE, 2018, pp. 1057–1062.

[7] A. Erdogan, B. Celebi, A. C. Satici, and V. Patoglu, "Assist on-ankle: a reconfigurable ankle exoskeleton with series-elastic actuation," *Autonomous Robots*, vol. 41, no. 3, pp. 743–758, 2017.

[8] R. Chin, E. T. Hsiao-Wecksler, E. Loth, G. Kogler, S. D. Manwaring, S. N. Tyson, K. A. Shorter, and J. N. Gilmer, "A pneumatic power harvesting ankle-foot orthosis to prevent foot-drop," *Journal of neuroengineering and rehabilitation*, vol. 6, no. 1, p. 19, 2009.

[9] G. Bovi, M. Rabuffetti, P. Mazzoleni, and M. Ferrarin, "A multiple-task gait analysis approach: kinematic, kinetic and emg reference data for healthy young and adult subjects," *Gait & posture*, vol. 33, no. 1, pp. 6–13, 2011.

[10] R. Ranaweera, R. Abayasiri, R. Gopura, T. Jayawardena, and G. Mann, "Design and analysis of an anthropomorphic two-dof ankle-foot orthosis," in *2019 5th International Conference on Control, Automation and Robotics (ICCAR)*. IEEE, 2019, pp. 802–807.

[11] C. L. Brockett and G. J. Chapman, "Biomechanics of the ankle," *Orthopaedics and trauma*, vol. 30, no. 3, pp. 232–238, 2016.

[12] A. Agrawal, S. K. Banala, S. K. Agrawal, and S. A. Binder-Macleod, "Design of a two degree-of-freedom ankle-foot orthosis for robotic rehabilitation," in *9th International Conference on Rehabilitation Robotics, 2005. ICORR 2005.* IEEE, 2005, pp. 41–44.

[13] I. Wiszomirska, M. Błażkiewicz, K. Kaczmarczyk, G. Brzuszkiewicz-Kuźmicka, and A. Wit, "Effect of drop foot on spatiotemporal, kinematic, and kinetic parameters during gait," *Applied bionics and biomechanics*, vol. 2017, 2017.

[14] W. Huo, V. Arnez-Paniagua, G. Ding, Y. Amirat, and S. Mohammed, "Adaptive proxy-based controller of an active ankle foot orthosis to assist lower limb movements of paretic patients," *Robotica*, vol. 37, no. 12, pp. 2147–2164, 2019.

[15] "Foot drop (ankle foot orthosis)," OrthodMed Canada Ltd, 2021. [Online]. Available: https://www.orthomed.ca/foot-ankle/foot/foot-drop

[16] "Afos - ankle foot orthoses," Custom Orthotic Design, 2021. [Online]. Available: https://www.customorthotic.ca/treatments/ankle-foot-orthoses/

[17] "Thermoplastic ankle joints," Becker Orthopedic, 2020. [Online]. Available: https://www.beckerorthopedic.com/Product/AnkleComponents/ThermoplasticAnkleJoints

[18] C.-H. Yeh, Y.-C. Tsai, F.-C. Su, L.-C. Kuo, K. Chang, and P.-H. Chuang, "Mechanical problem in 3d printed ankle-foot orthoses with function of energy storage," in *AIP Conference Proceedings*, vol. 2046, no. 1. AIP Publishing LLC, 2018, p. 020019.

[19] J. A. Blaya, "Force-controllable ankle foot orthosis (afo) to assist drop foot gait," Ph.D. dissertation, Massachusetts Institute of Technology, 2002.

[20] O. Ulkir, G. Akgun, and E. Kaplanoglu, "Mechanical design and analysis of a pneumatic ankle foot orthosis," in *2018 Electric Electronics, Computer Science, Biomedical Engineerings' Meeting (EBBT)*. IEEE, 2018, pp. 1–4.

[21] D. Adiputra, A. Rahman, M. Azizi, S. A. Mazlan, N. Nazmi, M. K. Shabdin, J. Kobayashi, M. Ariff, M. Hatta *et al.*, "Control reference parameter for stance assistance using a passive controlled ankle foot orthosis—a preliminary study," *Applied Sciences*, vol. 9, no. 20, p. 4416, 2019.

[22] S. Telfer, J. Pallari, J. Munguia, K. Dalgarno, M. McGeough, and J. Woodburn, "Embracing additive manufacture: implications for foot and ankle orthosis design," *BMC musculoskeletal disorders*, vol. 13, no. 1, p. 84, 2012.

[23] D. P. Ferris, J. M. Czerniecki, and B. Hannaford, "An ankle-foot orthosis powered by artificial pneumatic muscles," *Journal of applied biomechanics*, vol. 21, no. 2, pp. 189–197, 2005.

[24] D. P. Ferris, K. E. Gordon, G. S. Sawicki, and A. Peethambaran, "An improved powered ankle–foot orthosis using proportional myoelectric control," *Gait & posture*, vol. 23, no. 4, pp. 425–428, 2006.

[25] Y. H. Cha, K. H. Lee, H. J. Ryu, I. W. Joo, A. Seo, D.-H. Kim, and S. J. Kim, "Ankle-foot orthosis made by 3d printing technique and automated design

software," *Applied bionics and biomechanics*, vol. 2017, 2017.

[26] J. Leclair, S. Pardoel, A. Helal, and M. Doumit, "Development of an unpowered ankle exoskeleton for walking assist," *Disability and Rehabilitation: Assistive Technology*, 2018.

[27] L. Deberg, M. Taheri Andani, M. Hosseinipour, and M. Elahinia, "An sma passive ankle foot orthosis: Design, modeling, and experimental evaluation," *Smart Materials Research*, vol. 2014, 2014.

[28] J. Carberry, G. Hinchly, J. Buckerfield, E. Tayler, T. Burton, S. Madgwick, and R. Vaidyanathan, "Parametric design of an active ankle foot orthosis with passive compliance," in *2011 24th International Symposium on Computer-Based Medical Systems (CBMS)*. IEEE, 2011, pp. 1–6.

[29] A. Dubin, "Gait: the role of the ankle and foot in walking," *Medical Clinics*, vol. 98, no. 2, pp. 205–211, 2014.

[30] K. E. Gordon, G. S. Sawicki, and D. P. Ferris, "Mechanical performance of artificial pneumatic muscles to power an ankle–foot orthosis," *Journal of biomechanics*, vol. 39, no. 10, pp. 1832–1841, 2006.

[31] S. Hwang, J. Kim, J. Yi, K. Tae, K. Ryu, and Y. Kim, "Development of an active ankle foot orthosis for the prevention of foot drop and toe drag," in *2006 International Conference on Biomedical and Pharmaceutical Engineering*. IEEE, 2006, pp. 418–423.

[32] M. Moltedo, T. Bacek, K. Junius, B. Vanderborght, and D. Lefeber, "Mechanical design of a lightweight compliant and adaptable active ankle foot orthosis," in *2016 6th IEEE International Conference on Biomedical Robotics and Biomechatronics (BioRob)*. IEEE, 2016, pp. 1224–1229.

[33] Y. Zhang, R. J. Kleinmann, K. J. Nolan, and D. Zanotto, "Design and evaluation of an active/semiactive ankle-foot orthosis for gait training," in *2018 7th IEEE*

International Conference on Biomedical Robotics and Biomechatronics (Biorob). IEEE, 2018, pp. 544–549.

[34] J. Ward, T. Sugar, J. Standeven, and J. R. Engsberg, "Stroke survivor gait adaptation and performance after training on a powered ankle foot orthosis," in *2010 IEEE international conference on robotics and automation*. IEEE, 2010, pp. 211–216.

[35] S. M. Cain, K. E. Gordon, and D. P. Ferris, "Locomotor adaptation to a powered ankle-foot orthosis depends on control method," *Journal of neuroengineering and rehabilitation*, vol. 4, no. 1, p. 48, 2007.

[36] K. W. Hollander, R. Ilg, T. G. Sugar, and D. Herring, "An efficient robotic tendon for gait assistance.(technical briefs)(author abstract)," *Journal of Biomechanical Engineering*, vol. 128, no. 5, pp. 788–791, 2006.

[37] G. A. Pratt and M. M. Williamson, "Series elastic actuators," in *Proceedings 1995 IEEE/RSJ International Conference on Intelligent Robots and Systems. Human Robot Interaction and Cooperative Robots*, vol. 1. IEEE, 1995, pp. 399–406.

[38] B. Jardim and A. A. Siqueira, "Development and analysis of series elastic actuators for impedance control of an active ankle–foot orthosis," *Journal of the Brazilian Society of Mechanical Sciences and Engineering*, vol. 36, no. 3, pp. 501–510, 2014.

[39] A. W. Boehler, K. W. Hollander, T. G. Sugar, and D. Shin, "Design, implementation and test results of a robust control method for a powered ankle foot orthosis (afo)," in *2008 IEEE International Conference on Robotics and Automation*. IEEE, 2008, pp. 2025–2030.

[40] O. Kirtas, Y. Savas, M. Bayraker, F. Baskaya, H. Basturk, and E. Samur, "Design, implementation, and evaluation of a backstepping control algorithm for an active ankle–foot orthosis," *Control Engineering Practice*, vol. 106, p. 104667, 2021.

[41] R. Van Ham, B. Vanderborght, M. Van Damme, B. Verrelst, and D. Lefeber, "Maccepa: the mechanically adjustable compliance and controllable equilibrium position actuator for'controlled passive walking'," in *Proceedings 2006 IEEE International Conference on Robotics and Automation, 2006. ICRA 2006.* IEEE, 2006, pp. 2195–2200.

[42] A. M. Soliman, I. Hussain, M. I. Awad, and D. Gan, "Design and modeling of a variable stiffness barrel mechanism for ankle exoskeleton," in *ASME 2020 International Design Engineering Technical Conferences and Computers and Information in Engineering Conference*. American Society of Mechanical Engineers Digital Collection, 2020.

[43] D. Dong, W. Ge, B. Convens, Y. Sun, T. Verstraten, and B. Vanderborght, "Design, optimization and energetic evaluation of an efficient fully powered ankle-foot prosthesis with a series elastic actuator," *IEEE Access*, vol. 8, pp. 61 491–61 503, 2020.

[44] Y. Ning, H. Huang, W. Xu, W. Zhang, and B. Li, "Design and implementation of a novel variable stiffness actuator with cam-based relocation mechanism," *Journal of Mechanisms and Robotics*, vol. 13, no. 2, p. 021009, 2021.

[45] Y. Shao, W. Zhang, Y. Su, and X. Ding, "Design and optimisation of load-adaptive actuator with variable stiffness for compact ankle exoskeleton," *Mechanism and Machine Theory*, vol. 161, p. 104323, 2021.

[46] A. Basu, "Design of a novel active ankle foot orthosis using permanent magnets for drop foot assistance," Ph.D. dissertation, State University of New York at Buffalo, 2021.

[47] H. S. Choi, C. H. Lee, and Y. S. Baek, "Design and validation of a two-degree-of-freedom powered ankle-foot orthosis with two pneumatic artificial muscles," *Mechatronics*, vol. 72, p. 102469, 2020.

[48] D. P. Ferris and C. L. Lewis, "Robotic lower limb exoskeletons using proportional myoelectric control," in *2009 Annual international conference of the Ieee*

engineering in medicine and biology society. IEEE, 2009, pp. 2119–2124.

[49] M. Debeurre, C. M. Thalman, T. Hertzell, and H. Lee, "Soft robotic afo for active stroke rehabilitation," 2020.

[50] Y.-L. Park, B.-r. Chen, N. O. Pérez-Arancibia, D. Young, L. Stirling, R. J. Wood, E. C. Goldfield, and R. Nagpal, "Design and control of a bio-inspired soft wearable robotic device for ankle–foot rehabilitation," *Bioinspiration & biomimetics*, vol. 9, no. 1, p. 016007, 2014.

[51] W. Svensson and U. Holmberg, "Ankle-foot-orthosis control in inclinations and stairs," in *2008 IEEE Conference on Robotics, Automation and Mechatronics*. IEEE, 2008, pp. 301–306.

[52] I. Veneva, "Adaptive system for control of active ankle-foot orthosis and gait analysis," *International Program Committee*, p. 222, 2010.

[53] D. H. Kuettel III, "Pulley optimization for a walking-engine-actuated active ankle-foot orthosis," *Journal of Young Investigators*, vol. 31, no. 5, 2016.

[54] E. M. McCain, T. J. Dick, T. N. Giest, R. W. Nuckols, M. D. Lewek, K. R. Saul, and G. S. Sawicki, "Mechanics and energetics of post-stroke walking aided by a powered ankle exoskeleton with speed-adaptive myoelectric control," *Journal of neuroengineering and rehabilitation*, vol. 16, no. 1, pp. 1–12, 2019.

[55] J. R. Koller, D. A. Jacobs, D. P. Ferris, and C. D. Remy, "Learning to walk with an adaptive gain proportional myoelectric controller for a robotic ankle exoskeleton," *Journal of neuroengineering and rehabilitation*, vol. 12, no. 1, pp. 1–14, 2015.

[56] K. A. Shorter, Y. Li, E. A. Morris, G. F. Kogler, and E. T. Hsiao-Wecksler, "Experimental evaluation of a portable powered ankle-foot orthosis," in *2011 Annual International Conference of the IEEE Engineering in Medicine and Biology Society.* IEEE, 2011, pp. 624–627.

[57] I. Veneva and N. Ferreira, "Adaptive system for control of active ankle-foot orthosis and gait analysis," in *Mathematical Methods in Engineering*. Springer, 2014, pp. 153–163.

[58] I. Veneva, "Intelligent device for control of active ankle-foot orthosis," in *7th IASTED international conference on biomedical engineering; 17–19 feburary*. Acta Press, 2010, pp. 100–105.

[59] J. A. Blaya and H. Herr, "Adaptive control of a variable-impedance ankle-foot orthosis to assist drop-foot gait," *IEEE Transactions on neural systems and rehabilitation engineering*, vol. 12, no. 1, pp. 24–31, 2004.

[60] Y. Bai, X. Gao, J. Zhao, F. Jin, F. Dai, and Y. Lv, "A portable ankle-foot rehabilitation orthosis powered by electric motor," *The Open Mechanical Engineering Journal*, vol. 9, no. 1, 2015.

[61] J. Han, "From pid to active disturbance rejection control," *IEEE transactions on Industrial Electronics*, vol. 56, no. 3, pp. 900–906, 2009.

[62] J. Guerrero-Castellanos, H. Rifaï, V. Arnez-Paniagua, J. Linares-Flores, L. Saynes-Torres, and S. Mohammed, "Robust active disturbance rejection control via control lyapunov functions: Application to actuated-ankle–foot-orthosis," *Control Engineering Practice*, vol. 80, pp. 49–60, 2018.

[63] Y. Long, Z. Du, L. Cong, W. Wang, Z. Zhang, and W. Dong, "Active disturbance rejection control based human gait tracking for lower extremity rehabilitation exoskeleton," *ISA transactions*, vol. 67, pp. 389–397, 2017.

[64] J. Zhao, T. Yang, X. Sun, J. Dong, Z. Wang, and C. Yang, "Sliding mode control combined with extended state observer for an ankle exoskeleton driven by electrical motor," *Mechatronics*, vol. 76, p. 102554, 2021.

[65] M. Moltedo, G. Cavallo, T. Baček, J. Lataire, B. Vanderborght, D. Lefeber, and C. Rodriguez-Guerrero, "Variable stiffness ankle actuator for use in robotic-

assisted walking: Control strategy and experimental characterization," *Mechanism and Machine Theory*, vol. 134, pp. 604–624, 2019.

[66] S. K. Au, P. Dilworth, and H. Herr, "An ankle-foot emulation system for the study of human walking biomechanics," in *Proceedings 2006 IEEE International Conference on Robotics and Automation, 2006. ICRA 2006.* IEEE, 2006, pp. 2939–2945.

[67] V. Arnez-Paniagua, H. Rifaï, Y. Amirat, S. Mohammed, M. Ghedira, and J.-M. Gracies, "Modified adaptive control of an actuated ankle foot orthosis to assist paretic patients," in *2018 IEEE/RSJ International Conference on Intelligent Robots and Systems (IROS).* IEEE, 2018, pp. 2311–2317.

[68] A. Bagheri, D. Dorostkar, M. R. Zakerzadeh, M. J. Sadigh, and M. Mahjoob, "Assessment of the adaptive sliding mode control of an active ankle foot orthosis with an impedance reference," in *2019 7th International Conference on Robotics and Mechatronics (ICRoM).* IEEE, 2019, pp. 503–507.

[69] N. Jarrassé, T. Charalambous, and E. Burdet, "A framework to describe, analyze and generate interactive motor behaviors," *PloS one*, vol. 7, no. 11, p. e49945, 2012.

[70] J. Liu, N. A. A. Osman, M. A. Kouzbary *et al.*, "Optimization and comparison of typical elastic actuators in powered ankle-foot prosthesis," *International Journal of Control, Automation and Systems*, vol. 20, no. 1, pp. 232–242, 2022.

[71] M. Grimmer, M. Eslamy, S. Gliech, and A. Seyfarth, "A comparison of parallel- and series elastic elements in an actuator for mimicking human ankle joint in walking and running," in *2012 IEEE International Conference on Robotics and Automation.* IEEE, 2012, pp. 2463–2470.

[72] B. Convens, D. Dong, R. Furnémont, T. Verstraten, P. Cherelle, D. Lefeber, and B. Vanderborght, "Modeling, design and test-bench validation of a semi-active propulsive ankle prosthesis with a clutched series elastic actuator," *IEEE Robotics and Automation Letters*, vol. 4, no. 2, pp. 1823–1830, 2019.

[73] S. Sahoo, D. K. Pratihar, and S. Mukhopadhyay, "A novel energy efficient powered ankle prosthesis using four-bar controlled compliant actuator," *Proceedings of the Institution of Mechanical Engineers, Part C: Journal of Mechanical Engineering Science*, vol. 232, no. 24, pp. 4664–4675, 2018.

[74] F. Ning, Y. Chang, and J. Wang, "Variable stiffness structures utilizing pneumatic artificial muscles," in *MATEC Web of Conferences*, vol. 256. EDP Sciences, 2019, p. 01005.

[75] M. Shields, S. C. Gorber, I. Janssen, and M. S. Tremblay, "Bias in self-reported estimates of obesity in canadian health surveys: an update on correction equations for adults," *Health Reports*, vol. 22, no. 3, p. 35, 2011.

[76] K. Deb, A. Pratap, S. Agarwal, and T. Meyarivan, "A fast and elitist multiobjective genetic algorithm: Nsga-ii," *IEEE transactions on evolutionary computation*, vol. 6, no. 2, pp. 182–197, 2002.

[77] S. E. Talole, J. P. Kolhe, and S. B. Phadke, "Extended-state-observer-based control of flexible-joint system with experimental validation," *IEEE Transactions on Industrial Electronics*, vol. 57, no. 4, pp. 1411–1419, 2009.

[78] B. DeBoon, S. Nokleby, and C. Rossa, "Multi-objective gain optimizer for a multi-input active disturbance rejection controller: Application to series elastic actuators," *Control Engineering Practice*, vol. 109, p. 104733, 2021.

[79] Y. Nakagaki and G. Zhai, "A study on optimization algorithms in MPC," in *Journal of Physics: Conference Series*, vol. 1490, no. 1. IOP Publishing, 2020, p. 012073.

[80] M. Diehl, R. Findeisen, F. Allgöwer *et al.*, "Nominal stability of real-time iteration scheme for nonlinear model predictive control," *IEE Proceedings-Control Theory and Applications*, vol. 152, no. 3, pp. 296–308, 2005.

[81] A. Steinboeck, M. Guay, and A. Kugi, "A design technique for fast sampled-data nonlinear model predictive control with convergence and stability results,"

International Journal of Control, vol. 93, no. 1, pp. 81–97, 2020.

[82] L. Wang, E. H. van Asseldonk, and H. van der Kooij, "Model predictive control-based gait pattern generation for wearable exoskeletons," in *IEEE International conference on rehabilitation robotics*, 2011, pp. 1–6.

[83] S. Zarandi, S. Sani, M. Tootoonchi *et al.*, "Design and implementation of a real-time nonlinear model predictive controller for a lower limb exoskeleton with input saturation," *Iranian Journal of Science and Technology, Transactions of Electrical Engineering*, vol. 45, no. 1, pp. 309–320, 2021.

[84] M. Benoussaad, K. Mombaur, and C. Azevedo-Coste, "Nonlinear model predictive control of joint ankle by electrical stimulation for drop foot correction," in *IEEE/RSJ International Conference on Intelligent Robots and Systems*, 2013, pp. 983–989.

[85] O. Ulkir, G. Akgun, A. Nasab *et al.*, "Data-driven predictive control of a pneumatic ankle foot orthosis," *Advances in Electrical and Computer Engineering*, vol. 21, no. 1, pp. 65–74, 2021.

[86] H. Kervadec, J. Dolz, J. Yuan *et al.*, "Log-barrier constrained cnns," *Computing Research Repository (CoRR)*, 2019.

[87] S.-Y. Kuo, C.-H. Wu, C.-C. Chen *et al.*, "A novel metaheuristic: Fast jaguar algorithm," in *IEEE International Conference on Systems, Man, and Cybernetics (SMC)*, 2021, pp. 146–151.